Steady and oscillatory flow in the entrance region of microchannels

Author:
Sinclair, Alexander

Publication Date:
2012

DOI:
https://doi.org/10.26190/unsworks/15372

Steady and Oscillatory Flow in the Entrance Region of Microchannels

Alexander Sinclair

School of Mechanical and Manufacturing Engineering

University of New South Wales

A thesis submitted for the degree of

Doctor of Philosophy

2012

ORIGINALITY STATEMENT

'I hereby declare that this submission is my own work and to the best of my knowledge it contains no materials previously published or written by another person, or substantial proportions of material which have been accepted for the award of any other degree or diploma at UNSW or any other educational institution, except where due acknowledgment is made in the thesis. Any contribution made to the research by others, with whom I have worked at UNSW or elsewhere, is explicitly acknowledged in the thesis. I also declare that the intellectual content of this thesis is the product of my own work, except to the extent that assistance from others in the project's design and conception or in style, presentation and linguistic expression is acknowledged.'

Signed: ..... Date: April 16, 2012

To my loving parents, Sue and Derek (Deeman)...

Acknowledgements

Firstly, I would like to gratefully acknowledge the guidance and support of my supervisors, Gary Rosengarten, Victoria Timchenko and John Reizes. You have provided me with an open ear, exposed me to new ideas and taught me to work independently.

I would like to thank my friends and family for their support. I am overwhelmingly appreciative of the continued encouragement you all have provided me throughout the PhD. I would particularly like to thank Cam Stanley, my brother in arms, for all his help over the last few years. You have been a rock for me during this testing journey and I know it would not have been possible to make it through to the other side without you. Thank you for companionship and the many memorable moments along way!

Finally I would like to thank my parents, Sue and Derek, for their unconditional love and support.

Abstract

The entrance region of a fluid channel is where the velocity distribution changes substantially from its initial condition at the entrance to that of fully developed flow. This region is particularly influential in microchannels as it may be a substantial portion of the total channel length, meaning that pressure drop and heat transfer are significantly different than for fully developed flow. Despite the fact that much work has been done on the development of steady flow, no reliable correlations exist for low Reynolds (Re) number flows in rectangular channels, and there is even less data available for oscillatory flows. It follows that a greater understanding of flow development would aid in the design of devices using microchannels in particular, since they involve low Reynolds numbers and are often oscillatory.

In this study a microfluidic device was developed to generate controllable oscillatory flow together with a modular interface system to allow a reliable connection to a syringe pump so as to generate steady and pulsatile flows. The flow of de-ionised water from a large planar plenum into a square channel, nominally 50 by 50 micrometres, was studied under steady, oscillatory and pulsatile flow conditions. Time and phase averaged velocity fields were measured using micro-Particle Image Velocimetry.

Steady flow was studied in the entrance region of the microchannel for Reynolds numbers, $1 \leq Re \leq 66$. Entrance lengths were calculated from the measured centerline velocities. The expected non-linear relationship between entrance length with Re, for low Reynolds numbers was found, and the flow was shown to develop much faster than predicted by conventional correlations due to the planar entry. An entrance length correlation is proposed for steady flow under these conditions.

Oscillatory flow (zero net flow) was examined with Stokes number, α, < 2.45. Time varying entrance lengths were calculated and these varied significantly over an oscillation cycle. Pulsatile flow (a mean flow superimposed on the oscillatory flow) for $\alpha = 2.45$ was examined for a range of oscillatory to steady flow ratios, $0.93 < A < 3.70$. The entrance length was found to vary in time about the steady flow value. For both oscillatory and pulsatile conditions, the maximum entrance length was accurately described by the proposed steady flow correlation for entrance length, based on Re at peak flow. These results represent the first systematic experimental study into oscillatory entrance flows.

Contents

List of Figures

List of Tables

Nomenclature

Roman Symbols

A	ratio of oscillatory to steady flow components
a	half channel width, (μm)
B	contraction ratio
b	half channel height, (μm)
C^+	high Reynolds number asymptote
d_p	tracer particle diameter, (μm)
d_e	particle image diameter, (μm)
D_c	larger diameter in a sudden contraction, (μm)
D_h	hydraulic diameter, (μm)
f	frequency of oscillation, (Hz)
L_e	entrance length, (μm)
M	magnification
Kn	Knudsen number
Re	Reynolds number based on the instantaneous average velocity, $\bar{u}$
Re_{os}	Reynolds number based on the oscillating average velocity, $\bar{u}_{os}$
Re_{puls}	Reynolds number based on the peak average velocity, $\bar{u}_{puls}$

St	Strouhal number
u	streamwise velocity, (m/s)
$\bar{u}_{os}$	oscillatory mean velocity amplitude, (m/s)
$\bar{u}_s$	steady cross-sectional average velocity, (m/s)
$u_{cl,fd}$	fully developed centreline velocity, (m/s)
$\bar{u}_{puls}$	sum of oscillatory and steady velocity amplitudes, (m/s)
U_∞	freestream velocity, (m/s)
$\bar{u}$	instantaneous mean velocity, (m/s)
U_o	velocity amplitude of an oscillating plate, (m/s)
V_{os}	amplitude of voltage signal, (V)

Greek Symbols

α	Stokes number, $a\sqrt{\omega/\nu}$
β	phase angle delay, (deg)
Δt	laser pulse separation time, (μs)
Δx	tracer particle displacement, $(pixels)$
δ	boundary layer thickness, (μm)
δ_{corr}	half depth of correlation, (μm)
δ_{os}	oscillating boundary layer thickness, $\sim \sqrt{\nu/\omega}$, (m)
η	non-dimensional distance from an oscillating plate
ϕ	phase angle delay, (deg)
γ	aspect ratio of a rectangular duct
κ	Boltzmann constant, (J/K)

λ	molecular mean free path, (μm)
μ	dynamic viscosity, $(kg/m \cdot s)$
ν	kinematic viscosity, (m^2/s)
ω	angular velocity, (rad/s)
ρ	density, (kg/m^3)
θ	phase angle of the mean oscillatory flow, (deg)

Acronyms

ASE	Advanced Silicon Etching
CCD	Charge Coupled Device
CFD	Computational Fluid Dynamics
$DRIE$	Deep Reactive Ion Etching
HF	HydroFluoric acid
ICP	Inductively Coupled Plasma
ID	Inner Diameter
$MEMS$	Micro Electro Mechanical Systems
NA	Numerical Aperture
OD	Outer Diameter
$PDMS$	PolyDiMethlySiloxane
PIV	Particle Image Velocimetry
PTU	Programmable Timing Unit
$SIMPLE$	Semi Implicit Method for Pressure-Linked Equations
UVP	Ultrasonic Velocity Profile

Chapter 1

Introduction

1.1 Background

The flow of fluid in the entrance region of a pipe is one of the most widely studied problems of hydrodynamics (Wagner (1975)) and is simply known as the *entry flow problem*. Research on this problem began in the 1800's with the work of Hagenback, Boussinesq and Couette (Boger (1982)), who were interested in the pressure drop incurred in this region, in order to develop capillary rheometers that could make accurate measurements of a fluid's viscosity. The rigorous analysis of viscous flow about a solid body was first made possible with the aid of ideas suggested by Ludwig Prandtl in 1904 (Schlichting & Gersten (2000)). Prandtl proposed that the flow be divided into two regions; a thin layer in the neighbourhood of the solid body known as the boundary layer in which viscous effects dominate; and a region outside this layer in which the fluid can be assumed to be inviscid.

How Prandtl's model has been applied to laminar flow in the entry region of a channel is shown in Figure 1.1. Fluid at the channel wall does not slide over it but adheres to it, so that the velocity at the wall along the entire channel length is zero. This condition, known as the 'no slip condition', causes the fluid layers in the immediate vicinity of the wall to be retarded by viscous action thereby forming a thin boundary layer (Tietjens *et al.* (1934)), described by the thickness, δ. As the flow progresses downstream the effect of the solid surface is felt further out into the flow and the boundary layer thickness is said to grow

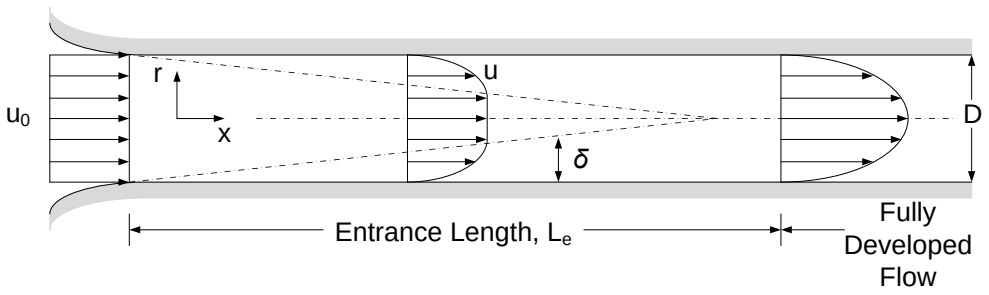

Figure 1.1: Flow in the entrance of a channel of characteristic dimension D.

(White (1999)). Since the mass flow rate remains the same at each cross section of the channel, the fluid which had been slowed near the boundaries forces the fluid in the central region of the channel to be accelerated. Far downstream from the entrance, the boundary layers merge and the entire channel cross-section is dominated by viscous effects. Farther downstream the velocity profile no longer changes and the flow is said to be fully developed.

The distance from the entrance of the channel to the position at which the flow becomes fully developed is called the hydrodynamic entrance length, L_e, which defines the entrance region of a channel. Prediction of the entrance length has been the primary concern of the entry flow problem (Boger (1982)), and through the years considerable effort has been applied in analytically determining its value. However, owing to the nonlinearity of the inertia terms in the equations of motion, the entry flow problem even for laminar flow does not yield to an exact solution (Sparrow *et al.* (1964)).

The widespread availability of computers in the last few decades has allowed the development and implementation of advanced numerical techniques, capable of solving the full equations of motion by finite difference or finite element methods (Wagner (1975)). Developing flow in the entrance region became a useful benchmark for the evaluation and comparison of these numerical procedures (Atkinson *et al.* (1969)), and as a result it became possible to obtain solutions for laminar flows with any boundary conditions. The conditions which received the most attention were flow between parallel plates and flow in circular pipes as they are the geometries that are the most amendable to mathematical treatment (Shah & London (1978)) and because the circular pipe is the most commonly

used macroscale geometry in practice.

The entrance region is significant in many engineering applications. Therefore a knowledge of the entrance length allows accurate estimates of the pressure drop and heat transfer rates to be made in any flow-intake device (Han (1960)).

For flow in circular pipes and between parallel plates, the entry flow problem is considered by some authorities to have been solved (Boger (1987)). However, the emergence of a new field of research, known as 'microfluidics' has renewed interest in the entry flow problem due to the unique flow conditions found in its devices.

1.2 Microfluidics

Over the past two decades a promising new area of research and application, known as the microfluidics field has emerged. Microfluidics can be defined as

> '...the science and technology of systems that process or manipulate small (10^{-9} to 10^{-18} litres) amounts of fluids, using channels with dimensions of tens to hundreds of micrometers.' -Whitesides (2006)

This field was born on the back of technology developed by the microchip industry, which has been used to create devices with microscopic features that are capable of handling fluids. The applications of such devices extends over a number of traditional research fields such as chemistry, biology, and medicine, and of course encompasses the various engineering disciplines. One of the main goals of microfluidic systems has been to create a so called 'lab-on-a-chip', in which a number of traditional biological and chemical processes are incorporated onto a single microchip (Beebe *et al.* (2002)). The size and volume of fluidic systems allows greatly reduced chemical and reagent consumption, shortened processing times, higher resolution and sensitivity of measurement, and enhanced safety of measurement, easy portability and ease of installation because of its small size (Hessel *et al.* (2005)).

The reduction in length scale of fluidic systems also brings about a change in the fundamental physics of the flow (Squires & Quake (2005)). Whereas inertial effects dominate and are responsible for responsible for the phenomenon of turbulence that occurs in most engineering applications, viscous effects control

microscale flows. The flow becomes highly ordered and free of the random fluctuations of turbulence. This regime is known as laminar flow, and in microchannel flows occurs almost exclusively.

Another flow type which is widespread in microfluidic devices are oscillatory flows (Tikekar *et al.* (2010)), that is, flows which contain a harmonic component. Due to the absence of turbulence in microchannels, fluidic oscillations have been exploited in order to disturb the flow in a number of types of applications. For example to enhance the mixing of two streams, (Glasgow & Aubry (2003), Bottausci *et al.* (2004)), for heat transfer augmentation (Timchenko *et al.* (2007)) and also for particle separation (Nilsson *et al.* (2004)).

A secondary reason for the prevalence of oscillatory flows is due to the pumping mechanisms that are used in microdevices. The vast majority of pumps at this scale are mechanical displacement pumps (Laser & Santiago (2004)), which function in a positive reciprocating manner, such as diaphragm and peristaltic pumps, which cause the resulting flow to have oscillatory components. The diaphragm pump is the most common micropump design in the literature (Iverson & Garimella (2008)), largely due to its ease of fabrication at this scale compared with other types of pumps.

The fabrication of microfluidic devices can be achieved using a large number of technological processes, the bulk of which have been derived from micromachining techniques developed in the microelectronics and Micro-Electro-Mechanical Systems (MEMS) fields. These techniques use crystalline silicon as the substrate material and consequently a number of these processes create features that follow the crystallographic planes of the silicon material. Channels fabricated in this manner have prismatic shapes with rectangular, triangular or trapezoidal cross-sections. A number of the existing fabrication techniques also largely produce planar structures (Stone *et al.* (2004)).

The prismatic structures and characteristics of flows in microfluidic devices just described are substantially different from those that have been conventionally analysed. For this reason there has been a resurgence of interest in a number of fundamental fluid mechanics problems for flow under these unique conditions.

1.3 Motivation

While a significant amount of research has been devoted to flow in the fully developed region of microchannels, little work has been done on entry flows (Bayraktar & Pidugu (2006)). The entrance region of a channel is of large practical importance because the wall shear, pressure drop and heat transfer rates are significantly different than for fully developed flow. This region is also particularly important in microchannels because their lengths are frequently very short, especially when compared to conventional channels, and the entrance length is often a significant potion of the entire length of the channel (Ahmad & Hassan (2010)).

A number of early studies of flow in microchannels reported a size effect (for example Peng & Peterson (1996)) and the validity of conventionally determined parameters for microchannel flows was questioned. Interestingly, one of the main reasons for the discrepancies between reported experimental results and classical theory was not adequately accounting for entrance effects (Steinke & Kandlikar (2006)). Unfortunately, because of the conditions that occur in a large number of microfluidic devices there are no universal correlations to determine the entrance length.

In steady flow in microfluidic devices, as pointed out by (Lee *et al.* (2008)), two geometric factors limit the applicability of conventional entrance length correlations. First, as described previously, the channel cross-sections are usually not circular, and most of the entrance length research has been devoted to either flow in circular pipes or between parallel plates. Secondly, the planar structures which are commonly fabricated, result in the channel and region upstream of the channel having surfaces in common. This allows a significant amount of predevelopment of the flow to occur before the channel inlet, which is not accounted for in almost all existing correlations.

Oscillatory flows, which play a role in a large number of microfluidic devices have received little attention in regards to their development in the entrance region. Flows with an oscillating component also occur in a number of other situations, such as in arterial flows, in the exhaust of reciprocating engines, out of synthetic jet devices, and in fluid transmission lines. Therefore the study of the development of oscillatory flow is important in its own right.

In this thesis, flow in the entrance region of a microchannel is examined

for steady, oscillatory and a combination of the two, namely, pulsatile flow, conditions. The entrance region consists of a large planar entry into a square microchannel, which has been fabricated with traditional micromachining techniques. These flow conditions are those which are prevalent throughout existing microfluidic devices in the literature, and apply to devices designed for many different applications. The design and optimisation of future microfluidic devices, that will be significantly improved because of the detailed analysis of flow in the entrance region presented in this thesis.

Chapter 2

Literature Review

This thesis builds upon the work of scores of researchers who have examined entry flows over the past 150 years. It is inspired by the unique flow conditions found within microdevices that present a new perspective from which to explore the entry flow problem.

In this chapter an overview of the relevant research found in the open literature is presented. It begins in Section 2.1 with a discussion of the prevalent flow conditions that occur in microfluidic devices. Following that, an account is given of the techniques used in their fabrication and of the methods used to connect them to macro-sized components. In Section 2.2, the large body of research for the steady flow in the entrance of a region of a channel is reviewed. Section 2.3 extends the discussion on entrance region flow to oscillatory flow conditions. This is followed by a summary in Section 2.4 of the key issues found in the survey of the literature. Finally, the objectives for the current research project are outlined in Section 2.5.

2.1 Microfluidics and Microchannel flow

Microfluidic devices range in complexity and can contain a number of different fluidic components. These include pumps, valves, flow sensors, mixers and filters, all which have been adapted to work with microscale dimensions. However, the element integral to all microfluidic devices are the channels, which transport fluids throughout the device.

The use of small passages for the study of flow phenomena occurred well before the advent of microfluidics. In the classic experiments of Poiseuille, fine capillaries, $29 - 142\mu m$ in diameter, were used to determine the resistance to flow through tubes (Rouse & Ince (1963)). In recent times, similar experiments have been conducted but extended the lower limit in size down to the nanometre range such as in the experiments performed by Cheng & Giordano (2002).

Table 2.1: Channel classification scheme given by Kandlikar (2006).

Classifcation	**Size**
Conventional channels	$> 3mm$
Minichannels	$3mm \geq D > 200\mu m$
Microchannels	$200\mu m \geq D > 10\mu m$
Transitional Microchannels	$10\mu m \geq D > 1\mu m$
Transitional Nanochannels	$1\mu m \geq D > 0.1\mu m$
Nanochannels	$0.1\mu m \geq D$

In Table 2.1, a size based classification scheme for channels given in Kandlikar (2006) has been reprinted. Here D is the diameter for circular ducts or the smallest dimension of the channel for non-circular ducts. This table reflects the overall usage of nomenclature in the literature for different sized channels. In this work, the term 'microchannel' is applied in a more general way and used to describe channels with a smallest dimension less than $1mm$.

The decrease in size of a channel can have a profound effect of the flow phenomena that occurs in channel flows. Accompanying the decrease in dimensions is an increase in the surface area to volume ratio of the channels and flow within them. Phenomena in channels that involve surface effects are greatly be enhanced by this reduction in size and become increasingly important in microscale flows. Surface forces are caused by the accumulative effect of intermolecular forces, which are short range ($< 1nm$) but through a large number of molecules cause longer range effects ($> 0.1\mu m$) (Ho & Tai (1998)). For example, surface tension and electrokinetic forces become significant at these scales. These effects can be exploited in microscale applications such as droplet generation using flow focusing and capillary forces (Anna *et al.* (2003)) or DNA separation using capillary electrophoresis (Effenhauser *et al.* (1994)).

The range of flow phenomena at this scale is diverse and the list of potential applications for microfluidic devices are endless. In the current work, further discussion of microchannel flow will be restricted to the pressure driven flow of a single phase, Newtonian fluid under isothermal conditions.

2.1.1 Characteristics of Flow in Microdevices

The reduction in physical size also sees the breakdown of a number of assumptions, boundary conditions and correlations used in macroscopic modelling of fluid flows. The cornerstone of classical fluid modelling is the concept of a continuum Fox *et al.* (1985)). Under the continuum assumption the fluid is treated as a continuous medium with properties that vary continuously in space. Although these properties are molecular in origin, their overall effect is accounted for in macroscopic properties such as temperature, pressure, density and viscosity Massey & Ward-Smith (1998). For gases, this idealisation holds true when the average distance travelled by molecules in between collisions, the mean free path λ, is much smaller than the characteristic size of the flow. The ratio of the two lengths is the Knudsen number

$$Kn = \frac{\lambda}{D} \tag{2.1}$$

and the continuum approach is valid for $Kn < 0.001$ (Gad-el Hak (1999)). The distance between molecules in liquids is much smaller than for gases, and the continuum assumption is thought to apply for most liquid flows in microchannels. Nguyen & Wereley (2002) considered the deviation of point properties within a fluid, and argued that liquids should behave as a continuum provided the length scale of the flow is greater than about $10nm$, which is substantially smaller than the size of most microchannels.

The applicability of the no-slip condition at a solid boundary for liquid flow has also been the subject of a number of recent investigations and it has been conjectured in these studies that microscopic slip does exist for liquid flows (Lauga & Stone (2003)). In this case slip is a complicated issue that depends on many physical factors such as surface wettability, roughness, liquid shear rate and polarity (Cao *et al.* (2009)). For most practical applications slip lengths are small and the no-slip condition is an excellent approximation for flows with length scales above

ten nanometres (Stone *et al.* (2004)).

Under the considerations above, for flow in microchannels with dimensions of the order of $\sim 100\mu m$ the continuum assumption and no slip condition apply and the flow is governed by the Navier-Stokes equations. The properties of flow under such conditions are then well known through dimensional analysis and the flow in microchannels is dominated by viscous effects with little influence from inertia. The primary dimensionless parameter describing viscous flows is the Reynolds number (White (1991)),

$$Re = \frac{\overline{u}D}{\nu} \tag{2.2}$$

where $\bar{u}$ is the cross-sectional average velocity, D is the characteristic length and ν is the kinematic viscosity of the fluid. For flows in microchannels the Reynolds numbers are low, of the order of ~ 10, and the flow is dominated by viscous effects with a negligible influence from inertia. The flow is known as laminar flow, which is highly ordered and free from macroscopic fluctuations (Shah & London (1978)). This is quite different from flow in larger pipes where inertia effects are significant and the phenomena of turbulence is the normal occurrence. Turbulent flow, that is flow that has become highly disordered in both space and time (Kerswell (2005)), exists when disturbances to the flow are no longer damped out by viscous action but develop into irregular motions within the flow. There exists a so called critical Reynolds number, such that below that limit initial disturbances are damped out (Tietjens *et al.* (1934)). The generally accepted value of the Reynolds number for the onset of turbulence in pipe flow is $Re = 2300$ (White (1999)), however current estimates vary in the range $1760 < Re < 2300$ (Kerswell (2005)).

Interestingly early experiments with flow in microchannels found a deviation from conventional theory, and transition to turbulence was suggested to occur at much lower Reynolds numbers (see Wu & Little (1984), Peng *et al.* (1994), Mohiuddin Mala & Li (1999) and Qu *et al.* (2000)). Measured friction factors or Nusselt numbers were found to be either different from conventional theory or to deviate from a linear trend with Reynolds number at much lower values of Re than expected, as low as $Re = 70$ (Peng & Peterson (1996)).

However, a number of these discrepancies can be explained with conventional

concepts (Morini (2004)) rather than resorting to suggestions of 'new effects' and more recent experiments have tended to agree more and more with classical theory (Celata *et al.* (2009)). For example, the careful work by Judy *et al.* (2002) and Li (2003) using pressure drop measurements, Li & Olsen (2006) and Natrajan & Christensen (2007) using velocity measurements, and Sharp & Adrian (2004) using a combination of the two measurements, all agreed well with results determined by conventional means.

The reasons for the reported deviations include not accounting for minor losses and the entrance region effects (Steinke & Kandlikar (2006)), viscous heating effects (Morini (2005)), large relative roughness (Gamrat *et al.* (2008)) and measurement uncertainty specifically concerning channel dimensions (Judy *et al.* (2002)).

The discussion above highlights the difficulty with performing experiments on microscale devices. Design of such devices require that careful consideration be given to a number of factors, arguably the most important of which is the accurate determination of the structural features resultant from the fabrication processes.

2.1.2 Fabrication and Interfacing

Microfluidic devices can be manufactured using a large number of technological processes, the bulk of which have been derived from micromachining techniques developed by the microelectronics and MEMS fields. These techniques are classified by the way in which structures are formed or 'machined'. Two broad categories exist, those processes where structures are formed by the removal of material from the substrate (bulk micromachining) and those where the addition of a secondary material on the surface of the substrate is used to form the structures (surface micromachining). Both groups incorporate similar technologies such as the use of thin film spin coating or deposition, photolithographic patterning and selective etching. The technologies from the integrated circuit industry are largely specific to silicon as a substrate however interest in microfluidic devices has lead to new processes and materials being introduced in microtechnologies, particularly those involving polymers (Abgrall & Gue (2007)).

Silicon and glass are still often the most suitable materials for microfluidic

devices. They both have high values of Young modulus, can handle high temperatures and do not react strongly to solvents, which makes them well suited for a number of chemical applications. The methods available for micromachining silicon are numerous and detailed in a number of texts such as Madou (2002). The most important technique in micromachining is Reactive Ion Etching (RIE) (Nguyen & Wereley (2002)), which is a dry anisotropic etch process capable achieving highly vertical walls of independent of crystallographic orientation. Deep Reactive Ion Etching (DRIE) and Advanced Silicon Etching (ASE) can produced high aspect ratio structures and are well suited to many microfluidic designs.

A key material in the development of microfluidic systems has been the polymer - poly(dimethlysiloxane), PDMS (Whitesides (2006)). It's use has allowed a wider range of researchers to be part of the microfluidics field, without needing expensive, sophisticated technology(Abgrall & Gue (2007)). PDMS as a material for microfluidics devices has many benefits, it is inexpensive, optically transparent, chemical inert and is permeable to gases. Structures are formed by casting the PDMS in a mold or master fabricated by usual micromachining techniques, re-usable. The drawbacks of PDMS are few but include its low modulus of elasticity, which means it is easy deformable, and it swells with absorption of organic solvents.

The final procedure in fabrication is the sealing or bonding of the various layers that are used to form the enclosed microchannels. A number of different bonding options exist depending on the material. For example silicon can be bonded directly to another silicon layer using silicon fusing bonding, or to a glass layer using anodic bonding (Schmidt (1998)). PDMS can be bonded to another layer of PDMS or glass using exposure an oxygen plasma treatment or to the discharge of a corona (Haubert *et al.* (2006)). For other combinations of materials an intermediate layer such as an adhesive can be used to bind the two layers together (Niklaus *et al.* (2006)).

Regardless of the exact processes used to form microfluidics devices, the resultant microchannels generally share a number of common features between one another. Etching, molding and bonding processes typically produce planar geometries, which means different regions within a microfluidic device will have surfaces in common. For example plenums and microchannels will often share a

number of surfaces, as was pointed out in Lee *et al.* (2008). Another resultant feature specifically for straight surfaces and sharp angles edges, is that their resultant finish becomes rounded (Stone *et al.* (2004)), sharp edges become filleted and flat surfaces become curved. Similarly the resultant geometry of microchannels is often quite different from intended and can only be known after fabrication.

In order to function, MEMS and microfluidic devices interact with a number of peripheral systems through the transport of fluids, power and data. The components which facilitate this connection between the micro-components of a device and the macro-environment of the world (commonly something) have been given a few titles, such as the macro-to-micro interface, world-to-chip interface, or simply the interface, interconnect or packaging (Fredrickson & Fan (2004)). The interfacing of microdevices has been one of the major challenges preventing microengineering products from fulfilling their commercial potential (Yang & Maeda (2002)).

Packaging of microfluidic devices has been challenging issue essentially due to the small size of the interfaces involved, and the large number of constraints placed upon them. Therefore custom solutions are often required (Bhagat *et al.* (2007)) and because of this the interfacing of microdevices has become an avenue of research in its own right. Difficulties also occur because devices are often flat and featureless making connection of additional modules difficult and because chips are fabricated in thin, brittle materials such as silicon and glass making them fragile (Nittis *et al.* (2001)). Some of the conditions which generally need to be satisfied for successful interfacing of microfluidic devices as pointed out by Nittis *et al.* (2001), and Fredrickson & Fan (2004), such are:
Reliability - connections need to remain leak proof at high pressures often found in microfluidic devices, and remain for sufficient lengths of time.
Chemical Compatibility - All components exposed to the working fluid need to be compatible with a range of laboratory solvents and reagents that may be used during the experiment or in cleaning of the microdevice.
Low dead volumes - Additional volume to the chip arrangement can decrease the efficiency of the device by increasing sample wastage and causing increased pressure drop across the device.
Ability to observe on-chip processes - The interface solution must still allow the chip to function as intended, which means providing access for measurement

techniques and generally optical access to the device.
Additionally, as with all working products, the solution needs to be cost effective and relatively easy to use.

A large number of different interconnect methods have now been presented in literature that have attempted to satisfy these constraints (for a more thorough account see the review given by Fredrickson & Fan (2004)). The most common method used to connected fluidic lines to microdevices it to bond tubes or capillaries to an opening on the microfluidic chip using some sort of adhesive. The adhesive not only holds the tubing in place but provides a seal between the microdevice and tubing. There are a number of drawbacks of using an adhesive, such as: the risk of clogging channel during its application, the adhesive may interaction with various solutions leading to contamination problems, and the bond establishes a permanent connection, which cannot be removed if applied unsuccessfully or if the chip becomes damaged or clogged.

Due to these disadvantages a number of solutions that use a mechanical seals based upon a pressure fit have been devised. Yang & Maeda (2002) developed one of the first fluidic interconnection systems using flexible silicone tubing that acted as an O-ring seal on the side of the microchip. The chip and tubing were aligned and held in place by a frame or socket and no leaks were observed for a pressure of $0.2MPa$. Nittis *et al.* (2001) and Bhagat *et al.* (2007) employed modular designs, which incorporated O-rings/gaskets to provide re-useable seals for high pressure applications (up to $1.7MPa$ for the latter paper). Another interesting modular interface was designed by Shimura *et al.* (2007) in order to provide a fluidic interconnect that could be opened and closed flush to the chips surface. The design incorporated a Teflon rotor valve, which pressed flush to the chip surface and was capable of sealing up to at least $1.0MPa$ in pressure.

This section attempted to provide an overview of the design considerations required in the successful fabrication of a fully integrated microfluidic system. The structures formed by the selected fabrication processes as well as the designed interface system have a marked influence on the flow fields that occur within a microfluidic device.

2.2 Steady Flow in the Entrance Region of a Channel

The distance from the entrance of the channel to the position at which the flow becomes fully developed is called the hydrodynamic entrance length, L_e. The flow approaches this state asymptotically and is never achieved (Tietjens *et al.* (1934)). Therefore a more practical definition of the entrance length is the distance from the inlet to a location along the pipe at which the velocity distribution does not differ from its fully developed value within experimental measurement error. A variety of definitions have been used in literature but the most commonly applied definition is the distance from the entrance of the duct required for the cross-sectional maximum velocity to reach 99% of its fully developed value (Shah & London (1978)).

Like most concepts in fluid mechanics the determination of the entrance length and the understanding of the phenomena in the entrance region came largely from theoretical work, backed by a few key experimental results. One hundred and thirty references devoted to the study of entrance length were presented by Fan & Hwang (1966), one hundred and seven of which are purely theoretical. At about this time the increasingly widespread use of digital computers led to the entrance flow problem becoming a standard for comparison for numerical schemes for solving the complete Navier-Stokes equations (Morihara & Ta-Shun Cheng (1973), Wagner (1975)). The entry flow problem has now been examined using a large number of techniques, both numerical and experimental, with a large variety of different boundary conditions. These are discussed below in some detail with specific attention paid to the effects of low Reynolds number flows.

2.2.1 Flow with a Uniform Entrance Profile

The entrance condition most widely studied is a uniform velocity distribution at the duct inlet, which is often referred to as a smooth duct entry. Early studies employed this entry condition in combination with a number of boundary layer type idealizations to devise approximate analytical solutions to the entry flow problem. A vast number of approaches have been utilised, the details of which can be found in the reviews by Schmidt & Zeldin (1971), Fargie & Martin (1971),

and Shah & London (1978). The important property of these solutions is that, when expressed in terms of non-dimensional quantities, the entrance length is independent of the Reynolds number (Shah & London (1978)) and it can be expressed as:

$$C^+ = \frac{L_e}{DRe} \tag{2.3}$$

Boundary layer solutions, for example the solution of Schlichting & Gersten (2000) and Bodoia & Osterle (1961) for a flat plate and Langhaar (1942) and Hornbeck (1964) for a circular pipe, have been shown by subsequent numerical and experimental investigations to correctly predict the entrance lengths for large Reynolds number flows. Numerical solutions of the full Navier-Stokes equations by Morihara & Ta-Shun Cheng (1973) for the flow between parallel plates and Friedmann *et al.* (1968) for flow in a circular pipe agreed well with the boundary layer solutions for $Re > 200$. Experimental validation of the high Re asymptotes for flow in circular pipes was reported by Atkinson *et al.* (1967) and Berman & Santos (1969) for $Re > 300$. In the extreme case boundary layer results were also been shown to hold true for Reynolds numbers of the order of 40,000 in the experiments of Pfenninger (1961). Thus the constant C^+ in Equation 2.3 has come to be known as the high Reynolds number asymptote with Reynolds numbers greater than about 200 being regarded as 'high' Reynolds number in entry flows.

At the other extreme of the Reynolds number scale, that is as $Re \to 0$, viscous forces become dominant and the convective terms in the equations of motion become vanishingly small. Flow in this regime is known as creeping flow or Stokes flow. The omission of the convective terms from the equations of motion represents a significant reduction in their complexity. Analytical solutions to the entry problem for creeping flows have been derived independently by Friedmann *et al.* (1968) and Lew & Fung (1969) for the condition of uniform entry flow in a circular pipe and by Abarbanel *et al.* (1970) and Brandt & Gillis (1966) for parallel plates. Interestingly the entrance lengths do not approach zero as $Re \to 0$, but approach a finite value. The distance for creeping flow to develop from a uniform velocity at the inlet to its fully developed profile is about 0.6D

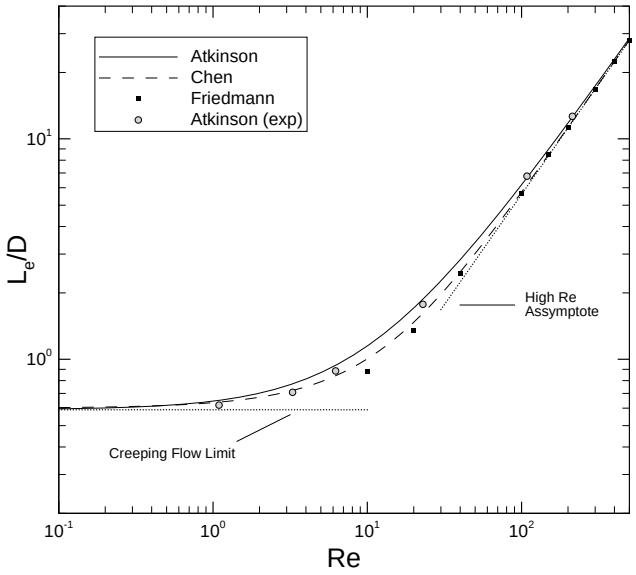

Figure 2.1: Entrance lengths for a circular pipe. Circles experiments of Atkinson *et al.* (1969), squares numerical solution of Friedmann *et al.* (1968), solid line Equation 2.4, dashed line Equation 2.6.

for either geometry.

For flow with Reynolds numbers between these limits, $0 < Re < 200$, referred to as just low Reynolds numbers flows, determination of entrance lengths can only be achieved by the solution of the complete set of Navier-Stokes equations or through careful experiments. In this region the entrance length varies from its linear relationship with Reynolds number at high Re, to a constant value as $Re \rightarrow 0$. This relationship between L_e/D, and Re, has been expressed in a number of different correlations determined from existing results in literature. The most commonly presented and used correlation is the linear form of Equation 2.3. It provides sufficient accuracy for the majority of engineering applications, which generally occur at higher Re. To extend a linear form of the correlation to also apply low Reynolds numbers, Atkinson *et al.* (1969) proposed the superposition of the high Reynolds number asymptote and the creeping flow limit. For a circular pipe this method gives the correlation:

$$L_e/D = 0.59 + 0.056Re \tag{2.4}$$

and for a flat plate:

$$L_e/D_h = 0.3125 + 0.011Re \tag{2.5}$$

Chen (1973) proposed two correlations of a different form, which provided a better fit to the data of Friedmann *et al.* (1968) for a circular pipe and agree well with the results of Morihara & Ta-Shun Cheng (1973) for flow in between parallel plates and are the correlations recommended by Shah & London (1978).

$$L_e/D = \frac{0.60}{1 + 0.035Re} + 0.056Re \tag{2.6}$$

and for a flat plate:

$$L_e/D_h = \frac{0.315}{1 + 0.0175Re} + 0.011Re \tag{2.7}$$

In Figure 2.1 the two correlations for a circular pipe, Equation 2.4 and Equation 2.6, have been plotted alongside the experiments of Atkinson *et al.* (1969) and the numerical results of Friedmann *et al.* (1968). For $0 < Re < 50$ where the biggest discrepancies occur, the linear correlation Equation 2.4 is within 30% of Friedmann *et al.* (1968), while in the same range Equation 2.6 is within 15%. A number of more complex correlations exist (for example Dombrowski *et al.* (1993) and Durst *et al.* (2005)), which give better agreement with the results of Friedmann *et al.* (1968) for this range of Re, however the use of any of these correlations for low Re flows is questionable and is discussed later in Section 2.2.2 .

The discussion so far has been limited to the two most studied cases, flow in circular pipes and flow between parallel plates. Studies on flow through ducts of other cross-sections from example rectangles, triangles or trapezoids, are limited and no universal correlations exist for these geometries. Of particular interest in microfluidic flows are channels with rectangular cross-sections. Existing results from a number of authors for rectangular ducts are presented in Table 2.2. The general trend across all studies is that the high Reynolds number asymptote, C^+ decreases for increasing aspect ratio γ, however there are large differences between authors for a given aspect ratio and clearly no well established values exist.

Table 2.2: Values of the high Reynolds number asymptote $C^+ = L_e/D_h Re$, for rectangular ducts of different aspect ratio γ.

Author	γ 1	2	4	5	8	10
Theoretical						
Han (1960)	0.0752	0.066	0.0427	-	0.0227	-
Wiginton & Dalton (1970)	0.090	0.085	-	0.075	0.080	-
Tachibana *et al.* (1986)	0.090	0.0821	-	0.0477	-	-
Experimental						
Sparrow *et al.* (1966)	-	> 0.080	-	0.080	-	-
Goldstein & Kreid (1967)	0.090	-	-	-	-	-
Muchnik *et al.* (1973)	-	0.090	-	0.070	-	0.035

2.2.2 Flow with Non-Uniform Entrance Profiles

The uniform representation of the velocity profile at the inlet discussed in the previous section allowed for the flow field upstream of the duct to be decoupled from the flow within the duct. This provided a simplified and consistent starting point for the analysis of the entry flow problem that was considered to be a good approximation to many cases. However, due to effects that can occur upstream of the entrance, in reality the flow at the inlet often differs from a uniform profile (Beavers *et al.* (1970), Sparrow & Anderson (1977)).

In the low Re experiments of Atkinson *et al.* (1969) and Brocklebank & Smith (1968), $Re \leq 200$, a distributor was developed, which incorporated an annular region to force the flow towards the boundaries followed by a series of mesh screens used to straighten the flow and prevent boundary layer development before the channel entrance. Based on this design, Berman & Santos (1969) also incorporated a number of mesh screens and found that for low Reynolds number, $Re \approx 100$ the entrance length depended highly on the way the screens were used, and thus on the velocity distribution at the inlet. For $Re > 300$, the region very close to the entrance was affected by changes to the mesh screens, but the far field remained largely unchanged. This caused the measured entrance lengths to be the same as calculated by the methods described earlier for a uniform velocity entry.

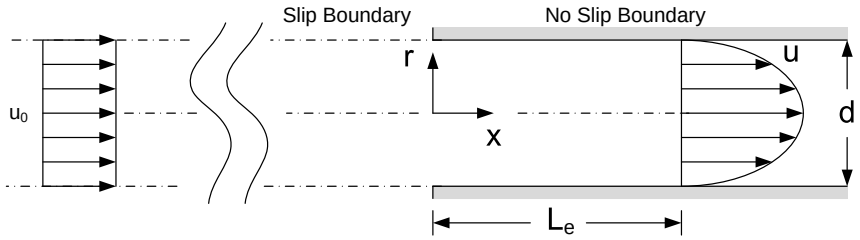

(a)

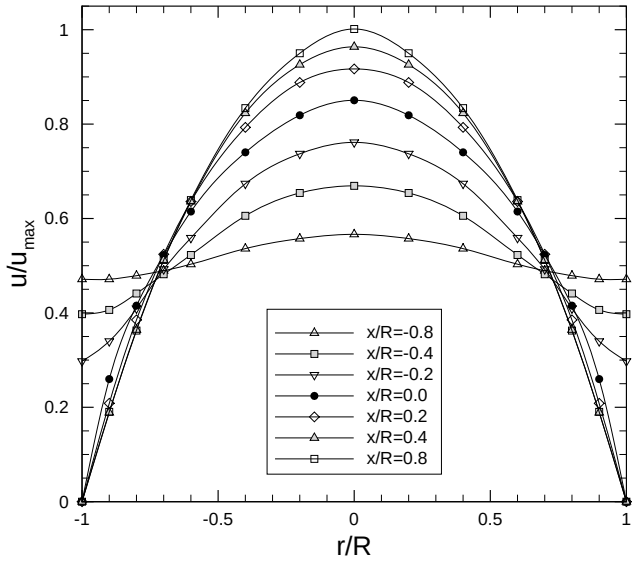

(b)

Figure 2.2: (a) Streamtube entry conditions. (b) Velocity profiles for $Re \to 0$, replotted from Figure 3 in Vrentas *et al.* (1966) using the streamtube entry condition.

Numerically this same effect was reported in the simulations of Wang & Longwell (1964) for $Re = 300$. In terms of the entry flow problem, this was the first rigorous solution of the full Navier-Stokes equations. In this work two different inlet conditions were examined for flow between parallel plates. The first was for a uniform velocity distribution at the inlet, and the second condition, referred to as a streamtube entrance, consisted of a region upstream of the entrance bounded by an impermeable frictionless wall (Figure 2.2(a)). A uniform velocity profile was applied to the entry of the streamtube, far upstream of the actual entrance.

This arrangement allowed the role of diffusion of momentum on flow development to be investigated in the upstream region of the entrance. Comparison of the two cases in Wang & Longwell (1964) revealed differences in the flowfield close to the entrance, but in terms the overall effect, such as the entrance length and total pressure drop, little difference was found between the two boundary conditions, for $Re = 300$.

Later, the streamtube condition was also applied to flow in circular ducts by Vrentas *et al.* (1966) and Christiansen *et al.* (1972) for a range of Re. The insensitivity of high Reynolds number flows to exact inlet conditions was also confirmed for $Re > 200$, which compared well with boundary layer solutions.

For lower Re however, the inlet conditions had a significant impact on the flow in the entire entrance region. A large amount of predevelopment was found to occur and the velocity distribution at the pipe entrance became highly developed. Velocity profiles from Vrentas *et al.* (1966) have been plotted in Figure 2.2(b) for $Re \to 0$, and it can be seen that the centreline velocity at the inlet is already greater than 85% of its fully developed value. This caused the corresponding entrance lengths to be considerably reduced, with the greatest reduction occurring at the lowest Re. Comparison of the data of Friedmann *et al.* (1968) with Vrentas *et al.* (1966) for the zero Reynolds number limit showed the entrance length was reduced from $0.6D$ to about $0.3D$; a decrease by a factor of 2. The results of the streamtube studies clearly indicate that at low Reynolds numbers a uniform velocity distribution at the entrance of a pipe is not a realistic approximation and can only be achieved in practice with considerable difficulty, as with the experiments of Atkinson *et al.* (1969), Brocklebank & Smith (1968), and Berman & Santos (1969).

The streamtube condition however is also rather artificial and the corresponding physical situation would be difficult to realize (Vrentas *et al.* (1966)).Therefore its results prompted the use of more realistic upstream geometries to study their impact on the flow at low Reynolds number. Flow between parallel plates was studied in the numerical work of Sparrow & Anderson (1977) and Sadri (2002), with flow entering from an infinite region through a squared edged entry. Sparrow & Anderson (1977) modelled the far upstream region as potential flow towards a sink, while Sadri (2002) modelled the same region as Jeffery-Hamel sink flow. The results of both studies echoed the findings of the streamtube entrance simu-

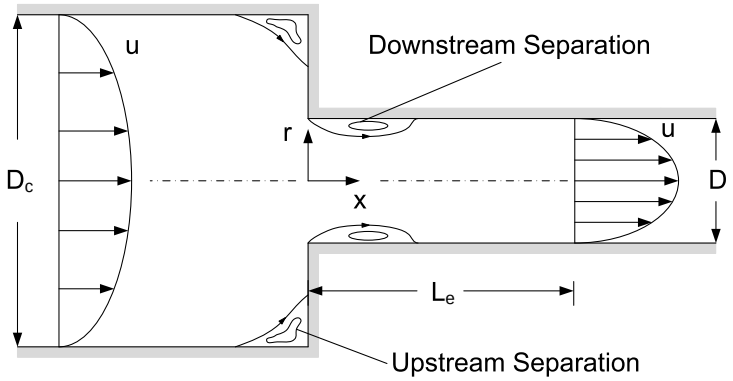

Figure 2.3: Sudden contraction entry condition.

lations, that at low Reynolds number the flow enters the pipe highly developed causing a reduction in entrance length compared with the results of a uniform entry condition.

Another inlet condition that has received a considerable amount of attention is the flow from a larger diameter pipe into a smaller diameter pipe through a sudden contraction, due to its importance in a number of practical applications. The arrangement is drawn in Figure 2.3 with a contraction ratio, B, given by D_c/D. Far upstream of the contraction, the flow inside the large pipe is fully developed and at a distance, L_e, downstream stream of the contraction the flow in the small pipe also becomes fully developed. Numerically this situation has been examined by Christiansen *et al.* (1972), Vrentas & Duda (1973), Kim-e *et al.* (1983), and Durst & Loy (1985) who also performed an experimental investigation. The results of these studies showed that the velocity profile at the entrance of the small pipe approaches that of uniform flow for $Re \geq 200$ and becomes more uniform for increasing contraction ratio B and increasing Re. For low Reynolds number flows the velocity profiles entered highly developed, in a manner very similar to the streamtube results of Vrentas *et al.* (1966) presented in Figure 2.2(b). The overall findings for the entrance lengths were that they were only a weak function of the contraction ratio, B, for all Re. Based on these works in the review of Boger (1982) the entrance length was concluded as independent of the contraction ratio B for $B \geq 4$ and for most practical purposes independent

of B for $B \geq 2$.

The discussion given in this section showed that a uniform velocity distribution at the inlet is not a realistic assumption for low Reynolds number flows. The results of studies for flow through a sudden contraction showed that the developing region is only weakly affected by small variations to the upstream region and that the streamtube model provides accurate results for real flows. With this in mind, Boger (1982) proposed the linear correlation,

$$L_e/D = 0.245 + 0.055Re \tag{2.8}$$

comprised on the creeping flow limit from the streamtube model, and the high asymptote, $C^+ = 0.055$.

2.2.3 Flow Phenomena in the Development Region

Two interesting phenomena have been reported to occur in experimental works and solutions of the full set of Navier-Stokes equations, namely an off centreline maximum velocity in developing velocity profiles and flow separation near the pipe inlet.

In the numerical simulations of Wang & Longwell (1964) velocity profiles just downstream of the entry of the pipe had a maximum velocity value that occurred off-centreline near both of the solid boundaries with a local minima occurring in between. This phenomena, now referred to as a velocity overshoot, was found by Wang & Longwell (1964) to be particularly distinguishable in the case of a uniform entry. These overshoots were confirmed in later numerical simulations using a uniform entrance profile by a host of workers including the numerical works mentioned earlier of Friedmann *et al.* (1968), Atkinson *et al.* (1969), and Morihara & Ta-Shun Cheng (1973). The overshoots in these numerical studies occurred even as $Re \to 0$, and increase in magnitude until a Reynolds number of about 200. The overshoots slowly decreased with further increases in Re above 200.

In the streamtube and sudden contraction studies the overshoots were far less noticeable and did not occur in very low Reynolds number flows. For flow through a sudden contraction Christiansen *et al.* (1972) reported overshoots for $Re > 30$, however Kim-e *et al.* (1983) suggested these results were caused by

insufficient numerical resolution and overshoots only occurred for $Re \geq 100$, which was supported by the work of Vrentas & Duda (1973). Experimentally Burke & Berman (1969) found overshoots for $Re > 100$ and $B = 4.67$, and Durst & Loy (1985) found overshoots for $Re > 234$ and $B = 1.87$. The magnitude of the overshoots in the sudden contraction studies was shown to increase with both the contraction ratio, B and Re. For flow between two plates Sadri (2002) found overshoots for $Re > 100$ and Sparrow & Anderson (1977) for $Re \geq 300$. These results all suggest that in engineering applications velocity overshoots do not occur for $Re << 100$, due to the diffusion of momentum through viscous action, which allows for sufficient development of the velocity profile before the entrance.

The flow phenomenon of separation has also been shown to occur inside of the pipe for sharp edged entries. When the flow separates near the entry of the duct, as shown in Figure 2.3, the flow is forced to accelerate in the region in between, known as the vena contracta. In the studies of flow through sudden contractions separation was found to occur at $Re > 150$ by Christiansen *et al.* (1972), $Re \geq 561$ by Durst & Loy (1985), and Vrentas & Duda (1973) found that separation did not occur for $Re \leq 200$. The separation region in these studies was shown to increase in size with increasing Reynolds number and increasing contraction ratio, B. For the flat plate studies of Sparrow & Anderson (1977) no separation region was reported for $Re \leq 100$, however Sadri (2002) found separation to exist for $Re > 365$. With the specific intention to examine both separation zones shown in Figure 2.3, studies have been performed for flow through a sudden contraction for parallel plate flow (Hunt (1990) and Hawken *et al.* (1991)). For a $B = 2$, Hunt (1990) found separation to occur for $Re \geq 500$, while in the work of Hawken *et al.* (1991) separation occurred in the range $300 < Re < 500$ for $B = 2$, and $200 < Re < 300$ for $B = 4$. The height of the recirculation zone when first detected is small, of the order of 1% of the channel diameter or plate spacing, growing to about 4-6% for $Re = 2000$ (Hunt (1990) and Durst & Loy (1985)). Much like the velocity overshoot, when separation first occurs it is hard to detect and unlikely to be present in flows of $Re < 200$, the realm of most microchannel flows.

2.2.4 Microchannel Entrance Studies

The description of developing flows in pipes so far covers the entire Reynolds number range. Renewed interest in the study of entrance flow from researchers connected with microfuildics occurred for two main reasons; to investigate various inlet conditions and geometries specific to microfluidic devices, and to evaluate any size effects that might be present at smaller length scales.

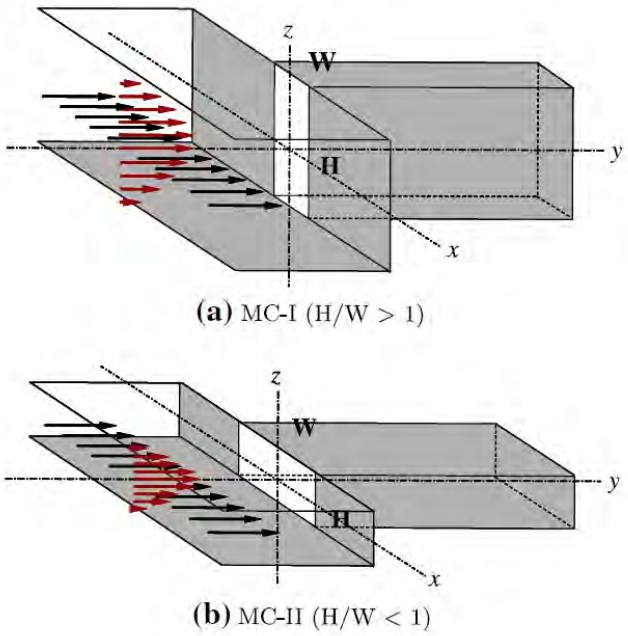

Figure 2.4: Diagram of the two planar entrance conditions used by and taken from Lee *et al.* (2008).

The effect of planar inlet plenums on developing flows was first investigated by Lee *et al.* (2002) and later in their follow up work Lee *et al.* (2008). Surfaces in common between plenum and duct were thought to allow the development of the boundary layers before the channel entrance and to reduce the length required to reach the fully developed state. In their first work, Lee *et al.* (2002) examined high Reynolds number flow into a rectangular channel $260\mu m$ by $690\mu m$ with the larger dimension in common with the plenum. The Reynolds numbers range was 250-2100 which allowed for the calculation of the high Reynolds number asymptote and a value of approximately 0.033 was calculated for all Re examined.

Compared to the values in Table 2.2, it represents at least a decrease of 50% of entrance length compared to flow with a uniform entry condition. Since there is no universal entrance correlation for rectangular ducts a more exact comparison can not be performed.

For low Reynolds number flows in rectangular ducts there is even fewer entrance length data available for comparison. Therefore in Lee *et al.* (2008) experiments were performed on two microchannels with approximately the same aspect ratio, however one had its longer side in common with the plenum and the other had its shorter side, as shown in Figure 2.4. The channel with the longer dimension in common with the plenum, developed in a substantially shorter distance than the channel with its shorter side in common with the plenum. The entrance lengths of the first arrangement were approximately half of those of the other arrangement for the Reynolds number range $1 < Re < 100$, clearly indicating the considerable influence that planar plenums can have on flow development for low Re flow.

A key point from the work of Lee *et al.* (2008) was in the calculation of entrance length. To experimentally determine the point along the centreline at which the velocity is within 1% of its fully developed value is a difficult task, particularly on the microscale since development lengths are short and channel geometries cannot be as accurately determined as in macro-scale experiments. Lee *et al.* (2008) fitted a curve to the centreline velocity of the form of a decaying exponential, viz,

$$u = C_1 - C_2 e^{-C_3 x} \tag{2.9}$$

in which C_1, C_2, C_3 are the constants to be determined. The asymptotic centreline velocity from the curve fit is C_1, and therefore the entrance length, L_e, is the x-location that produces $u = 0.99C_1$. This method allowed calculation of both the fully developed velocity on the centreline and the location at which 99% of that value is reached based on a large number of velocity measurements, which greatly improves the accuracy of the calculation.

While not as detailed as the above two studies, a few other studies with planar geometries have received attention. Lee & Kim (2003) examined the effects of rounded inlet conditions at low $1 < Re < 10$ and showed that a significant

reduction in resistance to the flow occurred in channels with rounded entries. Hsieh *et al.* (2004) examined flow into a rectangular channel $115\mu m$ deep and $200\mu m$ wide and for $50 < Re < 240$. The entrance length was described in dimensionless form as $L_e/D_hRe = 0.012$, which is much shorter than predicted from the results from in Table 2.2. Unfortunately no details were provided in terms of the calculation of L_e.

Using pressure based methods Costaschuk *et al.* (2007) made an estimate of entrance length for flow in a rectangular duct with an aspect ratio of 12.7 ($91.3\mu m$ by $1161.5\mu m$). For Reynolds numbers in the range $500 < Re < 1000$ a large variation in the high Reynolds number asymptote, C^+, was reported, being almost tenfold in range, making it difficult to draw any definite conclusions about the results.

Entrances to microchannels with sharp inlets have also been investigated. Thompson *et al.* (2005) performed experiments with flow entering in circular cross-section tubes of $182\mu m$ diameter for the Reynolds number range, $60 \leq Re \leq 350$. Their capillary tube protruded out into the reservoir and was described as representing a sudden contraction with an infinite contraction ratio. For flow with the two largest Reynolds numbers of 290 and 350, a re-circulation region was found to appear just after the entrance. The authors concluded this was a scale effect but these Reynolds numbers fall well within the plausible range for the occurrence of separation based on the discussion in previous section. Entrance lengths expressed as L_e/DRe were approximately 0.05 for all Re, which agrees with conventional theory, however no strict criterion was applied to determine this value.

Recently Ahmad & Hassan (2010) studied entry flow in conduits with square cross-sections with widths of $100, 200, 500\mu m$ where, each had a squared edged inlet in order to explore possible scaling effects. The glass capillaries were glued to the lower surface of a reservoir with the end of the capillary in line with one of the reservoir walls as can be seen in Figure 2.5. The entrance of the capillary was located at least 50 'widths' from boundaries other than the lower surface, which was separated from the capillary by a thickness of its wall. Instantaneous velocity fields were measured using MicroPIV in the centre plane of the channels. Developing profiles were presented for all three of the capillaries at four different Reynolds numbers in the range $0.5 < Re < 200$. The velocity profiles exhibited

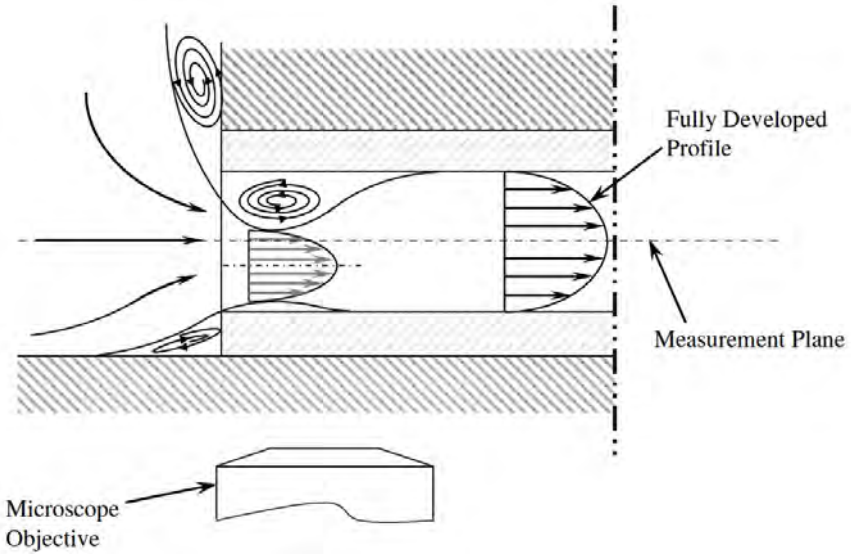

Figure 2.5: Schematic diagram of the entrance conditions used in and taken from Ahmad & Hassan (2010).

a number of interesting features, particularly in the results of the smaller two capillaries. In many Reynolds number cases large off centre maxima occurred at the entrance, even for a Reynolds number as small as 0.5, and large asymmetries also were present in a number of the velocity profiles. The velocity along the centreline at the entry was also much lower than would typically be expected, as low as 20% of its fully developed value in one case.

These features were explained by the occurrence of asymmetric flow separations at the inlet, as depicted in Figure 2.5, thereby forcing the maximum velocities off the center plane and outside of the plane of measurement. The re-circulation zones were not measured or observed, but inferred to exist at all Reynolds numbers. The suggestion of separation at a Re as low as 0.5 is quite surprising, and for it to have such a significant impact on the velocity profiles a particularly interesting finding when typically the size of the recirculation zone are only a small fraction of the pipe diameter. Unfortunately, no images or measurements were made of the geometry of the entrance region, which makes alternate explanations of the phenomena difficult. It should be pointed out however, that there is no other data in the literature available for comparison for entry flow into a square duct at such low Reynolds numbers.

A number of other geometric flow arrangements have been studied. Hao *et al.* (2005) measured velocity profiles in the entrance region of a trapezoidal channel with a hydraulic diameter of $237\mu m$. For the flow in the range $50 < Re < 1200$, the entrance length correlation was described by the linear fit $L_e/D_h = 0.084Re$. Oak *et al.* (2004) examined the distance for two co-flowing streams in a rectangular duct once introduced at the end of a divider plate to become fully developed. It was shown that a velocity differential between the two streams caused significant transverse velocities, which greatly increased the length required for the flow to reach a fully developed state. The studies by Hao *et al.* (2005) and Oak *et al.* (2004) were both conducted with configurations specifically important to microfluidic devices. Another such arrangement, which has received no attention in literature on the microscale, is that of oscillatory entry flow.

2.3 Oscillatory Flow in the Entrance Region of a Channel

Generally speaking, the expression 'oscillatory flow' can be used to describe any flow where a harmonic component makes up a substantial part of the flow. Oscillatory flow of this type occurs in many industrial applications such as in the exhaust of reciprocating pumps and engines, in hydraulic lines and control systems. As discussed earlier it is particularly prevalent in microfluidic devices, and of course in biological systems. Oscillatory flow development in the entrance region of a conduit is particularly important in arterial flow (Ku (1997)), where due to frequent branching of arteries the flow is rarely free from entrance effects (Chang & Atabek (1961)).

Oscillatory flows are usually divided into two classes, flows in which the flow rate oscillates as a sinusoid in time about a mean value of zero, referred to as oscillatory flow and pulsatile flow where there is a sinusoidal variation about a mean value other than zero. Therefore oscillatory flow is used in two ways; to broadly describe any flow with a harmonic component, and also to refer to the specific subcategory of this flow, which has a zero time mean. This definition is prevalent in the literature, and also has been adopted for the current work.

The characteristics of unsteady flows differ substantially from those found in

steady flows and therefore the general properties of fully developed oscillatory flow are first described, followed by the more complicated problem of developing oscillatory flow in the entrance region of a duct.

2.3.1 Characteristics of Oscillatory Flow

An illustrative problem of oscillatory flow is that of a fluid above an infinite flat plate undergoing harmonic oscillations, $U_0 cos(\omega t)$, parallel to itself. This problem was first studied by Stokes and is now known as Stokes' second problem (Schlichting & Gersten (2000)). The solution is given by:

$$u(y,t) = U_0 e^{-\eta} cos(\omega t - \eta) \tag{2.10}$$

which has the form of damped harmonic motion. Here U_0 is the velocity amplitude of the plate, ω is the angular frequency and η given by:

$$\eta = y\sqrt{\frac{\omega}{2\nu}} \tag{2.11}$$

which has been plotted in Figure 2.6. Examining Equation 2.10, as done by

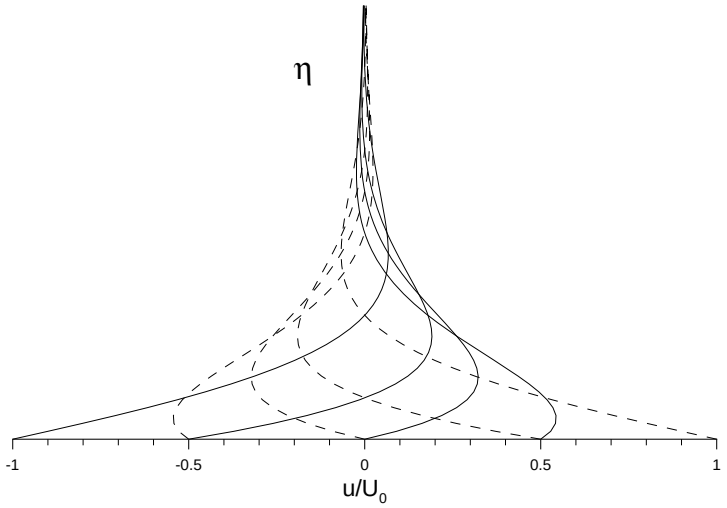

Figure 2.6: Flow above an oscillating flat plate at various times given by Equation 2.10.

White (1991), the location from the plate where u oscillates with an amplitude of $0.01U_0$, gives $e^{-\eta}$=0.01 or $\eta = 4.6$. Therefore we arrive at a definition of an oscillating boundary layer thickness, given by

$$\delta_{os} \approx 6.5\sqrt{\frac{\nu}{\omega}} \tag{2.12}$$

i.e. the layer of fluid which is carried by the wall has a thickness of the order $\delta_{os} \sim \sqrt{\nu/\omega}$. It can be seen that this oscillating boundary layer thickness, δ_{os}, decreases with decreasing kinematic viscosity and increasing frequency. Flow of a fluid whose velocity oscillates in a duct introduces an additional length scale to that of a oscillating plate, namely the pipe radius, r, or halfwidth a for rectangular ducts. The ratio of the pipe radius, r, to oscillating boundary layer thickness, δ_{os}, is defined as

$$\alpha = r\sqrt{\frac{\omega}{\nu}}, \tag{2.13}$$

which is the non-dimensional parameter that characterises oscillatory duct flows. The parameter α is known as the Stokes number, or in biomechanics the Wormsley number (Fung (1997)). Sexl (1930) was the first to derive an analytic solution to laminar oscillatory flow in a circular pipe under fully developed conditions, which took the form,

$$\bar{u} = \bar{u}_{os} sin(\omega t) \tag{2.14}$$

or equivalently

$$\bar{u} = \bar{u}_{os} sin(\theta). \tag{2.15}$$

Here $\bar{u}_{os}$ is the oscillatory amplitude of the cross-section average velocity and θ is the phase angle (where $\theta = \omega t$). Later this problem was also solved by Womersley (1955) and Uchida (1956).

In Figure 2.7, the solution of Womersley (1955) has been plotted for four different values of α. At low values of α, the instantaneous velocity distribution is almost the same as that in steady Hagen-Poiseuille flow so that it can be

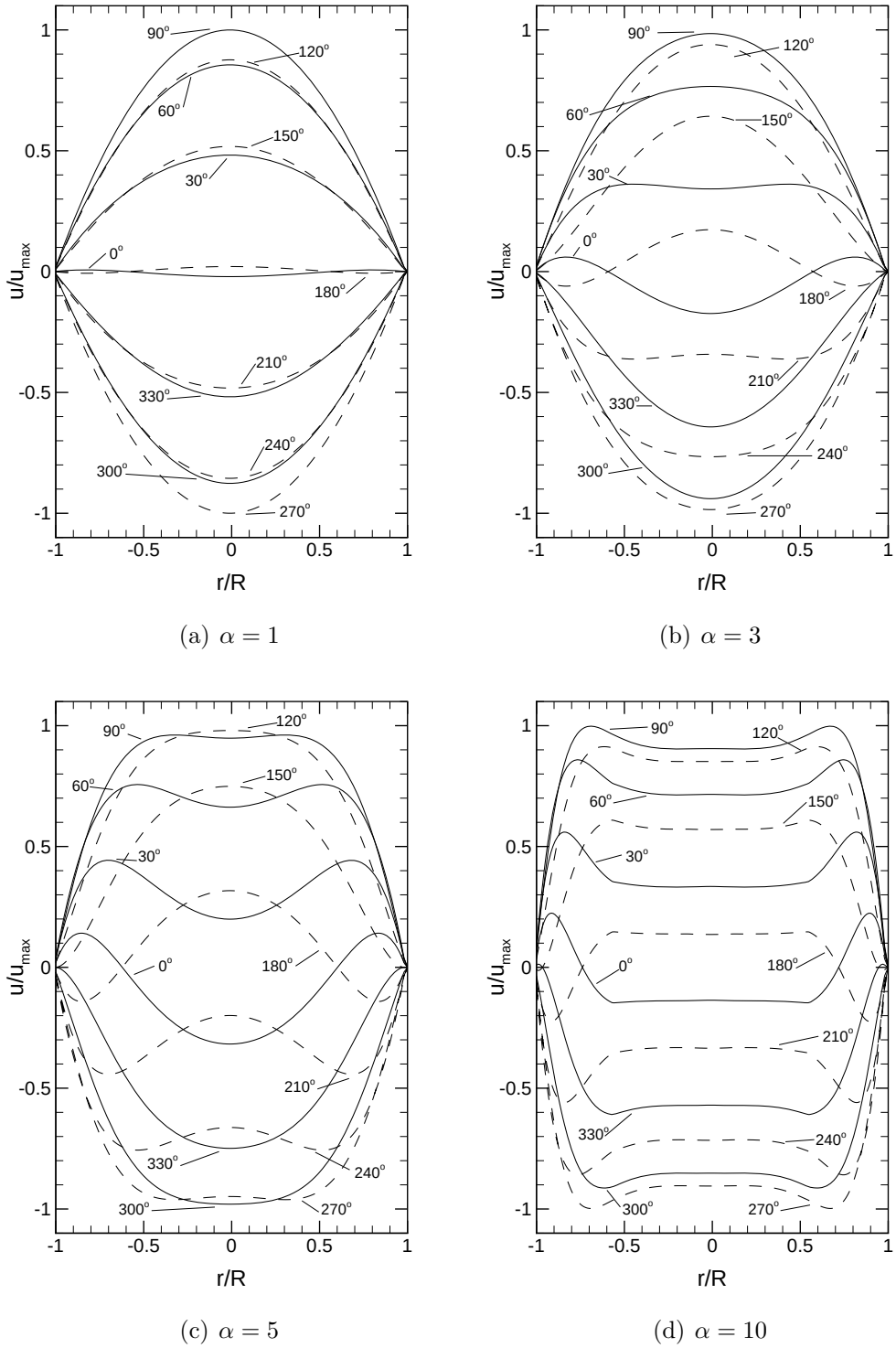

(a) $\alpha = 1$

(b) $\alpha = 3$

(c) $\alpha = 5$

(d) $\alpha = 10$

Figure 2.7: Velocity profiles for fully developed oscillatory flow in a circular duct, for various Stokes number, α.

referred to as quasi-steady Hagen-Poiseuille flow, see Figure 2.7(a). As the Stokes number is increased, due to the inertia of the fluid, the flow on the centreline of the duct lags behind the flow nearer to the wall (Figures 2.7(b) and 2.7(c)). Interestingly at phase angles $\theta = 0^o$, and $\theta = 180^o$, where the average velocity over the cross-section is zero, the flow is segmented into region travelling in both directions. At large α, (Figure 2.7(d)) the solution has a form typical of boundary layers (Schlichting & Gersten (2000)) and the flow is said to have an oscillating boundary layer with an inviscid core. The maximum value of velocity no longer occurs on the axis of the pipe, but lies closer to the wall, an effect first noted in the experiments of Richardson (1927). It is now called *Richardson's annular effect* in his honour but is also referred to as the velocity overshoot, just as with the case of steady entrance flow.

Fully developed laminar oscillatory flow in a rectangular duct was first solved by Drake (1965), and shortly after by Fan & Chao (1965). A number of solutions now exist, each with their own nuances, which have been discussed in Yang *et al.* (2003). Under fully developed conditions, the resultant flow equations are linear and therefore other fully developed solutions can be superimposed. For example, the solution to fully developed pulsatile flow of the form,

$$\bar{u} = \bar{u}_s(1 + Asin(\omega t)) \tag{2.16}$$

in which $\bar{u_s}$ is the steady component of flow and the constant A is the ratio of the amplitude of oscillatory to steady flow $\bar{u}_{os}/\bar{u}_s$, is simply the summation of the fully developed steady and oscillatory flow solutions. Similarly, when modelling arterial flow a number of harmonics or different α numbers can be superimposed (Hale *et al.* (1955)). The ratio of the average velocity amplitudes, A, in the fully developed region then describes the relationship between the oscillatory velocity profiles seen in Figure 2.7 and the well known parabolic steady profile.

For $A > 1$ there are periods in an oscillation cycle where there is a reversal in the direction of the mean flow. For $A < 1$ however, the flow at certain locations within the duct cross-section may also reverse direction, depending on both A and the Stokes number. Figure 2.8 shows the smallest value of A for which flow reversal occurs at any point within a circular duct in the fully developed region. For small α, the profiles are quasi-steady and an amplitude ratio of greater than

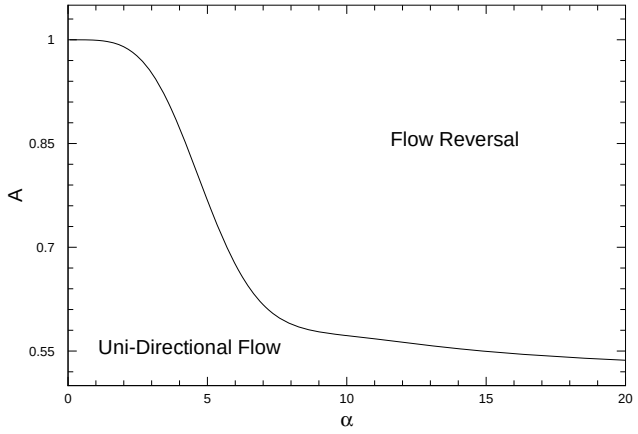

Figure 2.8: Conditions for flow reversal in the fully developed region of pulsatile flow, $\bar{u} = \bar{u}_s(1 + Asin(\omega t))$.

one is required for flow reversal to occur. For larger Stokes numbers, more of the flow is distributed towards the duct walls and flow reversal occurs at much lower values of A, approaching a value of approximately 0.5 for large α.

The characteristics of oscillatory flows described in this section depend on the non-dimensional parameters, α and A. In the entrance region, as with steady flow, oscillatory flow also depends on the Reynolds number. The concept of the entrance region is not as 'straight forward' in the case of oscillatory flow and the concept of entrance length will now be re-visited.

2.3.2 Entrance Length Definition for Time Dependent Flow

The entrance length for time dependent flows has been studied for flows with a oscillatory component (Atabek & Chang (1961)) and impulsively starting from rest (Atabek (1962)). Under these conditions a definition of the entrance length based on the flowfield is also a function of time. That is for every instant in time, there is a distance, L_e from a designated inlet to where the properties of the flow such as velocity distribution, wall shear stress and pressure gradient all vary minutely with further distance downstream. As little work has been done on time varying entrance flows, there is no established definition of entrance length for flow under these conditions.

In the case of pulsatile flow, two variations of the definition of entrance length have been used in the literature. In the very first study of time dependent entry flow, Atabek & Chang (1961) derived an approximate analytical solution for pulsatile flow in a circular pipe and used it to determine a time varying entrance length. They defined L_e as the distance from the entrance at which the difference between the instantaneous centreline velocity and its value in the fully developed flow region, when divided by the time averaged centreline velocity, $2\bar{u}_s$, was less than 1%.

Krijger *et al.* (1991) used the same definition as Atabek & Chang (1961) but also applied a second definition for the entrance length, which was a more direct application of the steady flow definition. The entrance length was defined as the distance from the inlet to the location downstream where the centreline velocity was within 3% of the fully developed centreline velocity at that instant in time. Therefore all values in the calculation are instantaneous values, unlike Atabek & Chang (1961) who incorporated a time averaged value, $2\bar{u}_s$.

The sole reason given for use of the first definition by Atabek & Chang (1961) rather than the more rigorous approach adopted by Krijger *et al.* (1991), was in order to simplify calculations and not for some underlying physical reason. Following Atabek & Chang (1961), He & Ku (1994) in a later study employed the same definition. However, it is argued here that the definition of Krijger *et al.* (1991) is a more consistent definition, and importantly, for quasi steady flow this definition yields an entry length equivalent to the instantaneous steady entrance length for the same percentage limit. Furthermore, it can be extended to all time dependent flows without modification, unlike the definition of Atabek & Chang (1961). For that very reason even Atabek (1962) employed a definition consistent with that of Krijger *et al.* (1991) for flow starting impulsively from rest, that only involved instantaneous velocities.

For oscillatory flow with no mean component, a range of definitions of the entrance length have also been used. Gerrard & Hughes (1971) applied a 1% criteria to the centreline velocity using instantaneous values, while it appears Raju *et al.* (2005) applied the same criteria to the cross-section location where the peak velocity occured. Yamanaka *et al.* (2002) defined the entrance length as the distance where the third harmonic had decayed to zero and Jaworski *et al.* (2009) modified the definition given by Atabek & Chang (1961), replacing $2\bar{u}_s$

with $\bar{u}_{os}$. These variations used make comparison of results between different authors difficult, as well as comparison with other flow types.

2.3.3 Oscillatory Flow Entrance Length Studies

In the study of oscillatory flows in the entrance region, numerous attempts have been made to characterise the flow using a variety of different approaches, each of which is driven by essentially the same idea.

Gerrard & Hughes (1971) suggested that in oscillatory flow the hydrodynamic entrance length would be shorter than in steady flow, as the retarding effects of the wall need only diffuse over the oscillating boundary layer thickness, δ_{os}, rather than the entire pipe radius as in steady flow. The oscillating boundary layer thickness, δ_{os}, used by Gerrard & Hughes (1971) and in the follow up work by Kassianides & Gerrard (1975), was defined as the distance from the wall at which the velocity is within 1% of the velocity at the centre of the duct, at that instant in time. δ_{os} was calculated from the analytic solution. In order to calculate an entrance length, it was proposed that correlations based on Reynolds number for steady flow would apply to oscillatory conditions as a function of time. For this to apply the length scale was replaced by the oscillating boundary layer thickness, δ_{os}, and the velocity scale by the instantaneous average velocity, $\bar{u}$. This approach gives the oscillatory entrance length, L_e in time as being proportional to $\bar{u}\delta_{os}^2/\nu$ rather than $\bar{u}D^2/\nu$ for steady flow, representing a reduction $\sim \delta_{os}^2/D^2$ for large Stokes numbers (Gerrard & Hughes (1971)). For low α, viscosity affects the entire duct cross-section and the entrance lengths are suggested to become as large as in steady flow (Kassianides & Gerrard (1975)).

For large values of α, essentially the same general idea based on an oscillating boundary layer was suggested by Caro *et al.* (1978), and later entered other biomechanics textbooks (such as Fung (1997)). The difference in this approach was that the oscillating boundary layer thickness, δ_{os}, was taken from the solution of Stokes to the oscillating plate problem, given in Equation 2.12. Using the boundary layer solution of Blasius for steady flow along a flat plate, the boundary layer as a function of distance along the plate was calculated as

$$\delta = 3.5\sqrt{\frac{2\nu x}{u_\infty}} \tag{2.17}$$

where u_∞ is the freestream velocity and δ is the distance from the wall to the location where $u = 0.99u_\infty$ [1]. Substituting for δ_{os} from Equation 2.12 in Equation 2.17 and re-arranging yields the entrance length, L_e, as,

$$L_e = 1.7u_\infty/\omega. \tag{2.18}$$

Interestingly Equation 2.18 is independent of the duct diameter and as well as viscosity. The approach of Gerrard & Hughes (1971) is equivalent to Caro *et al.* (1978) with the assumption that $\delta_{os} \approx \sqrt{\nu/\omega}$. The term u_∞/ω in Equation 2.18 has the dimension of a length and can be viewed as a 'stroke' length or as the axial migration distance of a fluid particle during a cycle. As a consequence, Iguchi *et al.* (1992) defined the entrance region in oscillatory flow as the the maximum distance a fluid particle could travel into the pipe from the inlet before reversing. Therefore the fully developed region became the section of pipe that fluid particles entering the pipe could never reach. Iguchi *et al.* (1992) suggested this definition was a good approximation of the conventional entrance length for oscillatory flows based on data from experiments performed for $\alpha \geq 6.9$, however no strict criteria were applied in this comparison so that their conclusion was really only qualitative.

The only comprehensive set of data available for a quantitative comparison of the scaling of the oscillatory entrance length, are the numerical results of Raju *et al.* (2005). In this work, flow with a uniform velocity distribution at the inlet but varying sinusoidally in time between two of the parallel plates was studied over the extensive parameter space $79 < Re_{os} < 1570$ and $2.5 < \alpha < 15.9$. Here the oscillating Reynolds number is expressed,

$$Re_{os} = \frac{\bar{u}_{os}D}{\nu}, \tag{2.19}$$

and is based on the average velocity amplitude, $\bar{u}_{os}$. Raju *et al.* (2005) considered the entrance length as a function of phase angle, θ, and the non-dimensional entrance length, L_e/D, was presented for all Re_{os} studied by them. One set of results as a function of θ is plotted in Figure 2.9(a) for $Re_{os} = 79$. Here a substantial decrease of the entrance lengths can be seen for increasing α. Interestingly,

[1] In Caro *et al.* (1978) the numeral 2 is missing from inside the square root of Blasius's result.

for Stokes numbers $\alpha > 2.5$, the entrance length increased approximately linearly with phase angle and the maximum value occurred at $\theta = 180^o$, when $\bar{u} = 0$.

The approach of Gerrard & Hughes (1971) and Caro *et al.* (1978) discussed previously for the entrance length at large α to be based on δ_{os} suggests that

$$L_e/D \sim \bar{u}/\omega D = \frac{1}{St} \tag{2.20}$$

where St is the Strouhal number. The scaling of L_e/D with the inverse of St was the scaling proposed by Raju *et al.* (2005) for cycle averaged entrance lengths. The inverse Strouhal number can be formed from a combination of the Reynolds and Stokes numbers, viz, $1/St = Re/\alpha^2$, and therefore the high Reynolds number asymptote can be evaluated as

$$C^+ = \frac{L_e}{DRe_{os}} \sim \frac{1}{\alpha^2} \tag{2.21}$$

and a function of α only. The maximum value of entrance length for each case studied by Raju *et al.* (2005) has been extracted and normalised, L_e/DRe_{os}, and is plotted in Figure 2.9(b) against α. The two highest Reynolds number cases have been collapsed by this scaling, and therefore as with steady flow, the maximum oscillatory entranc elength becomes essentially linear with respect to Reynolds number for $Re > 200$. Also shown in Figure 2.9(b) is the high Reynolds number asymptote, $C^+ = 0.044$ for steady flow between parallel plates. The reduction from this line for oscillatory flow is expected to be proportional to δ_{os}^2/D^2 (Gerrard & Hughes (1971)) or $1/\alpha^2$ according to Equation 2.21.

In Figure 2.9(b), $1/\alpha^2$ has been plotted as the solid line, and the reduction of entrance length is indeed well captured by this scaling, particularly for Stokes number greater than 5. A constant of proportionality for Equation 2.21 of approximately 0.6 gives a good fit to the high Re and high Stokes number results, and is plotted as the dashed line in Figure 2.9(b). The idea that at low Stokes numbers, $\alpha \leq 2.5$, the entrance length becomes as large as in steady flow appear to be correct in Figure 2.9(b). For $\alpha = 2.45$, the result lie very close to the high asymptote from stead flow, $C^+ = 0.044$. In fact, all three entrance lengths for this Stokes number, are within 5% of the parallel plate correlation of Chen (1973), given by Equation 2.7 using Re_{os}. It should be pointed out that perhaps

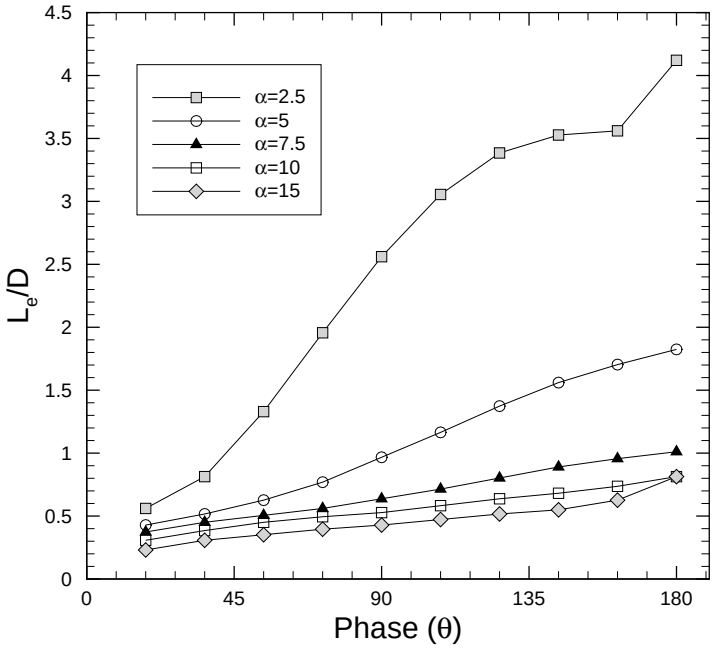

(a)

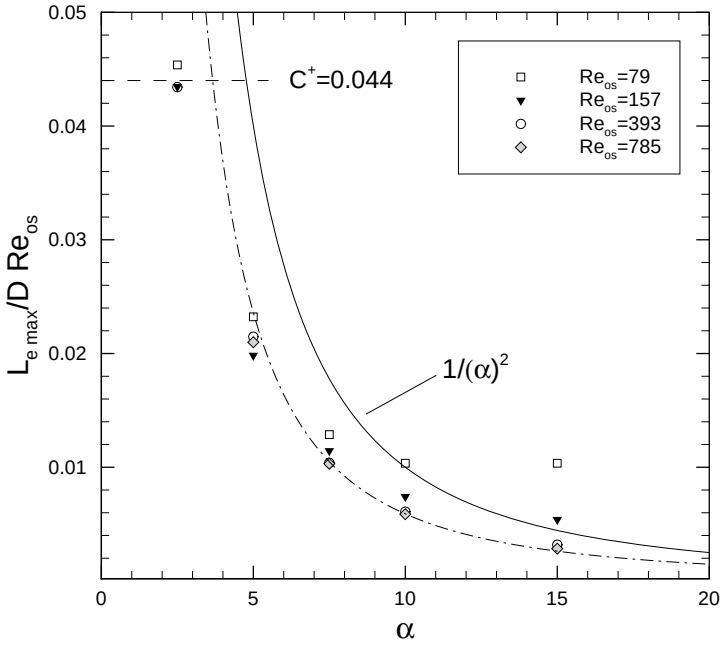

(b)

Figure 2.9: Entrance lengths obtained from Raju *et al.* (2005). (a) Entrance length, L_e/D against phase angle, θ for varying Stokes number, α and $\Re_{os} = 79$. (b) Maximum entrance length, $L_{e_{max}}/DRe_{os}$ against α.

surprisingly this maximum entrance length did not occur at the phase angle, θ, where the peak average velocity, $\bar{u}_{os}$ occured, but at $\theta = 180^o$. Despite this it was still accurately described by the steady flow correlation and a Reynolds number based on peak flow, $\bar{u}_{os}$. It can also be concluded from Figure 2.9(b) that the entrance length over the entire range of Reynolds numbers and Stokes numbers, requires more than just a single parameter such as the Strouhal number for its determination.

Experimental work on oscillatory flow in the entrance region is extremely limited but also agrees with the suggested scaling for large Stokes number flows. Gerrard & Hughes (1971) studied the entrance lengths in time for a single case with $\alpha = 14.4$ driven by the simple harmonic motion of a piston. A method similar to hydrogen bubble visualisation was used, incorporating a pH indicator to produce bands of colour that travelled with the fluid. Four phases angles in the cycle were measured, and when normalised in the manner proposed, showed qualitative agreement with their own theory. More recently, using Particle Image Velocimetry (PIV), Jaworski *et al.* (2009) examined entrance conditions in a parallel plate stack subjected to oscillatory flow when $\alpha = 23.6$ and $Re_{os} \approx 640$. The flow field measurements highlighted the rich flow patterns that can exist in oscillatory flows, with vortices found to exist both inside and outside of the stack. Due to the difficultly involved in calculating the entrance length from the experimental data, numerical simulations were performed for a number of different plate spacings. For large values of α, the entrance lengths determined from the numerical simulations were found to be independent of the plate spacing as suggested by Equation 2.18.

The one exception to these trends was the work of Yamanaka *et al.* (2002), in which the Ultrasonic Velocity Profile (UVP) measurement method was used to investigate oscillatory flow generated by a piston in a circular tube. An entrance length was determined for a single case that was described as weakly turbulent. Contrary to all of the previous works cited, they concluded for oscillatory flow that as the boundary layer becomes thinner, the entrance length becomes longer than in steady flow. All other studies found in the literature suggest the entrance length should be equal to the steady flow entrance length for low α and decrease with increasing α or equivalently with decreasing boundary layer thickness, δ_{os}, for large α.

2.3.4 Pulsatile Flow Entrance Length Studies

In pulsatile flows there is the interaction between the steady and oscillatory flow components described by the ratio of their amplitudes, $A = \bar{u}_{os}/\bar{u}_s$. The two flows are additive in the fully developed region, but in the region of interest, the entrance region, the governing equations are non-linear, and so their interaction is expected to be more complicated. The development of steady flow and its features are well established, and so the results of developing pulsatile flows are normally discussed in terms of the affect that the oscillatory component has on the developing steady flow.

The entrance length for pulsating flow was first studied analytically by Atabek & Chang (1961) for flow in a circular pipe. The boundary layer equations were linearized by assuming that the instantaneous velocity of the convective terms was equal to a constant value throughout the pipe (the Oseen approximation (Krijger *et al.* (1991))). This value was equated to that of uniform flow at the inlet varying periodically in time. A calculation was performed as an example by Atabek & Chang (1961), for the condition of $A = 0.5$, and $\alpha = 4$, which has been replotted in Figure 2.10. The entrance length in this case oscillates in time about the steady flow value.

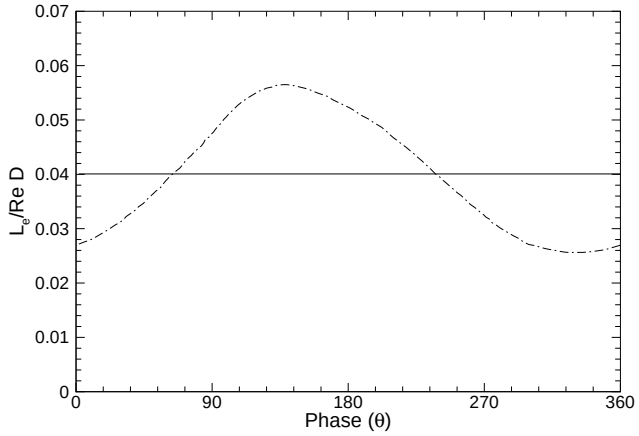

Figure 2.10: Non-dimensional entrance length against phase angle θ. Replotted from Atabek & Chang (1961). Dashed line is for pulsatile flow, $\bar{u} = \bar{u}_s(1 + Asin(\omega t))$, $A = 0.5$ and $\alpha = 4$. Solid line is their solution for the steady flow component.

The amplitude of oscillation of the entrance length about the steady flow value in pulsatile flow is affected by the Stokes number in the same way as the entrance length in purely oscillatory flows (Krijger *et al.* (1991) and He & Ku (1994)). Krijger *et al.* (1991) and He & Ku (1994) solved the full Navier-Stokes equations for pulsating flow in parallel plates and a circular pipe respectively, for uniform velocity conditions at the entrance. For $\alpha \leq 2$, the entrance length oscillates in a quasi-steady manner and is well approximated by steady flow correlations based on the same instantaneous average velocity. For increasing α, the amplitude of the entrance length is reduced and occurs at a later phase angle in the cycle, (for example in Figure 2.10, the maximum entrance length occurs well after peak flow, $\theta = 90^o$). Both Krijger *et al.* (1991) and He & Ku (1994) also reported that entrance lengths were approximately a linear function of Reynolds number based on steady flow, for $Re \geq 75$.

The effect of the oscillatory component on the mean flow in the entrance region has largely been studied for $A \leq 1$, that is for flow with a steady component greater than the oscillatory component. The effects under this condition have been shown to be minimal. In the simulations performed by He & Ku (1994), throughout the entrance region the velocity along the centerline was reported to vary sinusoidally in time for all α. When the mean centreline velocity was examined, its development along the pipe was largely unaffected by variation of the Stokes number. Cho & Hyun (1990), who numerically solved the boundary layer equations for the pulsating conditions, $0 \leq A \geq 0.3$ and $0 \leq \alpha \leq 15$, found the mean flow fields in the entire entrance region to be essentially unaffected by the oscillating component. A similar finding was made by Florio *et al.* (1968) experimentally for $\alpha = 6, 21$, $A = 0.4$ and $Re \approx 200$. Within experimental error, Florio *et al.* (1968) found that the time-averaged flow developed as steady flow for the same average velocity.

Only Chan *et al.* (2002) numerically studied the case of the velocity amplitude ratio, A, having values greater than 1. This work was also the only work performed at low Reynolds number with $Re = 30$. For $0.1 \leq A \leq 2.5$, unlike Cho & Hyun (1990), the mean developing fields for the different values of A, were found to be noticeably different from each other. Differences was found in both the developing velocity profiles and also in the mean axial friction factors. It is not clear how Chan *et al.* (2002) reached the same conclusion, that the oscillatory

component had negligible affect on the developing mean flow, to that of Florio *et al.* (1968), He & Ku (1994), and Cho & Hyun (1990).

Experimentally the situation is very similar to oscillatory entrance flows and experimental results for pulsatile conditions are few and limited to low values of A and high Reynolds numbers. Atabek *et al.* (1964) made hot film anemometry measurements for a single case of pulsating flow, $A = 0.344$, $Re = 1500$ and $\alpha = 5$. Good agreement between their analytical solution and experimental results was obtained for the developing velocity profiles. Denison *et al.* (1971) found that the analytical solution of Atabek & Chang (1961) predicted shorter development lengths compared with Laser Doppler Velocimetry experiments for $A = 0.16$, $Re \approx 1000$ and $4 \leq \alpha \leq 6$. The discrepancy between the results is arguably a scaling issue, as in the experiments of Denison *et al.* (1971), the reported mean fully developed centreline velocity is also a value lower than expected. The experimental work performed by Florio *et al.* (1968) already mentioned also agreed with the approximate solution of Atabek *et al.* (1964), and it can be concluded that this solution is a good approximation for flows with high Reynolds numbers and small relative oscillating component, A.

2.4 Summary

From the preceding literature survey, a number of key issues have been identified and can be summarised as follows:

The most current research on the flow of liquids in microchannel suggests conventional theories, such as the continuum hypothesis and no-slip condition, should apply in the majority of microscale flows. From the existing experimental studies it has been shown that it is paramount for experimentalists to accurately determine the geometric features of the devices employed when working on the microscale. According to Steinke & Kandlikar (2006), 'There is no substitute to accurate measurements obtained through destructive measurement of the channel geometry.'

Interfacing microfluidic devices with other macro-sized components is a challenging task that is an avenue of research in itself. The design of the entire fluidic system can have a large effect on the flow within the microdevice due to compliance effects of connecting tubes and trapped air within fluid lines. There-

fore, careful design of the microfluidic device is not only required for reproducible experiments, but of the entire system it interacts with.

There has already been much work performed on steady flow in the entrance region of a channel. Despite this there are no universal correlations that exist to accurately predict the entrance length in rectangular ducts. Moreover, regardless of duct cross-section, conventional correlations are not accurate for low Reynolds number flows, $Re < 50$, as they assume a uniform entrance profile, which is not a realistic entrance condition for these flows. Only the relatively unknown linear correlation proposed by Boger (1982) for flow in a circular pipe takes this effect into account. The streamtube model has been identified as a far better model for prediction or further numerical work on low Re flows.

Recently there have been a number of studies of entry flows on the microscale. In the vast majority of these studies no strict criteria was applied to determine the entrance length (Lee *et al.* (2008) being one of the exceptions), or at the very least, significant details are missing about its calculation. Unfortunately, very often the physical geometry of the entrance region is also not measured or characterised. These factors make it difficult to draw definite conclusions from these works, or place confidence in their results. For a fundamental problem such as the entrance length, sufficient details about its determination and all experimental details should be given in future works.

Only small amount of work has been performed on oscillatory flow in the entrance region of a channel. Theoretical considerations and numerical results show that there is reduction in entrance length compared with steady flow for large Stokes numbers, $\alpha > 3$, in both oscillatory and pulsatile flows. For $\alpha < 6$, the entrance length varies significantly in time over an oscillation cycle. It has been suggested that for low Stokes numbers, $\alpha < 3$, the maximum entrance can be determined by the steady flow entrance length correlations when a Reynolds number based on peak flow is used (He & Ku (1994), Gerrard & Hughes (1971)). These suggestions are partly supported by numerical results but currently there has been no systematic experimental study of these flows.

2.5 Objectives and Outline

Based on the summary of open literature just given the following objectives were established for this research:

To experimentally investigate and characterise steady flow in the entrance region of a microchannel under conditions most relevant to microfluidic devices. The selected conditions for the current work, are flow at low Reynolds numbers ($Re < 100$) with a planar entry fabricated using traditional micromachining techniques.

Generate high quality experimental results that complement the existing literature on entrance region flows, which has largely been analytical and numerical in nature. This includes, demonstrating the accuracy of the measurement technique, explicitly detailing the methods utilised to calculate the entrance length, and the accurate characterisation of the structural features of the microfluidic device in the entrance region.

Experimentally examine oscillatory and pulsatile flows in the entrance region of a microchannel at low Stokes numbers, $\alpha < 3$, where the entrance length is thought to be as large as steady flows. Measure the variation of entrance length with time, throughout the oscillation cycle, for a number of systematically varied flow conditions. Determine the maximum entrance length that occurs for each condition, and compare this to the results generated for steady flow in the same entrance region.

To meet these goals, Chapter 3 presents a detailed experimental characterization of the microfluidic device, and connecting fluidic components. The experimental techniques that are utilised in the present work are detailed and the procedures involved described. An uncertainty analysis is performed and the details of the numerical model documented. Chapter 4 examines steady flow in the entrance region of the channel and a provides a comprehensive comparison of experimental and numerical results. The method used to calculate the entrance length is then evaluated using this comparison. Chapter 5 extends the entrance region study to include oscillatory and pulsatile flows. Cycle varying entrance lengths are calculated and the maximum entrance length of each condition reported. Finally, in Chapter 6 conclusions and recommendations for future work are given.

Chapter 3

Experimental Methodology

In this chapter the experimental setup and details of the microfluidic device are presented. A description of the measurement technique is provided and the issues of its implementation in the current work is discussed. The experimental procedure is outlined, followed by a thorough error analysis of the experimental measurements. Finally, the approach taken in the numerical work is presented and its details documented.

3.1 Experimental Design

The design of a microfluidic device for experimentation can be a highly challenging task. The requirements for an experimental device are; that it can accurately generate the desired flow conditions, it is physically robust and can operate consistently to allow for repeat measurements, and it must allow for the desired measurement technique to be used. For the device to be physically realised, its fabrication must also be possible using existing micromachining techniques. The final constraint on the design is that it also needs to interface with a variety of macro-sized components, such as tubing and fittings, syringes and syringe pumps. These elements are discussed next as each element of the design is presented, starting with the most critical, the microfluidic chip.

3.1.1 Microchip Design

The microfluidic device in this study consisted of a large circular chamber connected to a series of microchannels integrated into a single device or 'chip'. The basic configuration of the chips was adapted from two designs of diaphragm micropumps, Morris & Forster (2000), and Sheen *et al.* (2008), and the harmonic change of volume of the chamber was used to transfer an oscillatory motion to the fluid within the device. Each device was formed from three different layers; a patterned silicon layer, a pyrex glass layer and a piezoelectric disc as shown in Figure 3.1. The circular piezoelectric disc was bonded to the back side of the silicon layer, centered above the circular chamber. The piezoceramic disc was used to deflect the silicon surface of the chamber, which is referred to as the diaphragm, under an applied voltage. Besides the chamber, the patterned silicon layer also contained a number of channels and the entire patterned surface was enclosed by the addition of the Pyrex glass layer, which allowed optical access into the device.

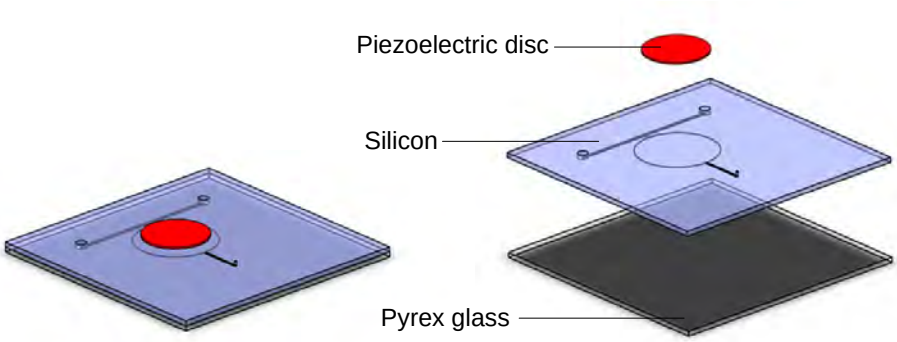

Figure 3.1: Microfluidic device.

The resultant fluidic structure formed between the silicon and pyrex glass layers was planar and its boundaries are shown in Figure 3.2. The pattern was designed in order to allow the study of velocity fields generated by oscillatory flows in variety of geometric arrangements commonly found in micro-devices. The current work is devoted to the entrance region, in this case where flow leaves

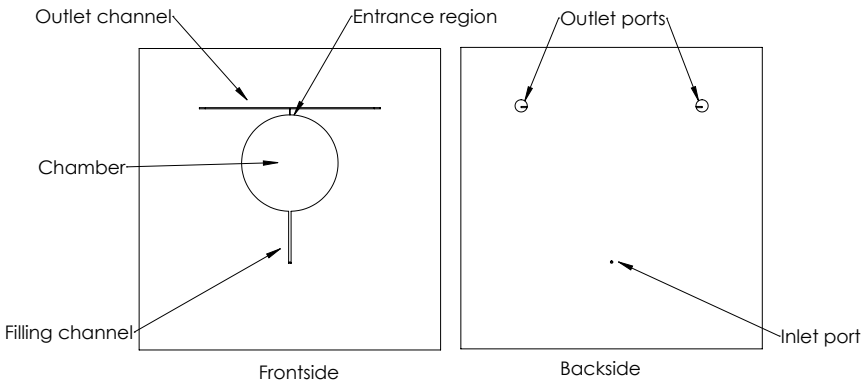

Figure 3.2: Planar pattern etched into the silicon layer.

the circular chamber and enters into a much smaller channel (see Figure 3.2). This region is described briefly here but discussed in more detail in Section 3.1.2.

The circular chamber was $8mm$ in diameter and connected to two channels, a $200\mu m$ wide filling channel located below the chamber and above by the main channel (as depicted in Figure 3.2), which was $50\mu m$ wide. The filling channel as the name suggests, was where the steady flow of fluid first entered into the device. Steady flow would continue from the filling channel to the chamber and then into the 'entrance region' of the main channel. At the end of main channel, it intersected with a third channel at a right angle to form a 'T' junction. This third channel was $100\mu m$ wide, and called the outlet channel. At the 'T' junction the flow would split into two and eventually flow out of the device at either end of the outlet channel.

Three openings or ports have been designed into the device and shown in Figure 3.2 from the top side of the silicon layer. Located $4mm$ below the chamber, a small inlet port $200\mu m$ in diameter was connected to the filling channel. The length of the filling channel was designed to allow sufficient space from the chamber for a valve to be placed on the back side of the silicon layer. The total volume of this port and connecting channel was designed to be small in comparison to the volume of the chamber and represents about 2 percent of the total chamber volume. The two remaining holes, $0.04in$ in diameter, were located at the two ends of outlet channel, $15mm$ apart, to allow sufficient space for connections to be attached at both ends.

The set of chips were fabricated using standard micromachining techniques by Micromotive Gmbh. The pattern in the silicon layer was etched with an inductively-coupled-plasma (ICP) etcher (ASE machine Surface Technology Systems). This method is a highly anisotropic process capable of etching high aspect ratio structures. The pattern consisting of the chamber, and channels was etched to a depth of approximately $50\mu m$ in a nominally $400\mu m$ thick silicon wafer. After this pattern was etched, the silicon layer was bonded anodically to a $300\mu m$ thick Pyrex glass layer. The circular holes for the inlet, and outlets were then etched from the back side of the silicon until they reached the patterned layer. Finally the chips were diced with a diamond tipped dicing saw into $25mm$ by $25mm$ chips. An example chip is shown in Figure 3.3.

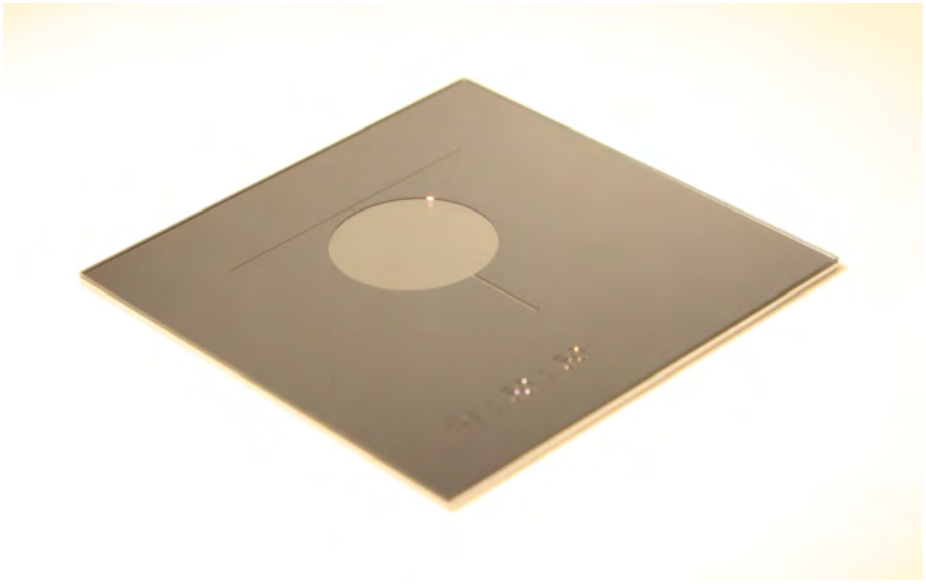

Figure 3.3: Image of the completed chip. Courtesy of Micromotive Gmbh.

To complete the devices a $6.4mm$ diameter circular piezoceramic disc (PSI-5A-4E Piezo Systems Inc) was bonded to the back of the silicon layer using conductive epoxy. Wires were soldered to the top of the PZT disc and to an area of the conductive epoxy using a solder/flux kit (Piezo Systems Inc).

3.1.2 The Entrance Region

The entrance region in the current work is shown in Figure 3.4, and was where flow entered the main channel from the much larger circular chamber. Due to the fabrication processes (etching and bonding of layers) this entry was planar, and the upper and lower surfaces were in common to both the chamber and channel. The channel was square in cross-section, nominally $50\mu m$ by $50\mu m$, and $500\mu m$ long, from chamber to the 'T' intersection. This channel length was relatively short for an entrance length study, however according to available correlations it should provide adequate length for development of low Re flows. The chamber was $8mm$ in diameter and since this dimension was much greater than the channel width (160 times larger), it was thought this entry would provide a good approximation of a planar entry from an infinite medium.

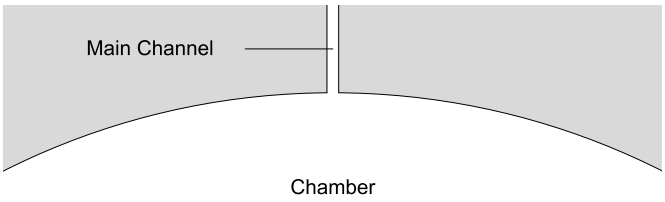

Figure 3.4: The entrance region.

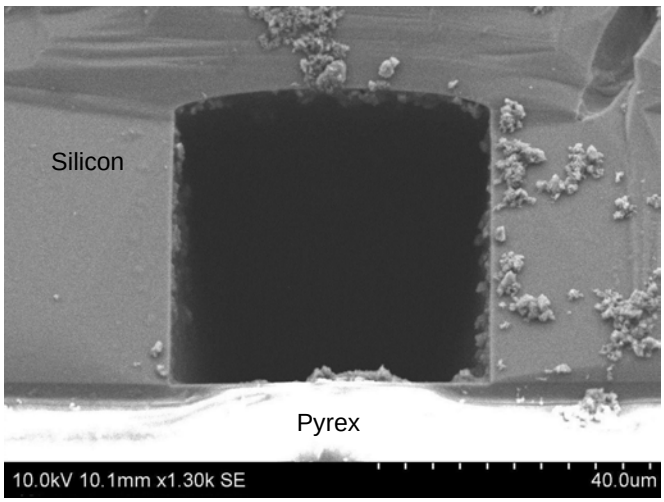

Figure 3.5: SEM image of the main channel cross section.

As discussed earlier in the literature review, the actual geometry resulting from the microfabrication processes often differs substantially from the intended design. The determination of the true geometry is critical for accurate reporting and interpretation of experimental results. After the completion of all experiments, the chip was cleaved into two pieces through the middle of the main channel to reveal the channel's cross-section. Figure 3.5 shows a Scanning Electron Microscope (SEM) image of a cross-section of the main channel. It can be seen that the etch process was able to create near-vertical walls, however it left the silicon surface of the channel (opposite the pyrex glass surface) slightly concave. The bonding process between the pyrex and silicon layers, as shown in Figure 3.5, was able to create angles in the corner very close to 90^o.

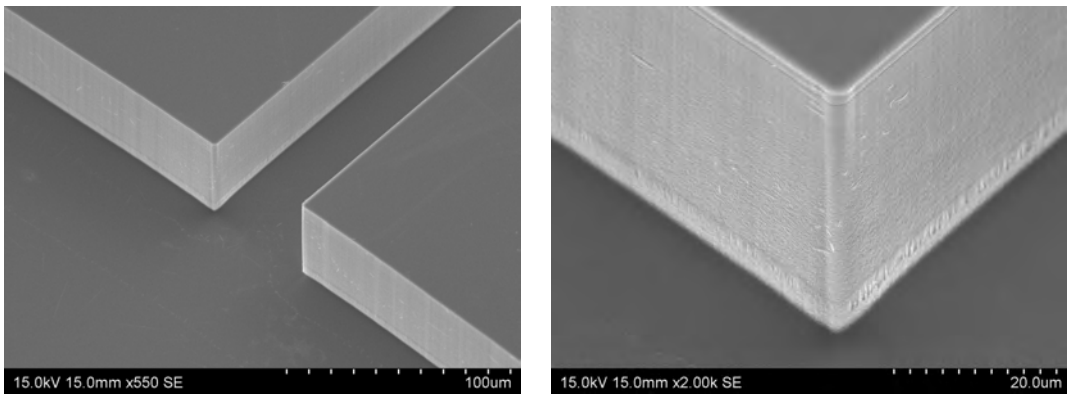

(a) (b)

Figure 3.6: SEM images of the entrance region. (a) Entrance region. (b) Close up of the entrance corner.

The part of the chip containing the entrance region of the main channel was placed in a solution of Hydrofluoric acid (HF) and the pyrex glass layer etched away in order to allow access to the pattern silicon surface. Two SEM images for the entrance region are shown in Figure 3.6. In Figure 3.6(a) the etched silicon walls are again highly vertical and the lower surface of the entrance region appears to be constant and smooth. In Figure 3.6(b), an image taken closer to the corner shows a slight rounding of the vertical edge at the entrance. From the images in this figure it would appear as though the fabricated geometry is exceedingly close to the idealised case.

To confirm the finding of the SEM images the surface in the entrance region

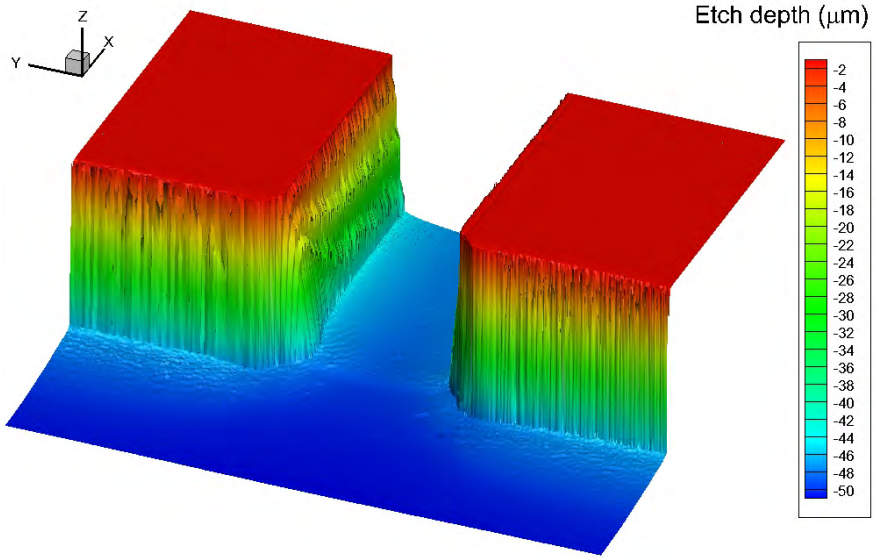

Figure 3.7: Optical profiler measurement of the surface depth.

was measured using an optical profilometer (Wyko model profilometer) and the result is shown in Figure 3.7. The profilometer was able to resolve the majority of the surface with high precision but was unable to obtain accurate measurements near the walls, within $\sim 5\mu m$. The nominal etch depth was $50mum$, however the lower surface, depicted as shades of blue in Figure 3.7, appears to vary around the entrance region. The curvature of the lower surface of the main channel seen in the SEM image can also be confirmed by the lighter shades of blue near the walls of the channel.

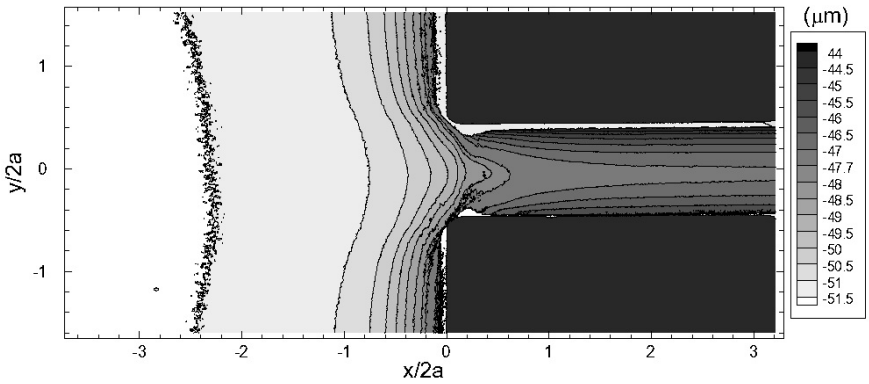

Figure 3.8: Two dimensional contour plot of the surface depth.

In Figure 3.8, the variation of the lower surface can more easily be distinguished. It can clearly be seen that away from the channel inlet, the depth of the lower surface of the chamber was very uniform, but interestingly in closer proximity to the channel entrance, the etch depth is reduced. The optical profiler measurements in Figure 3.8 reveal that the etched depth depends strongly on a locations proximity to the masked boundaries.

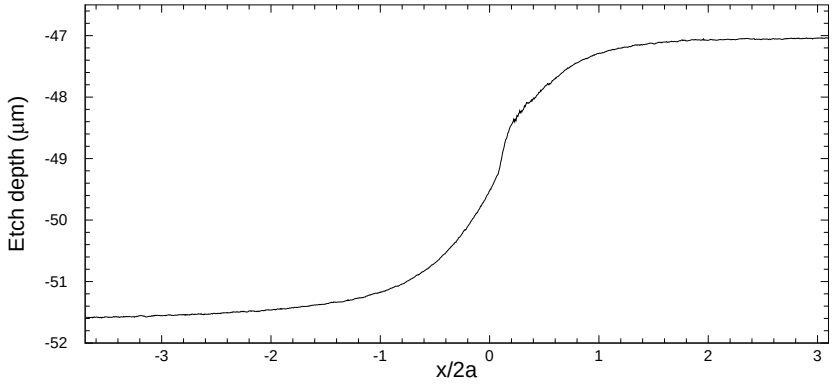

Figure 3.9: Etch depth along the centreline of the main channel.

Along the centreline of the channel, $y/2a = 0$, the surface depth has been extracted and plotted in Figure 3.9. The depth varies from $51.6\mu m$ in the chamber, far from the channel, to $47.1\mu m$ far inside the channel, which is a significant variation. The majority of this change happens within $\pm 2a$ of the entrance of the main channel and after one width, $2a$, into the channel, the depth varies only about 0.6% of its final value from then on.

Based on the SEM image and the optical profiler measurements, the best estimate of the channel dimensions at locations $> 2a$ away from the inlet are given in Figure 3.10. The width of the channel, $2a$, is equal to $51.2\mu m$, and the depth, $2b$, midway across the channel width is equal to $47.1\mu m$. The lower surface in Figure 3.10 varies smoothly from this value of $47.1\mu m$ to $43.9\mu m$ at the walls.

The curvature of the lower surface of the channel cross-section, as well as the change in etch depth that occurs around the boundaries, was found in both the SEM images and optical profilometer measurements. The changes found represent a significant deviation from the idealised geometry of a perfectly square channel, $50\mu m$ by $50\mu m$ and can have a marked influence on the development of flows. The identification of the features was critical in discerning the experimental results.

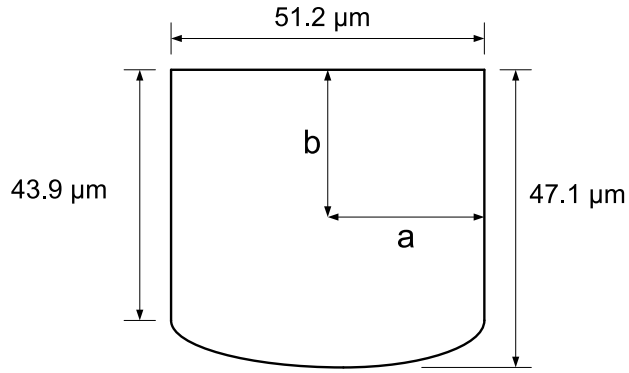

Figure 3.10: Main channel dimensions at distances $x/a > 4$ from the inlet.

3.1.3 Chip Interface Design

One of the key components for successful realisation of microdevices is their interfacing with other macro sized components. For the current set of chips a robust interconnect system was designed and is shown in Figure 3.11. The modular design allows for a reliable but non-permanent connection to external tubing and for a single interface to be used for all chips. A further benefit of the design is that it removes the need to use adhesives, which are a potential source of contamination in microfluidic devices.

Table 3.1: List of components in chip interface.

Item no.	**Name of Component**
1	OD 1/16*in* PEEK tubing
2	Upchurch M6 Nut and ferrule
3	Rotor valve
4	Silicon chip
5	Aluminium aligner
6	Glass slide
7	Aluminium top plate
8	Aluminium lower plate

An exploded view of the components is shown in Figure 3.11(a) and a list of all components given in Table 3.1. The interface consists of a top and bot-

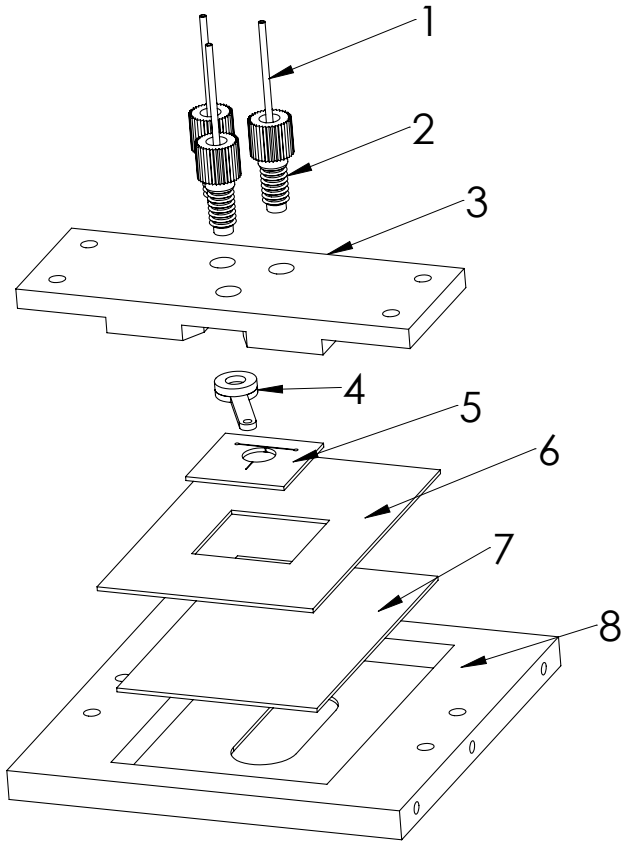

(a)

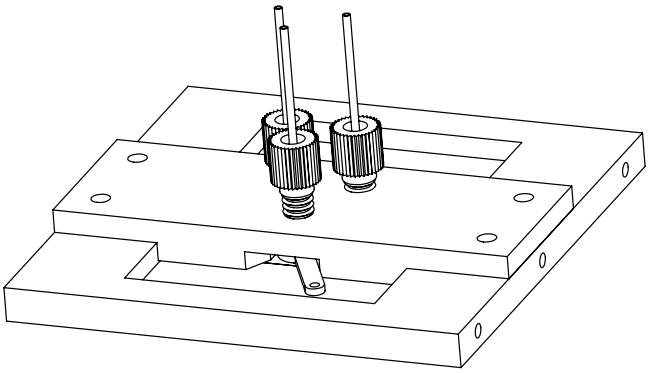

(b)

Figure 3.11: (a) Exploded view of chip interface. Identities of components 1-8 given in Table 3.1. (b) Assembled chip interface.

tom plate fabricated out of aluminium. Three tapped holes in the top plate allow the compression fitting of the standard $16in$ OD tubing to the chip with nuts/ferrules from Upchurch (Upchurch Scientific P-225/P-200N). The ferrules seal flush against the chip surface for the two outlet holes. For the filling port, the ferrule connects to a rotor valve on the chip surface, which provides a means of opening/closing the filling port without adding any additional volume to the oscillating chamber. The design of the rotor valve is discussed in the next section. The diaphragm region of the chip must be undisturbed so that it is free to deflect. Therefore no other contact from the chip holder to the top surface of the chip is made and it is the compression of the ferrules/nuts, which holds the chip in place in the vertical direction.

The bottom plate provides optical access into the device through a milled $16mm$ wide slot. A large $1mm$ thick glass slide $76mm$ by $51mm$ is inserted into the bottom plate to strengthen and protect the chips from the forces required in the compression seal of the ferrules. The chip is positioned on the surface of the glass slide by means of a $1mm$ thick aluminium locator. The locator aligns the chips ports with the tubing connections and also prevents stray light passing through the interface. The entire assembly is closed through four screws that connect the top and bottom plates together.

3.1.4 Rotor Valve Design

The rotor valve for the filling port was fabricated based on the design of Shimura *et al.* (2007). The valve connected to an Upchurch nut and ferrule on one side, and to opening of the filling port of the chip on the other side. Figure 3.12 shows a cross-sectional view of the valve arrangement. The location of the centre of the valve is offset a distance of $2mm$ from the filling port. A $1mm$ wide slot milled $0.5mm$ deep in the bottom of the rotor surface connected the centre hole to the filling port. A schematic drawing of the valve with its lever is presented in Figure 3.13. The valve and lever were fabricated in Teflon and aluminium respectively.

A key on the rotor was formed by milling away two sides of the rotor at an angle of 30^o to the slot. An aluminium lever with a matching keyhole was fabricated with a $17mm$ long handle. The rotor valve and lever fit into a slot cut out of the aluminium top plate. When the rotor is turned anti-clockwise

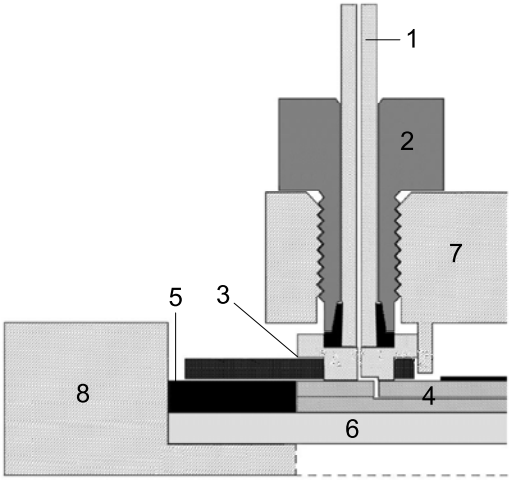

Figure 3.12: Cross section of the rotor valve assembly and interface. Adapted from Shimura *et al.* (2007). Identities of components 1-8 given in Table 3.1.

and positioned with the lever in line with the edge of the cut out section, the slot in the rotor is aligned with the filling port on the chip. The cut out section allows the lever to rotate an angle of 60^o. Misalignment of the slot and filling port occurs at a clockwise turn of about 17.5^o from this position and a $1mm$ seal in all directions is achieved at the maximum turn of 60^o.

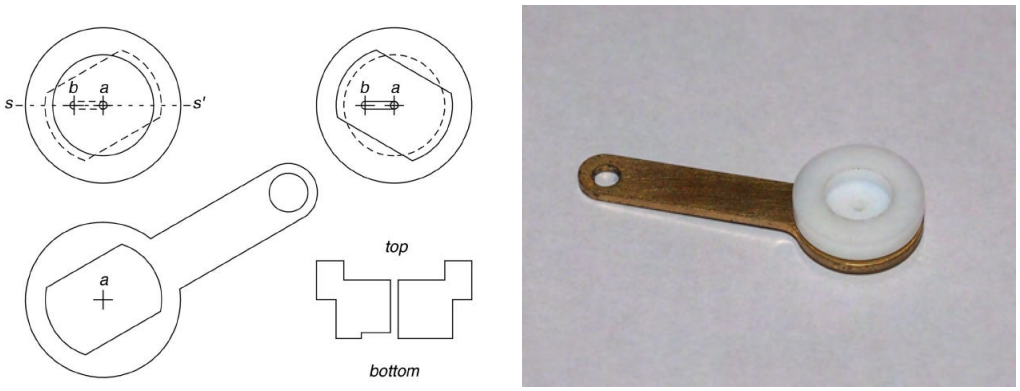

(a) (b)

Figure 3.13: Rotor valve. (a) Schematic diagram of the rotor valve and lever. Taken from Shimura *et al.* (2007). (b) Photo of the fabricated rotor valve.

3.1.5 Complete Flow Arrangement

A schematic diagram of the experimental setup can be seen in Figure 3.14. Steady flow through the silicon chip was generated by a syringe pump (Harvard Apparatus PHD 2000) and syringe (SGE $5ml$ gastight). All components of the fluidic system were connected to $1/16in$ OD, $0.04in$ ID PEEK tubing. The tubing and all fittings used in the setup were purchased from Upchurch Scientific. An inline $10\mu m$ frit filter (A-425) was installed just after the syringe to prevent clogging of the microchannel. The filter frit was small enough to protect the microchannels from debris but large enough to allow the fluorescent particles for the PIV measurements through. A junction was added to the fluid line between the syringe and device, with a valve connected to each line. The junction allowed for any air that became introduced into the line during the interchange of the syringes to be removed before it could flow into the device.

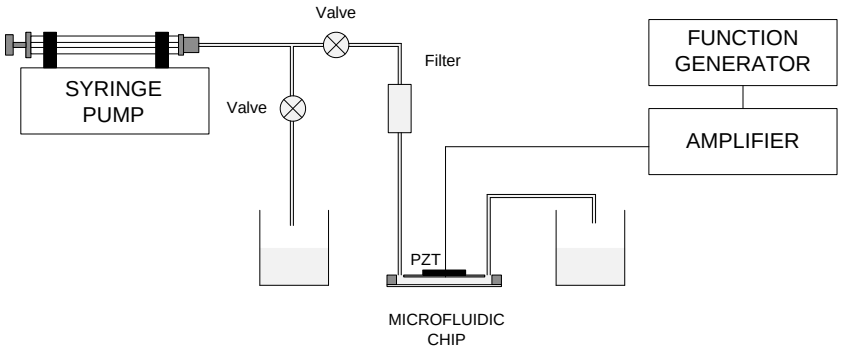

Figure 3.14: Schematic diagram of the complete flow arrangement.

The oscillatory component of the flow was generated by harmonic motion change in volume of the chamber due to the deflection of the diaphragm. The piezoceramic patch glued to the backside of the diaphragm converted a supplied voltage signal into a mechanical deflection. A sinusoidal signal from a function generator (INSTEK GFG-8216A) was amplified by a linear amplifier (EPA-007-012, Piezo Systems, Inc) and connected to the piezoelectric patch. The signal generator and amplifier allowed systematic variation of both the frequency and amplitude of actuation. The frequency limit of the amplifier was $1.5kHz$, which provided an upper limit to the Stokes number of 2.45 for the given geometric

and fluid conditions. The amplifier also had a voltage limit, which was $180V$ peak-to-peak. Finally, a TTL signal from the function generator served as the reference signal for the micro-PIV measurements.

3.2 Micro-Particle Velocimetry

The technique used exclusively in the current work to measure planar velocity fields was Particle Image Velocimetry (PIV). In PIV small tracer particles are added to the flow and the fluid velocity is inferred from the motion of the tracer particles (Westerweel (1997)). The positions of the tracer particles at two instances in time, separated by the time interval, Δt, are captured optically by a camera. The local velocity u, can then be estimated from

$$u = \frac{\Delta x}{\Delta t} \tag{3.1}$$

where Δx is the displacement of a tracer over the time interval Δt. The measurement of this velocity is an accurate representation of the fluid velocity provided; the particles are ideal tracers, and the spatial resolution and time interval of the recording is small compared to the spatial and temporal scales of the flow.

High concentrations of particles are used in PIV and the average displacement of local groups of particles are determined as opposed to tracking individual particles. The recorded images are divided into smaller regions known as 'interrogation windows' and the displacement of the group of particles within the interrogation windows are evaluated in a statistical manner (auto- and cross-correlation).

The modern macroscale PIV setup incorporates a fast interline transfer CCD camera to allow for the particle images to be captured on two separate frames with a time interval between frames shorter than a microsecond. A laser source with a duration short enough to 'freeze' the particles motion is pulsed twice, (once in each frame) with a time delay between pulses of Δt. The laser is formed into a thin light sheet and the light scattered from the particles within the sheet recorded by the CCD camera through a high quality lens.

The PIV technique was extended to microscale flows by Santiago *et al.* (1998) and Meinhart *et al.* (1999). They used epifluorescent microscopy with submicron particles to achieve spatial resolutions of less than a micron. Lack of optical ac-

cess into micro devices combined with diffraction effects means that light sheet illumination is not practical at this scale (Raffel *et al.* (1998)). Instead the entire flow volume is illuminated and the thickness of the measurement domain is defined by the optical components of the system. The other main difference to the traditional PIV method is the evaluation algorithms employed. MicroPIV evaluations generally use ensemble correlation based algorithms, which produce an averaged result from an ensemble of image pairs. These algorithms were developed to minimise the effects of Brownian motion and to overcome the low seeding densities (Wereley & Meinhart (2010)) encountered in microscale experiments.

3.2.1 System Configuration

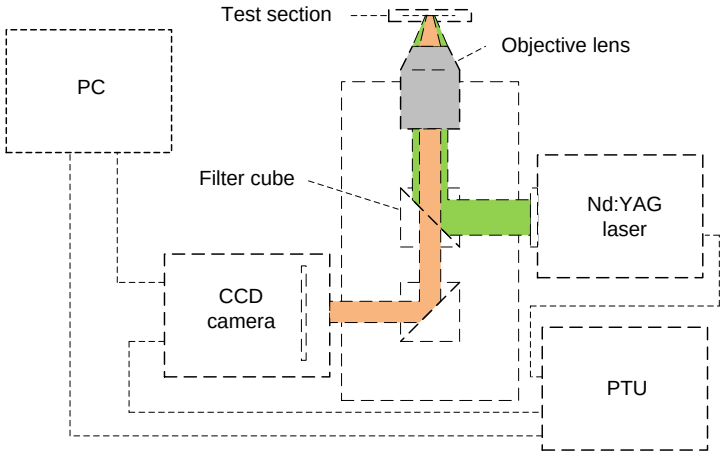

Figure 3.15: Components of the microPIV setup.

The microPIV setup used in the current work was a standard commercial setup supplied by Lavision Gmbh and is depicted in Figure 3.15. The illumination was provided by a pulsed Nd:YAG laser (Litron Nano S30-15), that was connected to an inverted microscope (Nikon Eclipse Ti) through a fibre optic link. The laser pulses were directed through an epi-fluorescent filter cube and then relayed on to the test section through a 40x objective lens. Fluorescent particles (Duke

Scientific) seeded in the flow absorbed the green laser light and emitted light back at a higher wavelength, red. The emitted light was imaged through the objective lens and passed back through the filter cube on to a CCD camera (PCO Sensicam QE). The timing of the camera frames and laser pulses were synchronised by a Programmable Timing Unit (PTU), which was controlled through Lavision's software package DaVis. The properties of each of the major components is given in Table 3.2.

Table 3.2: Properties of the components used in the microPIV setup.

Property	**Value**
Seeding	
Diameter	$0.5\mu m$
Density	$1.06kg/m^3$
Ex/Em maxima	$542/612nm$
Optics	
Magnitication	40x
wd	$2.7mm$
N.A.	0.6
Recording	
pixels	1376 x 1040
pixel size	$6.45\mu m$
Field of view	$222\mu m$ x $168\mu m$
Measurement depth, $2\delta_{corr}$	$6.8\mu m$
Particle Image Diameter	$55\mu m$ (8.5 pixels)
Illumination	
Source	Nd:YAG
Energy	$40mJ$

The definition of out of plane measurement thickness for microPIV experiments was first introduced in Meinhart *et al.* (2000) and later named the depth of correlation. It is defined as the depth in which particles significantly contribute to the signal peak in the particle image correlation function. Olsen & Adrian (2000) derived an equation for the depth of correlation in microPIV as:

$$\delta_{corr} = \left[\frac{(1-\sqrt{\epsilon})}{\epsilon}\frac{n_0^2 dp^2}{4NA^2} + \left(\frac{5.95(M+1)\lambda^2 n_0^4}{16M^2NA^4}\right)\right]^{1/2} \tag{3.2}$$

where d_p is the particle diameter, λ the emitted wavelength, M the image magnification, n_0 is the refractive index of the lens immersion liquid, NA the numerical apperature of the lens, where $NA = n_0/2f^{\#}$ has been used, with $f^{\#}$ being the f number of the lens. Here ϵ is a threshold value set equal to 0.01. The measurement thickness was then determined as $2\delta_{corr}$ and this represents the commonly accepted expression for the depth of correlation. It is important to note however that the correct quantification of the depth of correlation is still an avenue of current research Lindken *et al.* (2009). For the given experimental setup the measurement thickness, $2\delta_{corr}$ is $6.8\mu m$. This thickness was a considerably large portion, about 14% of the $\sim 50\mu m$ deep channel. Therefore the effect of this depth on the measurement accuracy must be considered and is explored in Section 3.2.3. The only way this depth could be significantly reduced is to choose a different objective lens with a higher NA value, however this was not possible as a large working distance of at least $1.5mm$ was required due to the physical setup of the device.

Another important property of the setup is the particle image diameter, d_e, recorded by the camera. It is a product of the particles geometric image and the particles diffraction limited image. Combing these effects Olsen & Adrian (2000) showed the particle image diameter is given by:

$$d_e = \left[M^2 d_p^2 + 5.95 \left(M+1\right)^2 \lambda^2 \left(\frac{n_0}{2NA}\right)^2 \right]^{1/2} \tag{3.3}$$

The particle image diameter for the current setup is approximately $55\mu m$ or 8.5 pixels.

3.2.2 Tracer Particles

In microPIV measurements the size of particles in terms of their tracing ability are generally not a large concern due to the large surface to volume ratios at this scale (Raffel *et al.* (1998)). Smaller particles follow the flow more faithfully and evaluation methods also benefit as the measurement error has been shown to be proportional to the particle image size (Westerweel (2000)). However larger particles are preferred to minimise the effects of Brownian motion and increase particle visibility. Therefore the smallest particle size which satisfies the optical

constraints is normally chosen. As a general rule, it is suggested that particle diameters be smaller than the smallest channel dimension by two of orders magnitude in order to avoid any size effects (Lindken *et al.* (2009)). The smallest dimension in the current micro devices is $\sim 50\mu m$ and therefore according to this criterion the particles selected were $0.5\mu m$.

In the desired experiments the high accelerations involved pose a potential challenge for tracers particles. Assuming stokes drag, the error due to slip can be given by (Meinhart & Zhang (2000)):

$$|u - v| = \frac{\rho_p d_p^2 |\dot{v}|}{18\rho_f \nu_f} \tag{3.4}$$

where u is the fluid velocity, v is the velocity of the tracer particle, ρ_p and d_p are the tracer particles density and diameter, respectively, $\dot{v}$ is the time derivative of the particle velocity, and ρ_f and ν_f are the density and kinematic viscosity of the fluid, respectively. For a point in a flow field with a sinusoidal dependence in time, $u = u_a sin(\omega t)$, the acceleration of a particle can be estimated by $|\dot{v}| = u_a \omega cos(\omega t)$. The velocity and acceleration are 90^o out of phase and therefore the maximum absolute error occurs at the minimum velocity. As an estimate of the maximum error, the slip velocity divided by the local amplitude velocity, u_a, can be given as

$$\frac{|u - v|}{u_a} = \frac{\rho_p d_p^2 \omega}{18\rho_f \nu_f} \tag{3.5}$$

which besides the fluid and particle properties, is only a function of the angular frequency, ω. For the particle size selected of $0.5\mu m$, this error is a maximum for the highest frequency, $f = 1.5kHz$, which gives an error of 0.014% u_a. In other words, the error due to acceleration when measuring a velocity even as low as 100 times smaller than the maximum velocity that occurs at that point, is still only about 1.4% of the actual velocity.

In microchannels, large velocity gradients of the order of $100,000 s^{-1}$ are often encountered. Velocity gradients can cause a particles motion to have a transverse component known as the Saffman effect when inertia effects are also present. The Saffman effect plays an important role in the migration of particle's in shear flow, however the transverse component is much weaker than the rectilinear compo-

nents (Michaelides (1997)). Provided the error due to slip is small, the error due to shear induced flow is necessary small and is therefore neglected in the current work.

Particles suspended in a fluid with sub-micron diameters experience a random thermal component to their movement, known as Brownian motion. Santiago *et al.* (1998)) performed a first order analysis of the relative error due to Brownian motion and showed that the relative error is given by

$$\epsilon_B = \frac{1}{u}\sqrt{\frac{2K}{\Delta t}} \tag{3.6}$$

Here the diffusion coefficient K is as derived by Einstein:

$$K = \frac{\kappa T}{3\pi\mu d_p} \tag{3.7}$$

where κ is Boltzmann's constant, T is the temperature in Kelvin and μ is the dynamic viscosity of the fluid. From 3.6 the relative error caused by Brownian motion decreases with increasing velocity, but increases with reduction of Δt. Generally the relationship chosen between u and Δt in experiments is a linear one and for faster flows the effects of Brownian motion become less and less important. For the slowest flow measured, the average velocity was $0.022m/s$ and $\Delta t = 59\mu s$, which gives an error from Equation 3.6 as 0.4%. If the effects of Brownian motion are modelled as random, the uncertainty decreases as $1/\sqrt{N}$, where N is the total number of the particles in the average and this error is further reduced with more particles in the evaluation.

3.2.3 MicroPIV Optimisation

So far only the physical components, which make up the PIV arrangement have been discussed, however there exists a number of parameters in PIV experiments, which need to be selected in order to make accurate measurements. These parameters are the concentration of tracer particles in the working fluid, the separation time between laser pulses, the number of image pairs recorded and the manner in which the images are processed to determine the velocity fields.

Particle Concentration - Typical particle/fluid volume percentages in the

range of 0.1% to 0.01% are used in microPIV experiments. A high particle concentration leads to an increase in noise within captured images and an increased in particle/particle interactions. A further problem is increased particle agglomeration and channel fouling. Correlation ensemble averaging, which was used exclusively in this work removes the dependence on concentration for increasing the effective particle image density. Therefore a low seeding concentration of approximately 0.01% by volume was used for all experiments. This provided an average of at least one particle per interrogation volume for all experiments performed.

Laser Pulse Separation Time - The laser pulse separation time, Δt, is an important parameter in a PIV experiment because it controls the particle image displacement. In traditional PIV measurements, Δt has strong impacts on the random error, the acceleration error, the error due to velocity gradients (Boillot & Prasad (1996)) and in microPIV also effects the error due to Brownian motion (see Equation 3.6). It is also the most easily varied parameter in a PIV experiment. A longer laser pulse separation time increases a particles displacement, Δx, and thus minimises the relative error component. A long Δt however, also increases the acceleration error caused by determining the Eulerian velocity field from a particles Lagrangian motion (Boillot & Prasad (1996)). Similarly a long Δt increases the error due to velocity gradients by increasing the relative motion between particles within an interrogation window (Keane & Adrian (1992) and Westerweel (2008)). Therefore an optimum laser pulse separation time, which minimises the total error from all sources should be selected.

A range of values for Δt (or equivalently particle displacements, Δx) were trialled and provided particles displacements were greater than a pixel, no discernable difference could be found between the results in terms of velocity profiles or entrance lengths. It was concluded that as the current PIV setup was largely insensitive to the choice of laser pulse separation time and that a large Δt should be chosen to ensure minimisation of the relative error. The final condition placed on the value of the laser pulse separation time, was that it must allow the particles moving at the fully developed centreline velocity a displacement of 16 pixels. Therefore all displacements with the measurement domain were in the range 0-16 pixels, and typically the average displacement was ~ 8 pixels. The only time this condition was violated was in the oscillatory cases, where a second condition was

imposed.

In the oscillatory cases when the flow changes its direction, the flow velocities are low and the acceleration is large. Therefore Δt must also be kept short to prevent error from temporal changes of the velocity field. The second condition imposed on the laser pulse separation time was that it could not be greater than 2% of the total oscillation cycle. However this condition was imposed on only a very few number of the total cases, at phase angles where the flow was changing direction and the average velocities in the measurement plane were very close to zero.

Number of Image Pairs - With all other PIV parameters selected the final parameter to be optimised is the number of image pairs required in the ensemble. Generally more image pairs in the ensemble gives a higher level of accuracy, however there is also a practical limit in terms of the acquisition and processing times and computer memory. For the experimental conditions described above, it was felt that this limit was 200 images pairs which was recorded for all experimental cases.

The convergence of the ensemble averaging process in terms of the number of image pairs is presented in Figure 3.16, following Poelma *et al.* (2008). In this plot the average of the absolute deviation of all vectors in the measurement domain was calculated, and the differences between results obtained using i and $i-1$ image pairs are shown. The rate of convergence depends on the seeding conditions, clarity of the channel in terms of fouling and the stability of the flow. As an indication of this variability four experimental cases were examined for a total of 200 image pairs. All four cases had approximately the same average pixel displacement equal to 8 pixels. In Figure 3.16 the deviation rapidly decreases for the first 50 image pairs and reached subpixel values within 10 images pairs for 3 out the four cases (with the exception of Exp 2). By 50 images pairs all cases have reached an average deviation of about 0.2 pixels, and this value decreases to under 0.1 pixels by 200 image pairs.

Image Evaluation - The acquired images were processed using the PIV software package Davis. Images from microPIV experiments are generally pre-processed before the vector calculation is performed to help remove background illumination non-uniformities and single pixel noise. Pre-processing of images also effects the depth of correlation and can be used to minimise the effects of velocity gradients

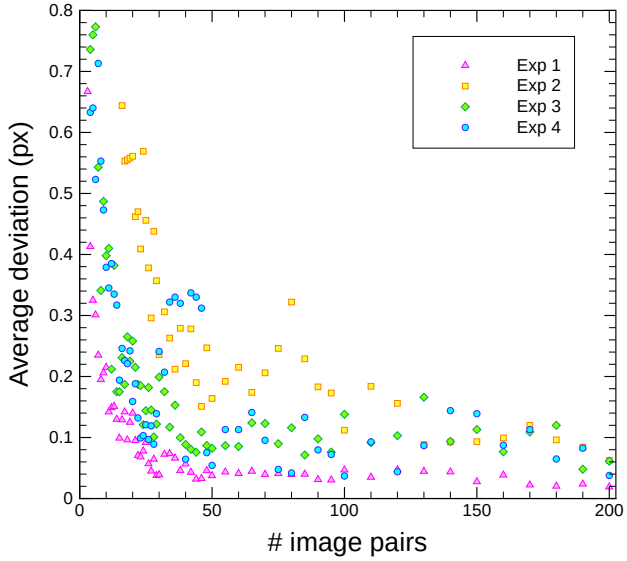

Figure 3.16: Convergence of velocity data against number of image pairs.

across the measurement volume. Bourdon *et al.* (2004) demonstrated the use of a power filter in combination with background subtraction to increase or reduce the depth of correlation by a known amount. Nguyen *et al.* (2010) overlapped images based on maximal intensity values to minimise the effects of out of focus particles. Due to the large value of depth of correlation calculated for the current setup an optimum method of pre-processing the images to reduce the depth of correlation was desired.

The two methods cited above were compared for fully developed laminar flow conditions, along with the case of no image pre-processing. No significant change in the results was found for both methods over no pre-processing. The same conclusion was reached by Rossi *et al.* (2010) for small particles sizes, $d_p \leq 1\mu m$, that pre-processing had a negligible effect on the depth of correlation. Therefore the pre-processing method selected was chosen solely to help with background noise, and minimise the effects of large groups of agglomerated particles, which sometimes passed through the channel. The method selected was built into the Davis software, called 'sliding background removal', which essentially acts as a high pass filter (Davis Manual), removing unwanted background noise from the image while allowing the particle image information through.

Each phase consisting of a set of image pairs was processed as a set to determine phase averaged results. The vector calculation was performed using an iterative cross-correlation method with decreasing window size. The cross-correlation method employed averages the correlation data rather than the velocity fields to determine the final phase averaged velocity vector. This method known as ensemble correlation and was first proposed by Meinhart *et al.* (2000). It results in a much higher signal-to-noise ratio for stationary or periodic flows.

The initial passes used a second order correlation and the final pass used a standard forward difference scheme. The initial passes were used to provide a good estimate of the flow field and window shift for the final pass. An initial window size of 64 x 64 pixels and final window size of 32 x 32 was employed. A window overlap of 50% was used in all passes.

The final vector field was processed by a validation algorithm to detect spurious vectors. The algorithm is based on the local median filter proposed by Westerweel (1994), which compares vectors to the median value of their surrounding vectors. Vectors outside of a set number of standard deviations from the median value were rejected. The vectors rejected by the validation procedure were replaced by the local average of adjacent vectors, which have been already been accepted.

3.2.4 A Final Note

In Adrian (2005), Adrian reviewed PIV's development over the past twenty years and commented on desirable future developments. Most crucial for the current work Adrian stated:

'The results of PIV experiments should be held to increasingly rigorous standards.'

In particular it was stated that the accuracy and reproducibility of the velocity measurements should be routinely demonstrated. Every attempt has been made in the current PIV experiments to comply with the suggestions made by Adrian. Section 3.2.3 attempted to provide both theoretical and experimental justification for the MicroPIV parameters selected. The laminar nature of the flow on the microscale has allowed the comparison of results to analytical solutions. This has been done wherever possible. Measurements in almost all cases were the

result of a number of experiments in order to increase accuracy and demonstrate reproducibility. Furthermore, a detailed uncertainty analysis of all measurements has also been performed and is discussed in section 3.4.1.

3.3 Experimental Method

3.3.1 Procedures

The experimental method employed in the current work can be broken down into a number of procedures or steps, which have been outlined in Figure 3.17. Once the chip and interface system were assembled together, the steps in the flowchart were followed from start to finish for each set of measurements made, however the step 7, the determination of amplitude and phase of oscillation, was required only for the oscillatory cases. The steady flow measurements were made in sets that consisted of a number of different flow rates. The oscillatory measurements were also made in sets but consisted of measurements made located at a different phase angles equally spaced, every 15^o throughout the cycle, under the same oscillatory flow conditions. All sets of measurements were acquired and processed in essentially the same manner represented by Figure 3.17. Since every step in the process was necessary for successful determination of the flow and entrance lengths, each step is described in some detail next.

Device filling - The performance of the diaphragm was heavily dependent on the amount of air in the chamber. Consistent performance was achieved by filling the device so that no visible signs of air bubbles could be found. The 5 mL gas tight syringe (SGE) and syringe pump (Harvard Apparatus PHD 2000) were used to fill the device completely with liquid. In order to achieve this, the chip and fluid lines were first primed with Isopropanol and the chip was visually inspected for bubbles under the microscope. Once all bubbles had been removed, the device was flushed with de-ionised water and visually inspected a second time. This process was made possible by the junction placed in the fluid line upstream of the chip entry (discussed in Section 3.1.5 and shown in Figure 3.14), which allowed for the syringe to be interchanged numerous times without any air being introduced into the line reaching the chip. Finally the working solution consisting of de-ionised water and fluorescent particles was introduced into the device.

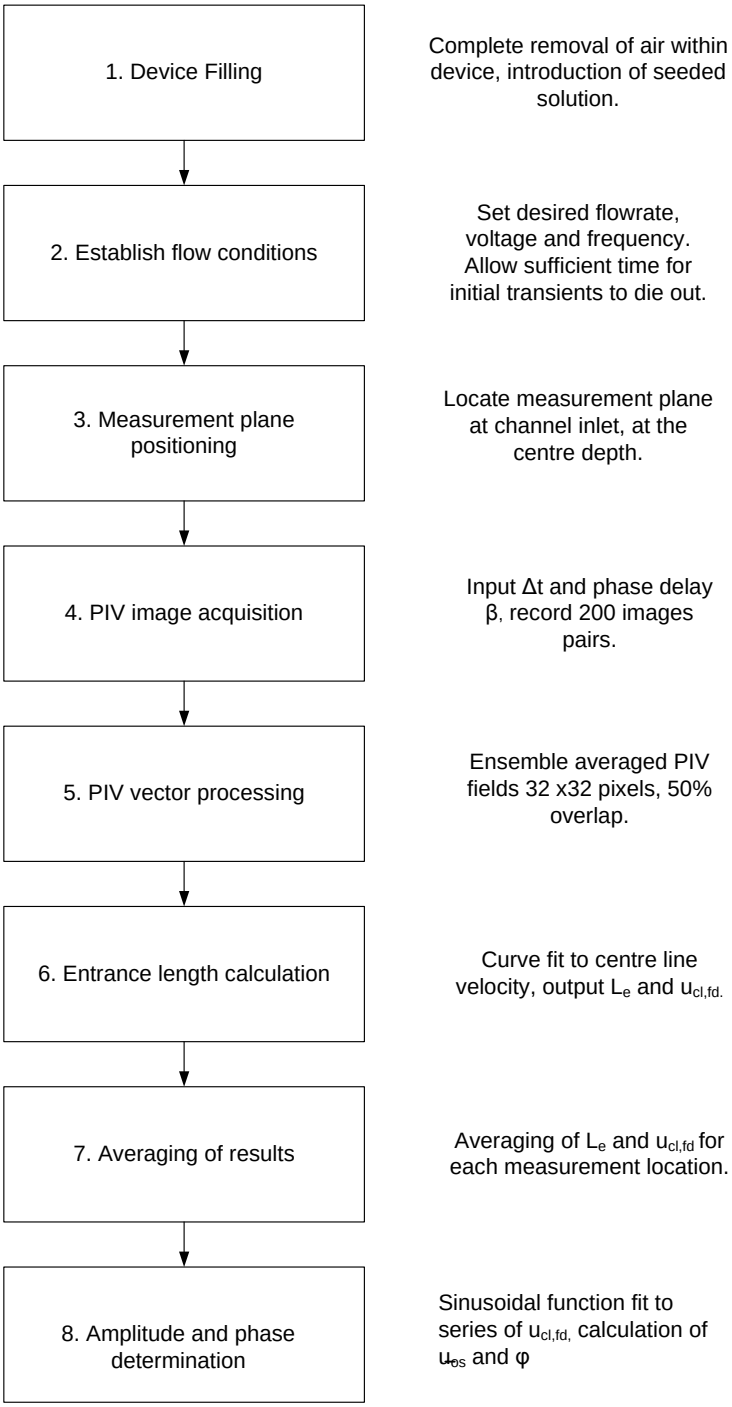

Figure 3.17: Flowchart of steps in the experimental procedure.

The amount of dissolved gases present in the working was not directly controlled. The degasification of solutions is known to be a complex process that is extremely difficult to control and quantify Morris & Forster (2003). Paramount to the current experiments was the ability to generate reproducible and consistent flow conditions. The degasification of a fluid creates a transient fluid state that is not in equilibrium with the surroundings. Therefore rather than varying the level of dissolved gases, the working fluid was kept constant by keeping it close to atmospheric conditions throughout the experimental work.

Establish flow conditions - The flow conditions were controlled by the flowrate set via the syringe pump and the voltage and frequency supplied by signal generator and amplifier. For steady flow conditions, the volumetric flowrate is set and the average velocity in the channel known. For the oscillatory and pulsatile experiments however, the voltage and frequency are set but the amplitude of oscillation of the flow per unit volt supplied was initially unknown. The relationship between the electrical signal delivered to the piezoelectric disc and the resultant velocity field was determined from preliminary PIV measurements, and described next in Section 3.3.2.

Once the conditions were applied to the syringe pump and/or the signal generator, a sufficient length of time had to be waited for all start up transients to die out before the commencement of measurements. Transient times in microdevices can be surprisingly long, of the order of mintues or longer (Stone *et al.* (2004)), due to the compliance of the tubing and small air bubbles, which may get trapped in the fluidic lines. The time required for both steady and oscillatory flow to reach a steady state was determined by a trial and error process with the micro-PIV measurements. The time required was in the range 2-10 minutes, depending on the initial and final conditions. For the purely oscillatory cases, where there was no steady flow component, seeded particles still needed to be introduced via steady flow from the syringe pump. Once a satisfactory concentration of particles was achieved, and the pump was stopped and the rotor valve closed. The flow was then allowed to settle before measurements were made. This process would needed to be repeated during experiments as the concentration of particles in the entrance region under oscillatory conditions would gradually be reduced over time.

Measurement plane positioning - The last part of the procedure required before

acquisition of images, was to locate the region on interest of the device within the camera image. The centre-plane of the channel (z-location) was determined by focusing on particles that had adhered to the upper and lower surfaces of the channel and then positioning the lens to a location halfway in-between. This was done in a similar manner to Rossi *et al.* (2010), however in this case the focal point was determined by eye and thus introduced an uncertainty into the measurement location. The location of the chip relative to the camera image was determined from an image acquired while focused on the lower surface of the chip. Here the silicon surface is bonded to the pyrex glass layer and the boundaries of the channel can be imaged with high clarity. The entry (x-location) and centreline (y-location), halfway between the two channel walls, was accurately identified from this image. Accurate determination of this positioning was required for the calculation of the entrance lengths.

PIV image acquisition - Two hundred images pairs were acquired for each desired flow condition. This required the specification of the laser pulse separation, Δt and the phase angle delay, β, relative to the reference signal for the oscillatory cases. As pointed out in the first step, the performance of the diaphragm for a given voltage signal was intially unknown and therefore so was the required phase angle delay, β. See Section 3.3.2 for the details of its determination. The laser pulse separation for all cases was set according to the criteria already discussed in Section 3.2.3.

PIV vector processing - The details of the velocity vector calculation was given in Section 3.2.3.

Entrance length calculation - the method employed here to calculate the entrance lengths incorporated a curve fit to the centreline velocities in a manner very similar to Lee *et al.* (2008). Equation 2.9,

$$u = C_1 - C_2 e^{-C_3 x} \tag{3.8}$$

was fit to the centreline velocities, which were extracted from the entrance region of the channel based on the determined position of the channel relative to the image. For all cases only a single field of view was used, and thus it was required that the flow developed within a length of $222\mu m$. The row of vectors corresponding to the y-location closest to the centreline was extracted, and due to

the resolution of the PIV measurements was within $+/-1.3\mu m$ of the specified centreline. The starting point for the extracted row of velocities was the first velocity that occurred after the calculated entrance to the channel. For each flow field measured, this process was performed with the entrance length, L_e, and the fully developed centreline velocity, $u_{cl,fd}$, extracted from the curve fit.

Averaging of Results - in order to increase confidence in the experimental results, each measurement (each Re for the steady cases, and phase angle, θ, for the oscillatory cases) was repeated on five separate occasions. The entrance length, and fully developed centreline velocity for each case were averaged and the standard deviation recorded.

Amplitude and phase determination - for the oscillatory flow cases, it was desired to represent each measurement in terms of the average flows properties, $\bar{u}_{os}$, the amplitude of oscillation, and θ, the phase angle. As the cross-section averaged flow rate is not measured, it's calculation is most easily derived from looking at a single point within the flow field over part of the oscillation cycle. The most reliable measurement point was the centreline velocity, $u_{cl,fd}$, determined from the curve fit and averaging procedures.

For fully developed oscillatory flow each point, i, within the cross-section, varies sinusoidally in time and can be described by,

$$u_i = u_{os,i} sin(\theta + \phi_i) \tag{3.9}$$

where ϕ_i is the relative phase between a local point and the cross section average velocity. Measurement of oscillatory flow conditions were made in sets of n different phase angles, and after performing step 7, as shown above in Figure 3.17,resulted in n average values of the fully developed centreline velocity, $u_{cl,fd}$. These measurements were sampled equally in time relative to the sinusoidal reference signal. A sinusoid was fit to the n values of $u_{cl,fd}$ and the value of uos, i and $(\theta + \phi_i)$ determined. The relationship between an individual point, $u_{os,i}$ and ϕ_i, and the desired properties of the average flow, $\bar{u}_{os}$ and θ, can easily be calculated from the analytical solution to fully developed oscillatory flow. In this case the analytical solution of Drake (1965) was used for this purpose.

3.3.2 Timing and Diaphragm Performance

As pointed out in the previous section the performance of the diaphragm for a set voltage signal was initially unknown. It was desired to determine the amplitude of the average flow, $\bar{u}_{os}$ for a given voltage amplitude and frequency. It was also desired to measure velocities at specific phase angles, θ, of the average flow cycle. Therefore knowledge of the relative timing between the flowfields and electric signal was required. The relative timing must account for all time delays present in the setup, such as with the triggering and firing of the lasers. This relationship was determined by PIV measurements and preliminary experiments were made following the steps outlined in Figure 3.17 and an example shown in Figure 3.18.

In these experiments a sinusoidal electric signal,

$$V = V_{os} sin(\omega t) \tag{3.10}$$

of known voltage and frequency was applied to the piezoelectric disc. Here V_{os} is the amplitude of the signal in volts, ω is the angular frequency equal to $2\pi f$ and t is time (see Figure 3.18(a)). PIV measurements were made in a set of 10 equally spaced phase angle locations across the voltage signal cycle and the flow chart was followed to produce 10 fully developed centreline velocities, $u_{cl,fd}$. The last step in the procedure was to fit a sinusoid through these 10 velocities (Figure 3.18(b)), and relate centreline velocities to the electrical signal through the known timing of the measurements, and to the average velocity through the analytical solution (Figure 3.18(c)).

This procedure was repeated across a range of frequencies to characterise the performance of the diaphragm. These experiments were performed at low voltages without the amplifier, and so were not limited to the frequency limit of $1500Hz$ of the amplifier. In Figure 3.19, $\bar{u}_{os}$ per volt for each frequency has been plotted. The peak output of diaphragm in this work lied at a frequency of $\sim 300Hz$. Throughout the experiments the performance of a number of devices was found to be consistent with Figure 3.19, and the output of each of the devices trialled was found to vary linearly with voltage across the range of voltages, $0 < V_{os} < 90$.

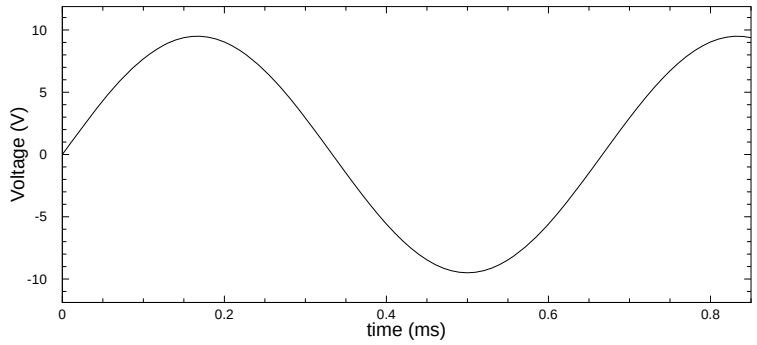

(a)

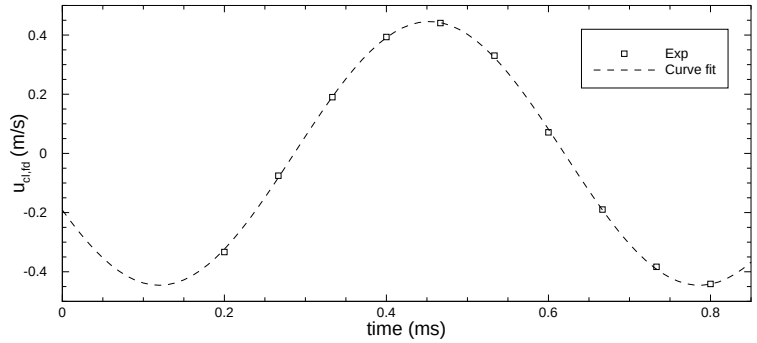

(b)

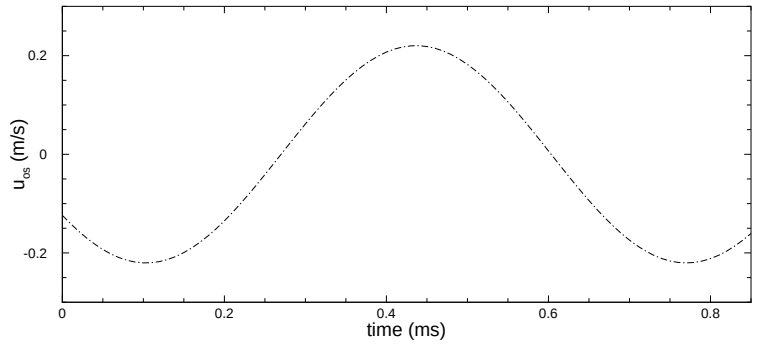

(c)

Figure 3.18: Signals plotted against time for $f = 1500Hz$. (a) Reference voltage signal. (b) Fully developed centreline velocity. Symbols are measured the velocities. Dashed-line is the curve fit. (c) Calculated average velocity from the analytical solution.

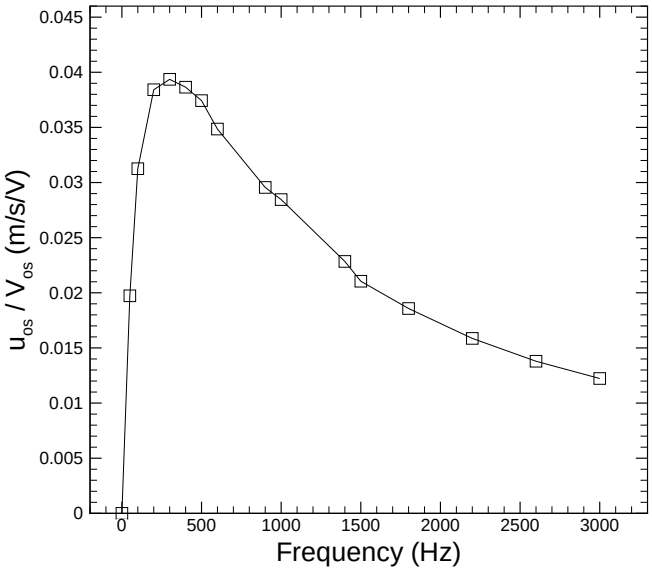

Figure 3.19: Average flow amplitude per volt against frequency. Experiments performed at $V_{os} = 10V$.

3.4 Experimental Uncertainty

The uncertainty analysis performed in this section is based on the guidelines provided by Coleman & Steele (1999) and the ideas proposed by Moffat (1988). The approach taken by Coleman and Steele is consistent with the methodology outlined by the International Organization for Standardization (ISO) in its publication 'Guide to the Expression of Uncertainty in Measurement'. The ISO guide has also been adopted in standards issued by a number of engineering institutions such as the American Society of Mechanical Engineers (ASME) and the American Institute of Aeronautics and Astronautics (AIAA).

Coleman & Steele (1999) suggested as a minimum all experimental data should be reported along with the systematic uncertainty, the random uncertainty, and the total uncertainty and its specified confidence level. The confidence level used exclusively in this work and recommended for the vast majority of engineering reporting is the 95% confidence level.

3.4.1 Uncertainty Analysis Methodology

Total uncertainty

The desired measurement value is often not measured directly. Instead it is derived from a number of other variables combined together in the form of a data reduction equation. Errors in the variables propagate through the data reduction equation and into the final result. A general representation of a data reduction equation for a result r from J measured variables is:

$$r = r(X_1, X_2, \ldots X_J) \tag{3.11}$$

The total error of the experimental value r is the summation of a systematic (or bias) error and a random (precision) error. The Root-sum-square (RSS) combination of the estimates for the systematic uncertainties B_r and random uncertainties P_r gives:

$$U_r^2 = B_r^2 + P_r^2 \tag{3.12}$$

For the 95% confidence large-sample analysis with no correlated precision errors the terms become

$$B_r^2 = \sum_{i=1}^{J} \theta_i^2 B_i^2 + 2 \sum_{i=1}^{J-1} \sum_{k=i+1}^{J} \theta_i \theta_k B_{ik} \tag{3.13}$$

$$P_r^2 = \sum_{i=1}^{J} \theta^2 P_i^2 \tag{3.14}$$

$$\theta_i = \frac{\partial r}{\partial X_i} \tag{3.15}$$

where B_{ik} is the covariance estimator for bias errors in X_i and X_k and θ is the sensitivity coefficient. The errors (bias and precision) are treated separately because they are estimated by different means.

Precision Errors

The precision error is the random component of the total error. Precision errors are evaluated on a statistical basis and their determination depends on whether the result is calculated from a single test or multiple tests. For multiple tests the precision error is the standard deviation, S_i, of N results multiplied by the coverage factor t,

$$P_i = tS_i \tag{3.16}$$

where t is determined from the degrees of freedom the the result, ν_r, and the t-distribution. The degrees of freedom of the result, ν_r, is not easily calculated in almost all cases and is based upon further estimation of variables. Therefore in the current work it is simply taken as $\nu_r = N - 1$. The precision errors in the current work are determined at the end result rather than at each measured value in order to eliminate the effects of correlated random errors. For a single test ($N = 1$) the standard deviation must come from previous experience with the particular measurement.

Bias Errors

The bias error is a fixed component of the total error and thus cannot be determined by statistically methods. Therefore they must be estimated with the best information at hand and often using engineering judgment alone (Coleman & Steele (1999)). As the total error is reported at the 95% confidence level the bias error also must be estimated with this same level of confidence. In this work the bias errors are identified and estimated at an elemental level and passed through the data reduction equation to calculate the final bias error. The details of the estimation of each measurement type made are described next for the each of the measured quantities.

3.4.2 Channel Cross-Section Measurement Uncertainties

The cross-section dimensions of the channel were estimated based on the measurements made using the optical profiler and the images taken by the SEM. The uncertainty in the measurements of the channel depth and width is estimated to be accurate to within $\pm 0.5 \mu m$.

3.4.3 Flow Rate Uncertainties

Two SGE gastight microvolume syringes ($5mL$ and $10mL$) are used in this work. They are guaranteed by the manufacturer to be accurate to within 1% of FS. Thus the accuracy of the average cross sectional area is good to at least to 1%. Similarly the syringe pump used to drive the syringe plunger is specified to be accurate to 1% of the set plunger speed. The flow rate is given by the product of plunger speed and plunger area (both accurate to 1%). Combining these errors in a RSS fashion the total bias error becomes $\sqrt{2}\%$ of the set flow rate.

3.4.4 MicroPIV Uncertainties

For a uniform displacement of tracer particle in an interrogation volume, the amplitude of the random component of error in the measurement, $\sigma_{\Delta x}$, can be described by

$$\sigma_{\Delta x} = cd_e \tag{3.17}$$

where c is a constant and d_e is the particle image diameter (Lindken *et al.* (2009)). The constant, c, varies in the range 0.1-0.05 (Prasad *et al.* (1992), Boillot & Prasad (1996), Westerweel (2000)). Taking $c = 0.05$ and $d_e = 8pixels$ from the previous section, the error becomes $\sigma_{\Delta x} = 0.4pixels$. Along the centreline a uniform displacement of the tracer particles is a reasonable assumption, and in the current experiments the pixel displacement along the centreline ranged from $8 - 16pixels$ and thus the error from $2.5 - 5\%$. Away from the centreline, particularly close to the channel walls, the velocity gradients are large and the error is increased from this value.

The bias error estimate for PIV measurements and large particle image diameters, $d_e > 2$, can be considered negligible compared to this random component (Prasad *et al.* (1992)) and therefore it was neglected in the current study.

3.4.5 Fully Developed Centreline Velocity Uncertainties

The fully developed centreline velocity, $u_{cl,fd}$, was calculated from the curve, Equation 3.8, fitted to the centreline velocity measurements. Repeat measurements were made to determine the value of $u_{cl,fd}$ and the precision error was

calculated based on this variation. The bias error sources for this measurement are the errors arising from locating the centreline, the errors in the PIV measurements, and errors from the curve fitted to the data.

The bias error in the determination of the centreline was half the resolution of the PIV measurements, and equal to $\pm 1.3\mu m$. The variation of the fully developed velocity in this region from the numerical study was about 1% and thus the bias error of this component taken equal to 1% of $u_{cl,fd}$. The error from the PIV measurements was considered as purely random, and therefore the bias component taken as zero. The bias error of the curve fitted to the centreline velocity was estimated from the error in using this fit on the numerical results. The curve consistently overestimated the fully developed velocity by approximately 0.1%, a negligibly small amount compared the other errors.

3.4.6 Entrance Length Uncertainties

The entrance length in the current work is defined as the distance from the inlet to the location downstream where the centreline velocity has reached 99% of its fully developed value. As with $u_{cl,fd}$, repeat measurements were made to determine the entrance length and the precision error was calculated based on this variation. The bias error sources include positioning errors, errors in the PIV measurements and errors due to the curve fit procedure. The positioning errors come finding the centre depth in the channel, the exact inlet location, and the centreline within the plane.

The overwhelmingly dominant bias error occurred from the curve fitted to the centreline velocities. This bias was largest for shorter entrance lengths, ranging from 21% for $L_e \approx 30\mu m$, to 3% for $L_e \geq 33$. The error was represented as a function of L_e,

$$\sigma_{L_e/2a} = 10(L_e/2a)^{-1.27} \tag{3.18}$$

which was determined using a power law fit to the difference between $L_e/2a$ calculated directly from the numerical data and using the curve fitted to the numerical data.

3.5 Numerical Modelling

For low Reynolds number flows accurate calculation of the flow in the entrance region of a pipe can only be achieved by the solution of the full set of Navier-Stokes equations. Fortunately, Computational Fluid Dynamics (CFD) is well adapted to generate a near-exact simulation of laminar flow problems (White (1991)), limited only by computing power and irregularities in the geometry of the flow region. In order to examine the accuracy of the experimental method, numerical simulations were performed for steady flow at approximately the same conditions as in the experiments. Of chief concern was the accuracy of using the curvefit, Equation 3.8, in the determination of the entrance length and its associated uncertainty.

The computations were performed by the commercial package ANSYS FLUENT (V13.0), using a finite volume, pressure-based solver. All simulations used a three dimensional domain and made use of 64-bit double precision processing. A second-order upwind differencing scheme was used for the advective terms, and the SIMPLE algorithm, as named by Patankar (1980), was employed to treat the pressure-velocity coupling. Two other differencing schemes, QUICK and MUSCL were also trialled and the differences in calculated entrance length between the three schemes was found to be negligible. Therefore the second-order upwind scheme was employed, as the more conventional scheme. Under these conditions, cases generally took between 2000 and 7000 iterations to reach a converged state. Convergence was defined a when the mass and momentum scaled-residual errors ceased to change by more than approximately 0.01% over 500 iterations.

Of prime importance for the flow in the current work is the accurate account of the geometric features that exist within the microdevice. The fluidic chip is too large to model in entirety with sufficient resolution, and only a restricted portion of the device has been incorporated into the model.

3.5.1 Meshing Strategy and Boundary Conditions

The modelled flow domain can be seen in Figure 3.20, and the entire length of channel in the microfluidic device was represented but due its large size only a portion of the chamber was included. In order to save computation time, a symmetry plane was implemented along the centreline of the channel that ran

parallel to the vertical direction (the z-axis). The upper surface of the channel and chamber, the bonded pyrex layer, was modelled as a perfectly flat surface. The walls of the chamber and channel were approximated to be perfectly vertical and formed right angles with the upper surface. The walls at the entrance to the channel were shown in the SEM images (Figure 3.6) to be slightly rounded but in the numerical model they were simplified as having a perfectly square edge. The lower surface of the device, the etched silicon surface, varied substantially in the entrance region and needed to be accurately represented in the numerical model. Both the SEM image (Figure 3.5) and optical profiler measurements were used to generate an accurate approximation of the lower surface. A full description of the method used in this approximation of lower surface geometry is given in Appendix A.

Only the flow rate set on the syringe pump was known and the distribution of the flow along the modelled boundaries of the chamber had to be approximated. As the modelled boundaries were far from the channel inlet, the flow inside the channel was fond to be insensitive to the exact conditions imposed on the chamber boundaries. Increasing the size of the modelled domain also had essentially no impact on the flow in the entrance region. The chamber boundary parallel to the y-axis, located at $x/a = -10$, which can be seen in Figure 3.20(a), was set to have a uniform velocity distribution equivalent to half the flow rate set on the syringe pump (as half the channel is modelled). The chamber boundary parallel to the x-axis, located at $y/a = 6$, which can also be seen in Figure 3.20(a) was modelled as a solid wall with a zero shear stress condition applied along it length, as to allowed slip. The outlet of the channel was modelled as outflow.

The mesh generation was performed using ANSYS ICEM CFD (V13.0). The mesh in the midplane of the entrance region, $z = 0$, is presented in Figure 3.20(b). The elements in the z-direction were uniformly spaced, and in the x-direction and y-direction the elements were varied in size, so that more elements occurred in the regions of greater importance and higher velocity gradients. In the chamber, the mesh was allowed to become more coarse in the regions further from the channel inlet as can be seen in Figure 3.20(b). Inside the channel, the elements were uniform in the y-direction, so that at each x-location, as shown in Figure 3.20(c), the elements were approximately uniform throughout the cross-section. Along the x-axis in the channel, the elements were allowed to grow slowly in size,

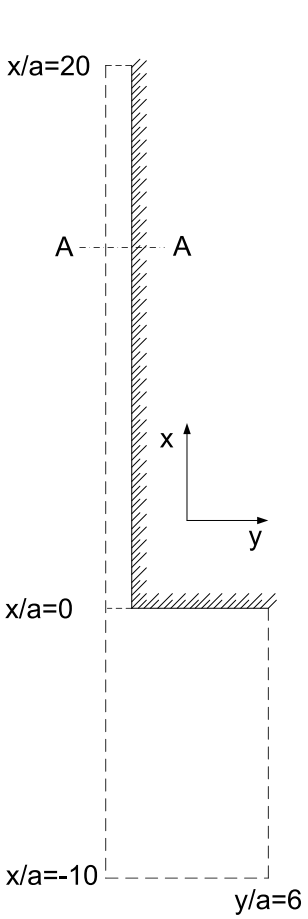

(a) Numerical Domain

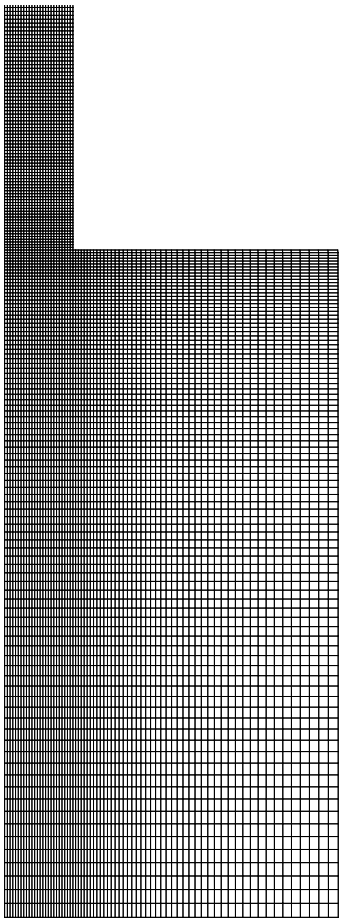

(b) Portion of the CFD mesh across the midplane, $z/a = 0$

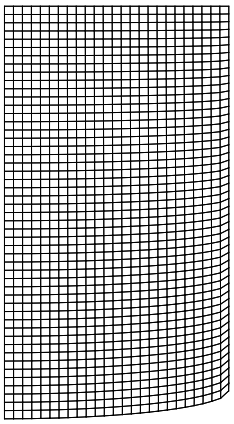

(c) CFD mesh at cross-section A-A

Figure 3.20: Geometry of the channel and chamber region used in the numerical model.

reaching an aspect ratio of 3.5:1 at the end of the channel.

A grid convergence study was performed to investigate the influence of grid resolution on the resulting entrance length. The grid density was progressively increased by a factor of two, until a further increase in the number of elements resulted in negligible difference in the results. Grid-independent solutions were achieved on a final grid consisting of 650,000 elements.

Chapter 4

Steady Flow in the Entrance Region

This chapter presents the results of microPIV measurements and numerical simulations performed in the entrance region of a channel for the microdevice described in Chapter 3. First the fully developed velocity distribution for the current microchannel cross-sectional geometry are established. The developing flow in the entrance region connecting the chamber to the channel is then examined and its key features discussed. Inside the channel, for $1 \leq Re \leq 66$, developing profiles across the midplane of the channel are extracted and the development of the centreline velocity analysed. The centerline velocities are used to calculate the entrance length and evaluation of this method for the geometry is included. Experimentally and numerically determined entrance lengths are presented and a correlation for the current geometry proposed. Finally these results are compared with numerical results for flow under various idealised conditions.

4.1 Fully Developed Flow

Flow downstream of the inlet becomes fully developed where the velocity only changes minutely with further distance downstream. Providing the flow is laminar, the fully developed velocity distribution that is established is a function of the channel geometry only. For the cross-section described in Section 3.1.2, a contour plot of the fully developed velocity distribution taken from the numerical

solution is presented in Figure 4.1. This distribution was extracted at a location approximately $16a$ from the entrance for $Re = 22$. The velocities have been normalised by the cross-sectional average velocity and the lengths by the halfwidth, a.

The maximum velocity in Figure 4.1 lies along centre plane, $y = 0$, at a depth of $23.52\mu m$ or $0.9118a$ below the flat pyrex surface, almost exactly halfway in-between the upper and lower surfaces. The distance between the upper and lower surfaces varies in the entrance region, which causes the depth of the midplane to also change. The plane of interest is where the maximum velocity occurs in the fully developed region, and therefore the depth found for the maximum velocity in the fully developed region has been set to $z = 0$. This plane will be referred to as the midplane and the line that passes through $y = 0, z = 0$ in the x-direction as the centreline.

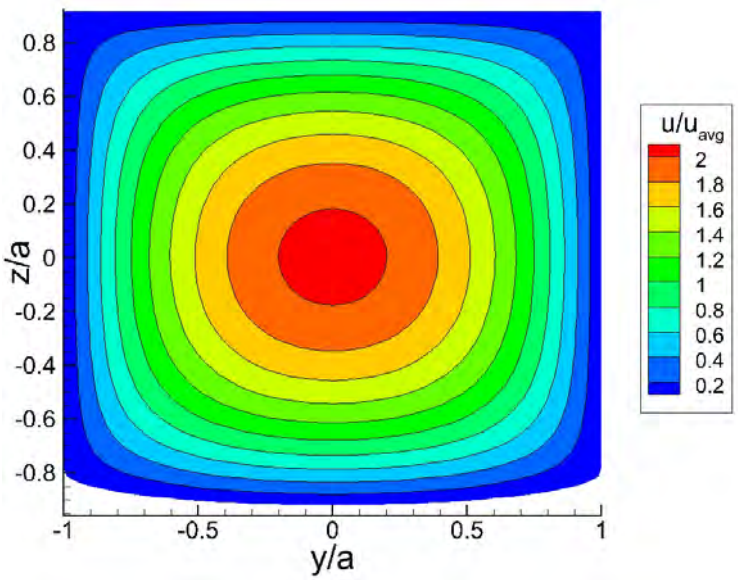

Figure 4.1: Contour plot of fully developed velocity distribution normalised by $\bar{u}$ denoted as u_{avg} in the figure.

In Figure 4.2 a comparison is made between fully developed profiles obtained by experimental, numerical, and analytical means along the midplane, $z/a = 0$. The numerical prediction and experimental results from a single case, again for $Re = 22$ are shown in Figure 4.2(a). Overall the experimental results lie close to

the numerical solution and are in particularly good agreement is achieved within the central region of the channel. Towards the walls, $y/a < -0.75$ and $y/a > 0.75$, the agreement is not as good, due to the larger velocity gradients in this region, which caused the PIV results to over predict the velocity in this region.

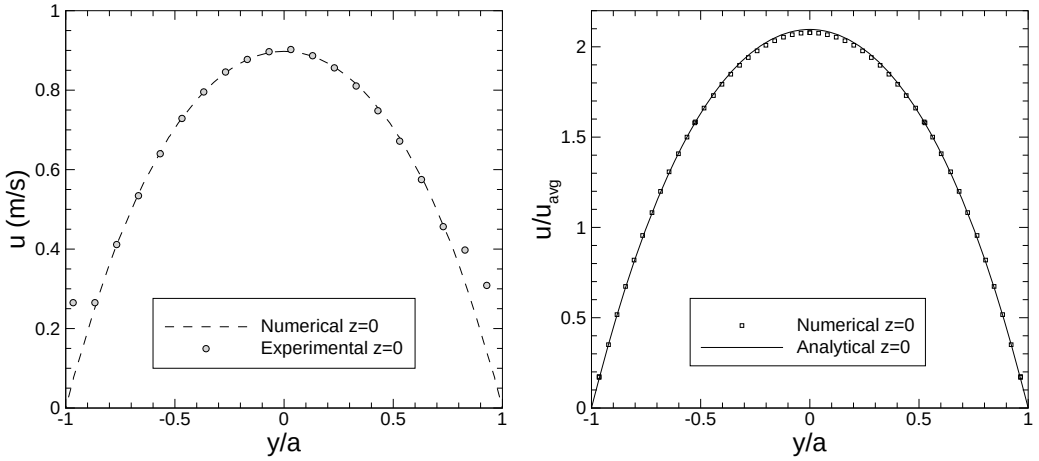

(a) (b)

Figure 4.2: Comparison of fully developed velocity profiles on the centreplane $z = 0$. (a) Experimental and numerical results for $Re = 22$. (b) Numerical and analytical results (White (1991)) normalised with $\bar{u}$.

A comparison between the numerical results and the analytic solution of White (1991) to steady flow in the idealised geometry of a square cross-section, has been presented in Figure 4.2(b). The agreement between the two curves is very good, particularly in the regions close to the channel walls. The largest discrepancy occurs near the peak velocity and the numerical results for the current geometry have a lower maximum velocity than that of the analytical solution. For a square cross-section the maximum velocity is 2.096 times the average velocity (Shah & London (1978)) and for the current geometry the maximum is 2.078 times the average velocity, a difference of approximately 1% from the solution for a completely square cross-section.

The velocity distribution within the fully developed region of the channel is invariant in the streamwise direction. In the entrance region the velocity distribution can vary substantially, and depends on the geometry of the inlet and the region upstream of the inlet, and also the Reynolds number. The region leading

up to the channel inlet has been known to affect the flow development for low Re (Vrentas *et al.* (1966)), which makes the description of the entire entrance region necessary in this study.

4.2 Entrance Velocity Fields

The majority of research on entrance flow studies have only been interested in the flow inside the channel and assumed a uniform velocity distribution at the inlet. Numerically there exists a handful of studies in which the fields upstream of the entrance have been described. These include numerical work by Wang & Longwell (1964) who studied flow with a the streamtube entry, Vrentas & Duda (1973) who investigated flow in a sudden contraction in a pipe, and Sparrow & Anderson (1977) who researched flow into a square edge entry from a large reservoir. Surprisingly, experimentally only for flow through a sudden contraction has the region upstream of the entrance been presented in detail, for example, Durst & Loy (1985). The combination of both numerical and experimental results for the current experimental arrangement provides a unique opportunity to examine flow throughout the entire entrance region.

The flowfield in the chamber as it approaches the entrance and develops towards its asymptotic state in the channel is shown in Figure 4.3. Flow from the chamber accelerates as it approaches the channel entrance, just as flow approaching a sink would, as the dimensions of the channel relative to the chamber are very small ($a << R$). In Figure 4.3(a) the vector field has been formed from two PIV measurement fields that have been stitched together and Figure 4.3(b) is the numerical result, both for the case of $Re = 33$. The experimental result, Figure 4.3(a), can be seen to be highly symmetrical across the centreline thereby confirming the appropriateness of the symmetry condition applied to the numerical model.

To get a more quantitative picture of the flow in the entrance region, in Figure 4.4 the development of flow in the streamwise direction has been plotted for a number of cross-section locations for the same experimental case of $Re = 33$. In the midplane, $z = 0$, a number of y/a locations have been extracted from the experimental and numerical results and are shown in Figure 4.4(a). Overall the agreement between experimental and numerical results is very good, particularly

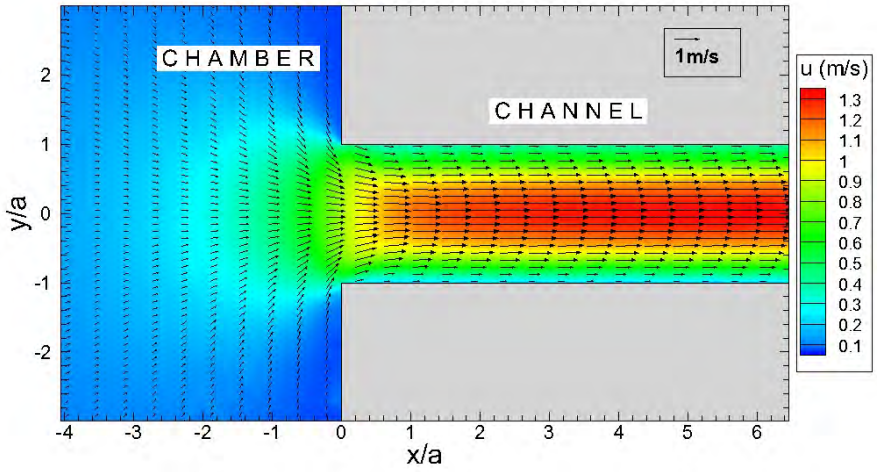

(a)

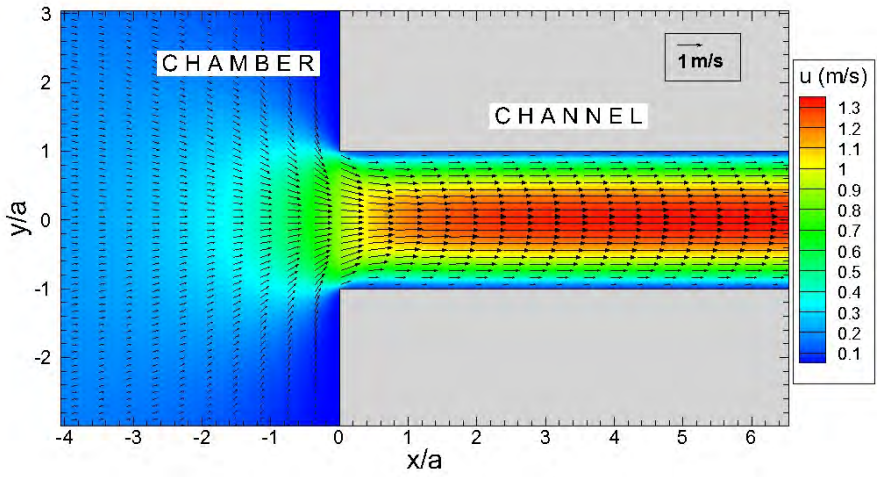

(b)

Figure 4.3: Entrance region flow for $Re = 33$. (a) PIV vector field. (b) Numerical streamlines.

for cross-section locations close to the centre of channel, $0 < y/a < 0.61$. For these locations, the experimental velocities under predict the numerical results by a small margin of about 2%. As identified earlier, closer to the wall the PIV measurements overpredict the velocity and this can be seen at $y/a = 0.90$. The results also differ upstream of the entrance, $x/a < -2$, most likely due to simplifications in the numerical model.

The numerical results in Figure 4.4(a) show the flow along the midplane accelerating almost uniformly regardless of y/a location until the channel entrance, $x/a = 0$, where the flow near the wall, $y/a = 0.81, 0.90$ then abruptly deccelerates as it is slowed by viscous action caused by the presence of the channel wall. This effect also occurred experimentally but was far less accentuated, most likely due to the slight rounding on the inlet corners found in the SEM image shown previously in Figure 3.6. The inlet corners only have a very small amount of rounding and therefore a 90 degree corner was implemented in the numerical model as an accurate representation of the channel entrance. The good agreement between the results presented here further justifies this modelling simplification. In Figure 4.4(b) the development at various z/a locations across the centreplane have been plotted from the numerical results. Unlike for the y/a plots, as the flow approaches the channel inlet it has a distinct velocity distribution in the z-direction. This variation of velocity is the effect of the planar plenum style entry, with the upper and lower surfaces of the device causing the flow to develop in the z-direction before the channel inlet. In the velocity distributions along $z/a = -0.63$ and $x/a = -0.82$ there is a slight peak in the velocity values but it is not as large as occurred in the y-direction along the midplane. This increase of velocity occurs because of the decrease in depth of the lower surface as the flow approaches the channel inlet, the details of which were presented in Section 3.1.2.

The flow in the chamber presented in this section was for $Re = 31$, but the key features identified were common to all Reynolds numbers studied in the range $1 \leq Re \leq 66$. While the velocity fields in the chamber were interesting in their own right, the region of most interest in the current study is the region inside of the channel in the immediate vicinity of the inlet.

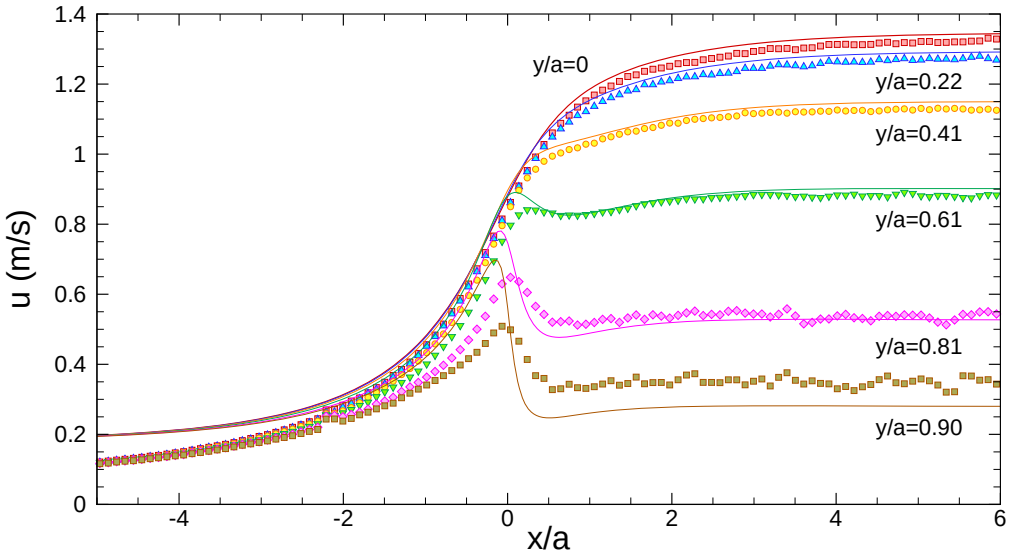

(a)

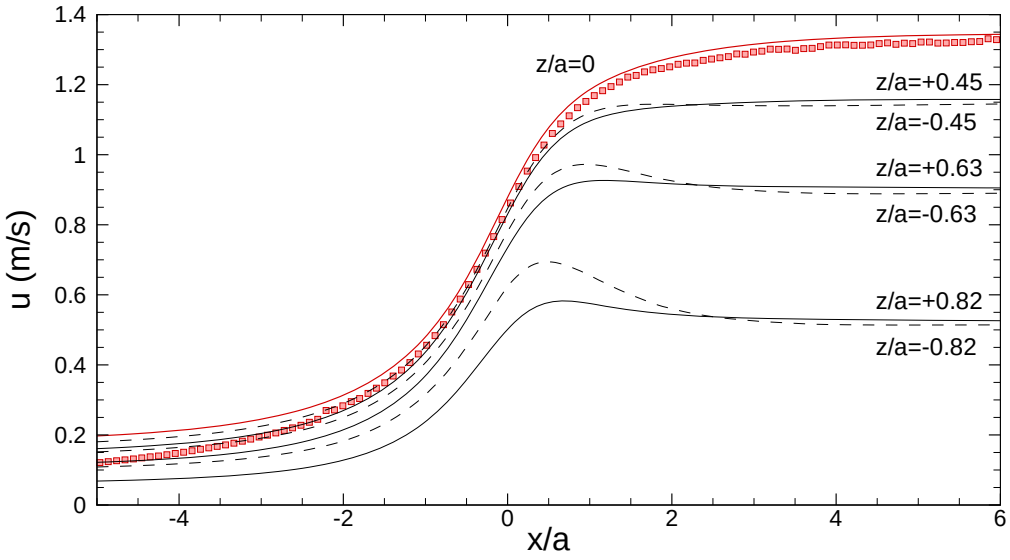

(b)

Figure 4.4: Development of flow in the streamwise direction at various cross-section locations for $Re = 33$. The solid and dashed lines are the numerical results. Symbols are experimental values.(a) Various y/a locations across the centreplane, $z = 0$. (b) Various z/a locations across the symmetry plane, $y = 0$.

4.2.1 Developing Velocity Profiles

PIV measurements were made in the channel along the midplane ($z/a = 0$) for eight different Reynolds numbers, $Re = 1, 6, 11, 22, 33, 44, 55, 66$, and each repeated five separate times. From a single set of measurements, developing velocity profiles have been extracted at various streamwise locations and plotted against the numerical results in Figures 4.5-4.8. In these figures the overall agreement between the numerical and experimental profiles is very good, particularly towards the centre of the channel ($y/a = 0$). As identified for the fully developed flow, near the channel wall the larger velocity gradients mean that accurate PIV measurements are difficult to obtain with a consequent overestimation of the velocity, as can be seen in a number of these plots. It can also be seen that better agreement, at least for the central region of the channel, between numerical and experimental values occurred at larger Reynolds numbers, $Re \geq 22$, where the flow was found to show far less variability.

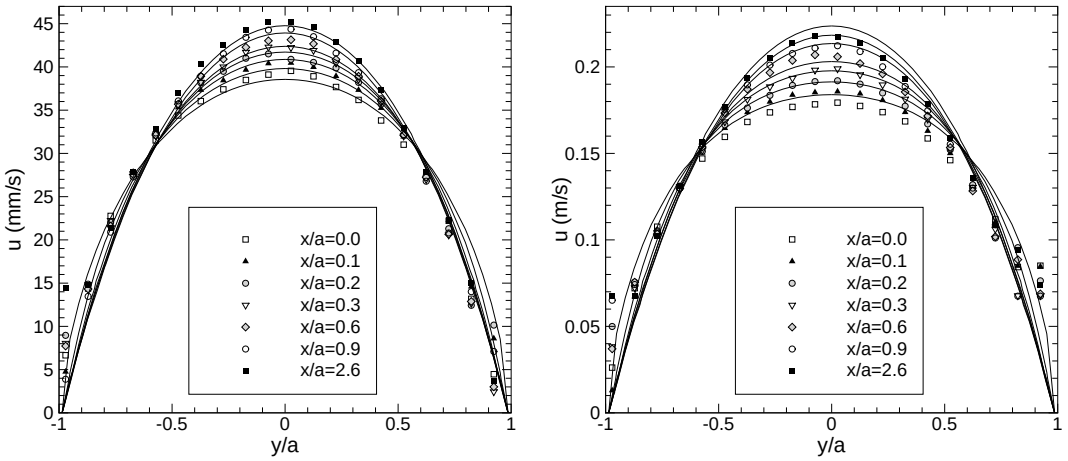

(a) Re=1 (b) Re=6

Figure 4.5: Developing velocity profiles for $Re = 1$ and 6 at various streamwise locations and $z/a = 0$. Symbols experimental values. Solid lines are the numerical result at the same x/a location.

For the slower flows, $Re = 1$ or 6, shown in Figure 4.5, experimentally the flow took a much longer time to stabilise, and there were much larger variations in measured velocity magnitudes between different experimental runs than for the higher Re cases. This can be seen in the profiles in Figure 4.5 where the

overall shape of the profiles are in very good agreement but the magnitudes are consistently different to the numerical predictions. For $Re = 1$, Figure 4.5(a), the velocity values are consistently above the numerical solution, and in Figure 4.5(b) for $Re = 6$ consistently below. Rather than a measurement error, it is suggested that this discrepancy is a physical occurrence and caused by variation of the actual flow rate set by the syringe pump at these lower flowrates. This was also reported by Lee *et al.* (2008) for a similar syringe pump. The underlying reason for conclusion, is that in the fully developed region for the higher Reynolds number flows, the PIV technique consistently measured the centreline velocities with substantially lower variability. Yet due to the timing scheme employed in the PIV measurement, in this region (the fully developed region), all cases should look identical as far as the PIV technique is concerned regardless of Re, as they all have the same particle image displacement. It cannot also simply be a positioning error, as all plots in Figures 4.5 - 4.8 used the same relative locations between numerical and experimental results. Furthermore, a positioning error would not cause a problem from the final profiles measured in the fully developed region.

With the nuances of the experimental measurements described, the flow features in Figures 4.5 - 4.8 can now be discussed. In Figure 4.5, the flow entering the channel, at x/a, already has a highly developed shape and for $Re = 1$ the centreline velocity is already 87% of its fully developed value. This amount of predevelopment in the profiles is a feature of low Reynolds number flows and is not a feature solely due to the physical entrance geometry, as it has been shown in all numerical studies where the region upstream of the inlet was also modelled. For example, at $Re = 1$ the centreline velocity was found to be over 80% of its fully developed value by Vrentas *et al.* (1966) for the streamtube entry into a circular pipe, and Sparrow & Anderson (1977) showed that for a square edge entry into parallel plates the value is about 90%. It can also be seen in 4.5, that the distances taken to reach the fully developed state are very short; of the order of about one half width, a.

A large amount of predevelopment also occurred for larger Reynolds number flows but the level of development decreased with increases in Re. In Figure 4.6, the inlet profiles, $x/a = 0$, take a much rounder shape, with a flatter distribution in the centre region. For $Re = 22$, Figure 4.6(b), the centreline velocity at the entrance is about 70% of its fully developed value, which is still significantly

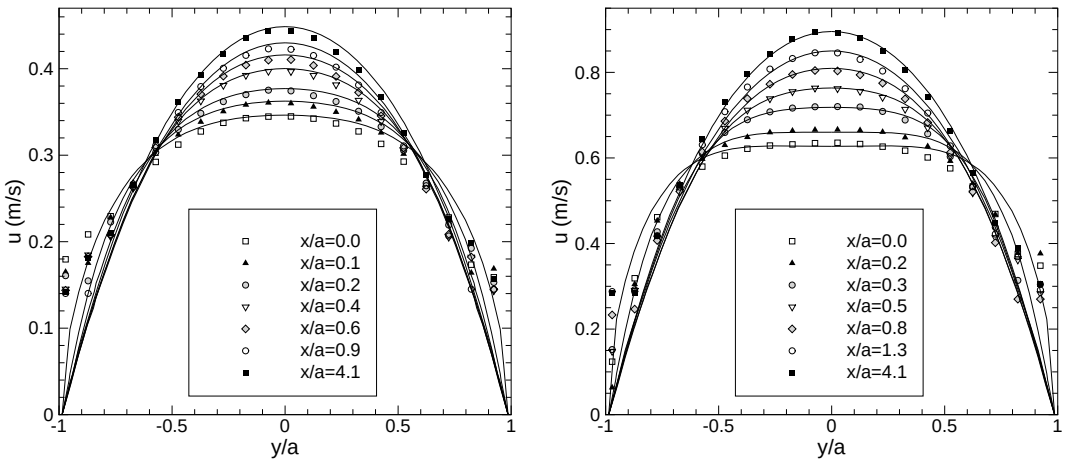

(a) Re=11 (b) Re=22

Figure 4.6: Developing velocity profiles for $Re = 11$ and 22 at various streamwise locations and $z/a = 0$. Symbols experimental values. Solid lines are the numerical result at the same x/a location.

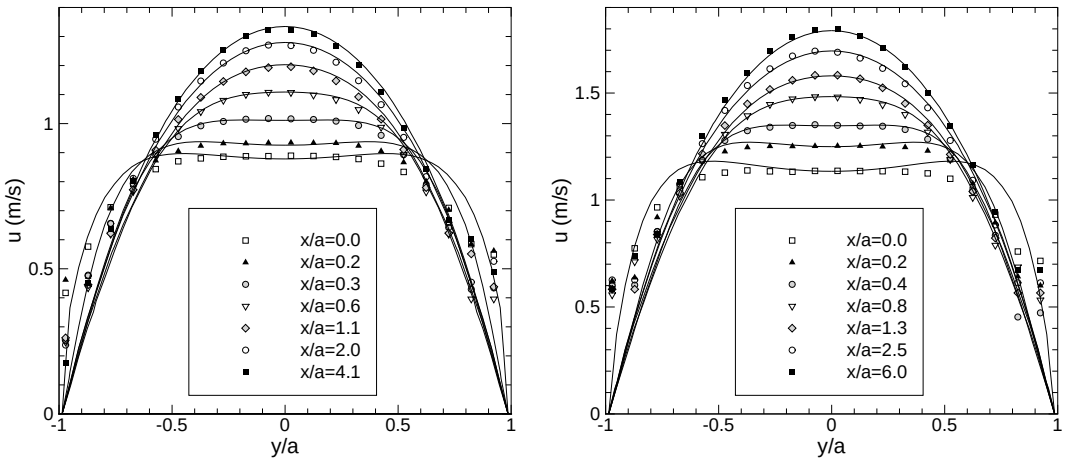

(a) Re=33 (b) Re=44

Figure 4.7: Developing velocity profiles for $Re = 33$ and 44 at various streamwise locations and $z/a = 0$. Symbols experimental values. Solid lines are the numerical result at the same x/a location.

higher than for a uniform distribution at the entrance, which would be 48% for the current channel cross-section. The distance required for the profiles to develop also substantially increased compared with the short lengths seen for $Re = 1$ and $Re = 6$.

For further increases in Reynolds number, in Figure 4.7 the flow behaved much more like typically studied entrance flows and entered with a profile that has a flat velocity distribution across a large portion of its core. As the flow proceeds downstream, close to the solid boundaries the flow is slowed, and the profiles become successively more rounded in order to satisfy continuity. Interestingly, in Figure 4.7(a) there is the first appearance of an offset of the maximum velocity from centreline, but in this case it can only be seen in the numerical result. For further increases in Re, the magnitude of the overshoot in the numerical results is also found to increase.

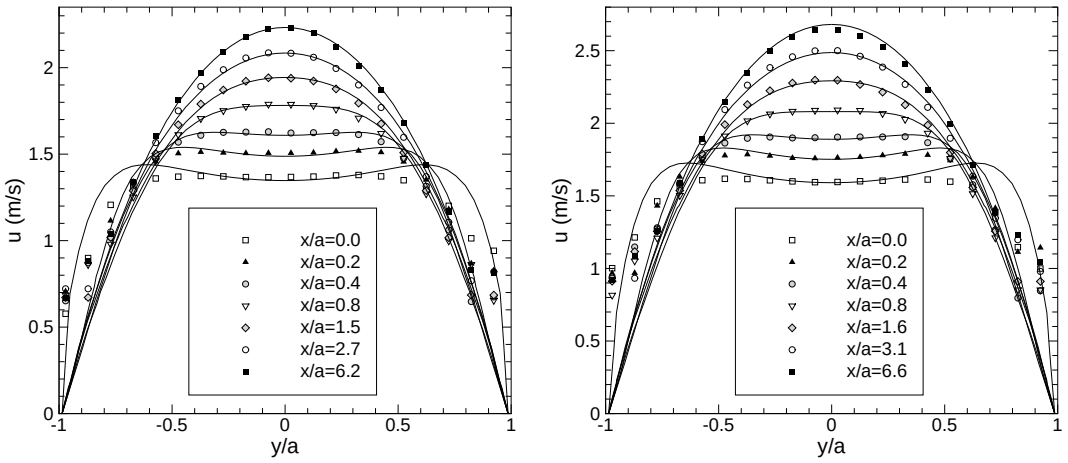

(a) Re=55 (b) Re=66

Figure 4.8: Developing velocity profiles for $Re = 55$ and 66 at various streamwise locations and $z/a = 0$. Symbols experimental values. Solid lines are the numerical result at the same x/a location.

For the two largest Reynolds numbers, $Re = 55$ and 66, the developing profiles experimentally and numerically are very similar, with the largest difference occurring at $x/a = 0$. Here at the inlet, the first sign of off centre maxima in the experimental results occurs for $Re = 66$ in Figure 4.8(b). The maximum velocity for this profile lies at $y/a = -0.47$ and is only 1.4% of the centreline

value. In the numerical results the overshoot has become quite substantial and for the same case is 8.5% of the centreline value. Christiansen *et al.* (1972) found similar overshoots for flow through a sudden contraction, with a maxima equal to about 5% of the centreline value. Later, however it was suggested by Kim-e *et al.* (1983) that this result of such a large overshoot was the product of insufficient mesh resolution in this region. A number of meshes were trialled which had a significant level of refinement in this region, however it was found that the increased resolution had no impact on the overshoot.

The developing velocity profiles presented in this section showed good agreement between with the experimental results and numerical predictions, particularly in the central region of the channel. As the entrance length was defined from within in this region, it was critical that excellent agreement was achieved along the centreline, $y/a = 0, x/a = 0$. In order for this to be confirmed a more close up examination of the centreline velocities is required.

4.2.2 Developing Centreline Velocity

The developing centreline velocity in the streamwise direction has been plotted in Figures 4.9 and 4.10 for the same experimental cases presented previously for the developing velocity profiles. For all cases the initial centreline velocity at the inlet increases in the downstream direction and appears to approach a constant value asymptotically as expected for developing flow. In this case, very early in the channel the centerline velocity also increases in a magnitude because of the reduction in cross-sectional area cause by the change in depth of the lower silicon surface. As discussed previously, at $x/a = 1$, the depth is within 2% of its final value further into the channel and by $x/a = 2$ it is within 0.6%, which after this point should have a negligible effect on the flow. For the lowest Reynolds number cases however this geometric variation will have a significant influence on the flow development.

The two lowest Re cases, $Re = 1$ and $Re = 6$ plotted in Figure 4.9, a fair amount of scatter in the velocity measurements can be seen. This scatter represents the consistency of the flow at lower flow rates, which was only very small, of the order of 1%. The disparity between the numerical and experimental cases found in the comparison of the developing profiles, can also clearly be identified in

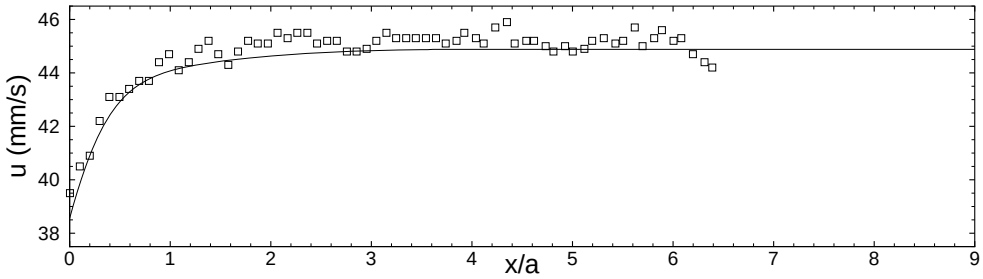

(a) Re=1

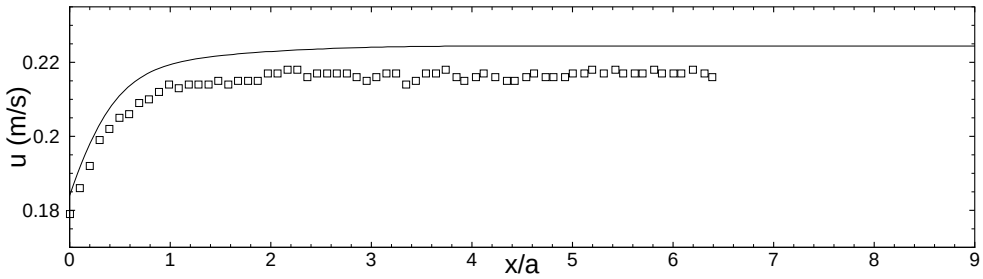

(b) Re=6

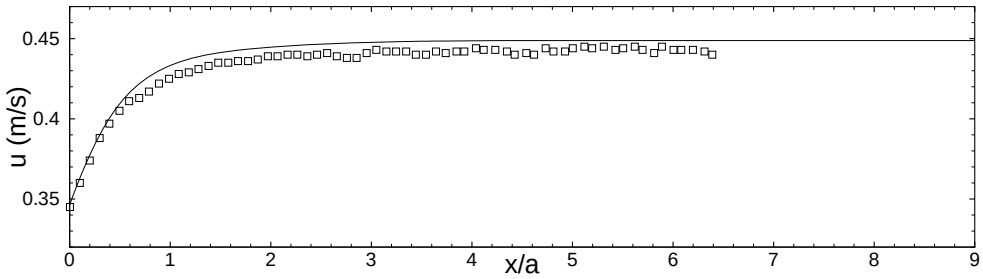

(c) Re=11

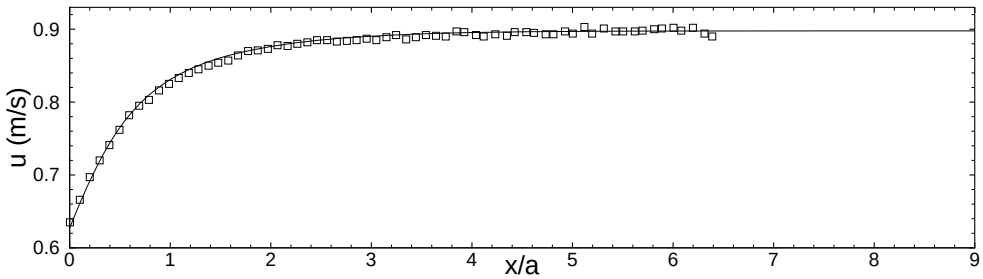

(d) Re=22

Figure 4.9: Developing centreline velocity at various streamwise locations for $1 \leq Re \leq 22$. Symbols experimental values. Solid lines are the numerical result.

these figures. For example, at the lower experimental velocities found for $Re = 6$ as shown in Figure 4.9(b) the difference becomes much more apparent due to the restricted y-axis range. However, even this seeming large discrepancy is actually only about 3%. Slightly lower values for the experimental result for $Re = 11$ are also noticeable in Figure 4.9(c), however in Figure 4.9(d) the experimental values for $Re = 22$ lie exceptionally close to the numerical curve.

For larger Reynolds numbers the agreement between numerical and experimental centreline velocities is exceptionally good. In Figure 4.10, for $33 \leq Re \leq 66$, the numerical curve passes close measured values throughout the entire range. For the largest Reynolds number, $Re = 66$ in Figure 4.10(d), the flow appears to reach its fully developed condition slightly outside the measurement range. For all other Reynolds numbers the size of the measurement plane appears sufficient to capture the full development process.

Overall for the range of Reynolds number examined in Figure 4.9 and Figure 4.10 the agreement between methods is good, almost always within a few percent of each other. The uncertainty estimated for PIV measurements along the centreline was given as $2.5 - 5\%$ of the true value, with 2.5% applying to the fully developed velocity. With the exception of $Re = 6$, which had the maximum discrepancy of 3%, all other datas sets fell within the predicted uncertainty. This suggests that the accuracy of the experimental measurement technique, the uncertainty estimation and the assumptions implemented in the numerical model are justified. The differences that do exist are largely due to the accuracy with which the flowrate can be set. This can be accounted for by proper normalisation of the centreline velocity, which will now be described.

4.3 Calculation of Entrance Length

The definition of entrance length employed here is the distance from the inlet to the location downstream where the centreline velocity reached 0.99% of its fully developed value. The entrance length can be evaluated in a number of different ways but all require accurate knowledge of the fully developed centreline velocity. The method employed by Lee *et al.* (2008) incorporated a curve fit to the centreline velocities. This method improves the accuracy and robustness of the calculation by using a series of data points, and by using the same data for

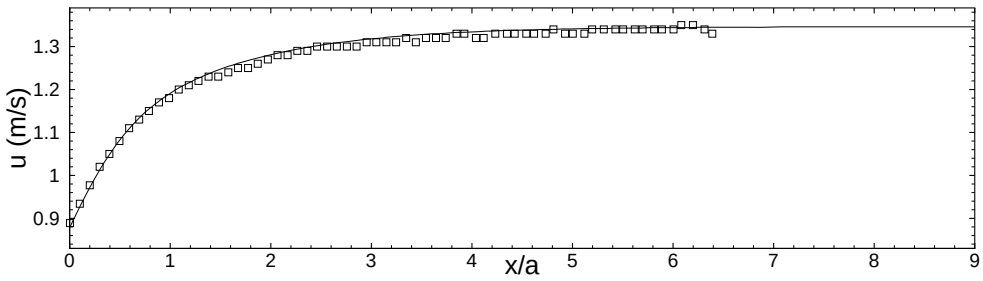

(a) Re=33

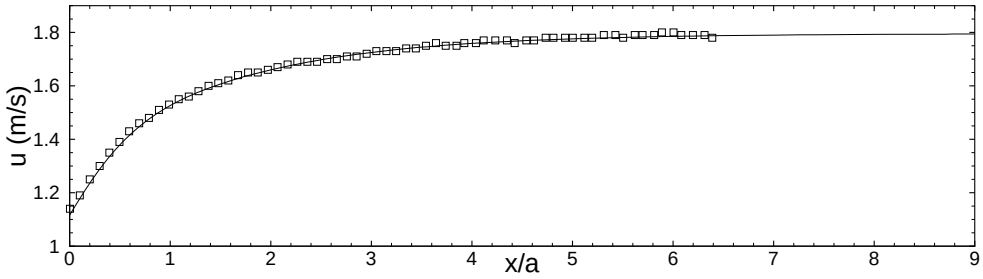

(b) Re=44

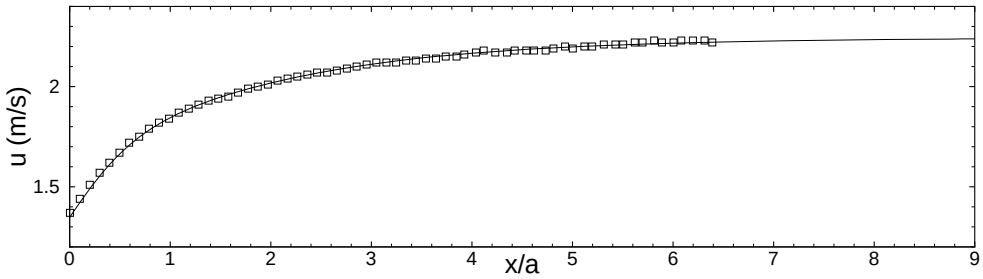

(c) Re=55

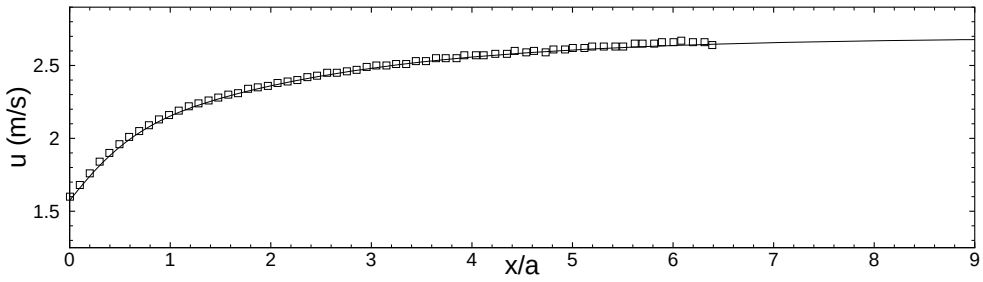

(d) Re=66

Figure 4.10: Developing centreline velocity profiles at various streamwise locations for $33 \leq Re \leq 66$. Symbols experimental values. Solid lines are the numerical result.

calculation of both the fully developed centreline velocity and entrance length. This is true provided that a suitable curve is fitted to the centreline velocity measurements. Lee *et al.* (2008) used a curve of the form of a decaying exponential function,

$$u = C_1 - C_2 e^{-C_3 x} \tag{4.1}$$

which was fitted to the centreline velocity to determine constants C_1, C_2 and C_3. C_1 is the asymptotic centreline velocity, $u_{cl,fd}$ and therefore the entrance length was the x location that yielded $u = 0.99C_1$. Lee *et al.* (2008) found that this equation provided an excellent fit to their developing centreline velocities for a similar range of Reynolds numbers as used in this research.

To test the accuracy of this method for the current work, Equation 4.1 was applied to the numerical results, where due to the small mesh sized used, the entrance length could also be accurately determined by inspection of the raw numerical data. In Figure 4.11, Equation 4.1 has been applied to the centreline velocity from the numerical simulation of $Re = 44$. Overall the fit of the curve describes the numerical data very well, with a goodness of fit, $R^2 = 0.9955$, and this level of fit was found for all Reynolds numbers. On closer inspection, the data varies systematically about the exponentially decaying curve, which can be seen more clearly in the plot of the residual difference between the two curves, show as the blue curve in Figure 4.11. In all Reynolds number cases, the same trend occurred and the curve fit systematically underestimated the fully developed centerline velocity.

The most important test for this particular curve fit is in how accurately it determines the fully developed centreline velocity, and the entrance length. The entrance length calculated by both inspection and using the curve fit to the numerical data and on the experimental cases presented so far, can be seen in Table 4.1. The curve fitted to the experimental and numerical results produces similar values of the entrance length, as would be expected from the high level of agreement agreement shown for the centreline velocities in Section 4.2.2. These values of entrance length however, differ quite significantly from inspection of the numerical data. Comparison of the two methods applied to the numerical results is given as the percentage difference in Table 4.1.

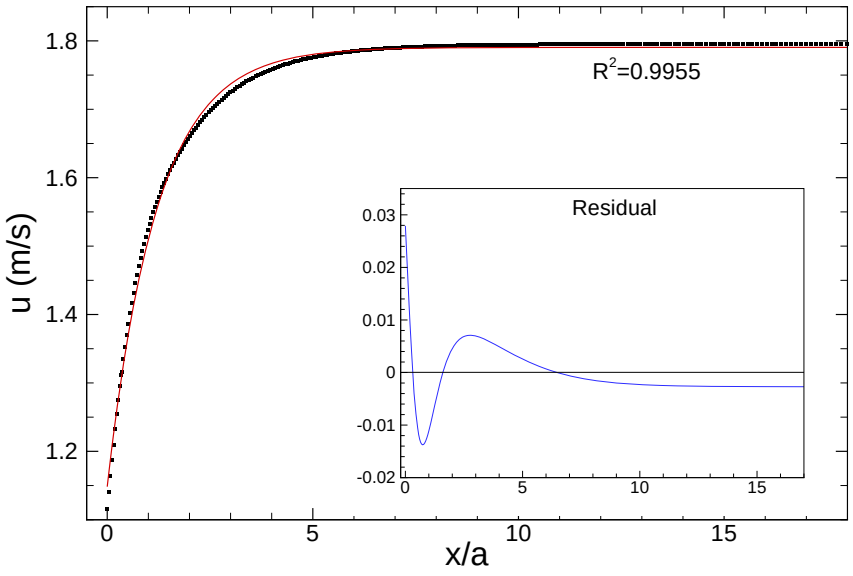

Figure 4.11: The decaying exponential function, Equation 4.1, fit to the numerical centreline velocity distribution for $Re = 44$. Symbols are the numerical result. Solid red line is the curve fit. Blue line is the residual difference between the curvefit and numerical values.

Table 4.1: Entrance length calculated using Equation 4.1 and by inspection of numerical results. Percentage difference is between the two numerical results.

Re	L_e (μm)			%Difference
	Exp curve fit	Num curve fit	Inspection	
1	35.0	32.4	39.1	-17
6	34.8	35.2	42.5	-17
11	47.3	43.2	50.0	-14
22	69.7	64.3	72.9	-12
33	91.7	87.8	101.1	-13
44	111.4	112.2	132.9	-16
55	131.4	137.1	166.2	-18
66	149.4	161.9	200.2	-19

Clearly, the effect of this systematic variation of points around the curve of the L_e shown in Figure 4.11 can be evaluated by this comparison, with the curve fit underestimating the entrance length by almost 20%. This is a rather remarkable discrepancy, and shows the sensitivity of the entrance length determination to the calculation method. The plot of the curve in Figure 4.11 and the results in Table 4.1 both show that a single exponential function cannot accurately describe the centreline velocity over the entire entrance region for the current geometry. For the current experimental arrangement the acceleration of the centreline velocity in the streamwise direction occurs because of flow development and also because of the small change of cross-sectional dimensions, particularly within the first $2a$ of the channel.

The area of critical interest, as far as the curve fit is concerned, is not at the inlet but around the location where the velocity reaches 99% of its fully developed value. Therefore, rather than applying a more complicated function to describe the centreline velocity over the entire entrance region, Equation 4.1 was applied over a restricted portion of the centreline distribution. For the lowest Reynolds number studied, $Re = 1$, the centreline velocity at the inlet was approximately 85% of the fully developed value. In order to be consistent for all Reynolds numbers, Equation 4.1 was fitted to the centreline velocities in a smaller region, defined by the streamwise location where 0.85% of the fully developed value occured, and the furthest distance downstream captured in the measurement plane.

The procedure is demonstrated with the numerical case at $Re = 44$ in Figure 4.12. To determine the location along the centreline where the centreline velocity is 0.85% of its fully developed value, Equation 4.1 was first fit to the entire data set along the centreline of the channel. Based on this fit, the restricted portion on the data set was extracted and Equation 4.1 was fitted a second time, but only to the the restricted data set. The second application of Equation 4.1, seen as the blue curve in Figure 4.12 achieves a much better fit to the numerical data in this range.

The result of the application to the restricted data sets are given in Table 4.2. For the low Reynolds number cases, $Re = 1, 6, 11$, the flow enters with close to 85% of its fully developed range and therefore the curve is fit to almost the same size data set, and little difference is achieved. For the higher Reynolds

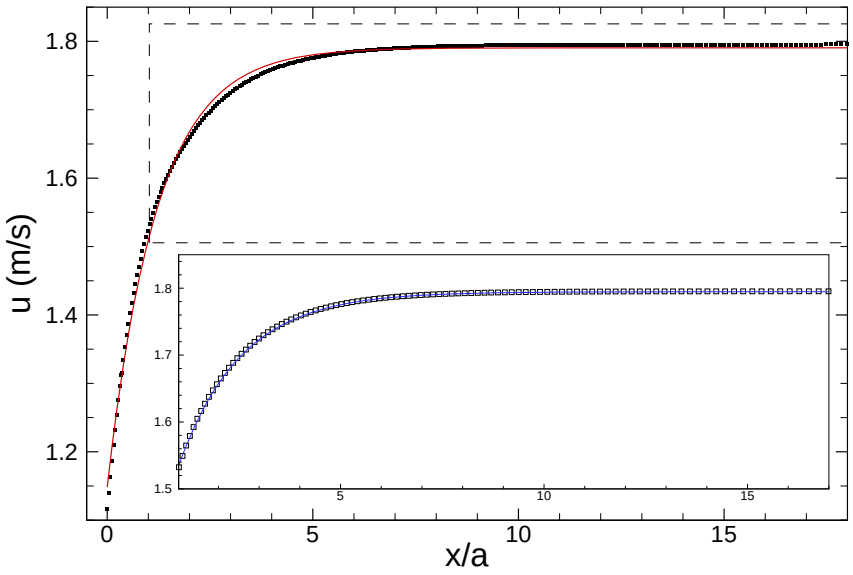

Figure 4.12: The decaying exponential function, Equation 4.1, fit to the numerical centreline velocity distribution for $Re = 44$. Symbols are the numerical result. Solid red line is the curve fit to the entire data set. Blue line is curve fit to the restricted portion of the data set.

Table 4.2: Entrance length calculated using two applications of Equation 4.1 to the numerical data and by inspection.

Re	L_e (μm)		%Difference
	Num curve fit	Inspection	
1	30.9	39.1	-21
6	35.1	42.5	-17
11	43.4	50.0	-13
22	68.3	72.9	-6
33	98.1	101.1	-3
44	129.9	132.9	-2
55	162.1	166.2	-3
66	194.7	200.2	-3

number cases, $22 \leq Re \leq 66$, a marked improvement over the original curve fit can be seen. Using this procedure, the calculation of entrance length was improved and the robustness of the method retained. Unfortunately, the curve fit still systmatically underestimated the actual entrance length, and at low Re this represents a significant bias.

4.4 Entrance Length Comparison

4.4.1 Numerical and Experimental Results

The experimental results presented thus far were extracted from a single measurement set. For each case, each Re in this instance, a measurement of the flowfields was made five separate times in order to improve the accuracy of the result. The entire setup procedure, described earlier in Section 3.3, was performed before each set of measurements to ensure that the errors incurred from positioning were not correlated and could be reduced by an averaging process. The extraction of the centreline velocities, and curve fit procedure were also performed before averaging, so that only the end result, L_e and $u_{cl,fd}$ were averaged as suggested by Coleman & Steele (1999).

Table 4.3: Experimental $u_{cl,fd}$ and L_e calculated from five measurement using Equation 4.1.

Re	$u_{cl,fd}$ (m/s)			L_e (μm)		
	avg	std (10^{-2})	std%	avg	std	std%
1	0.044	0.44	9.9	34	1.7	5.0
6	0.218	0.22	1.0	37	1.8	4.9
11	0.443	0.23	0.6	48	2.1	4.4
22	0.887	1.29	1.5	73	2.3	3.2
33	1.342	1.42	1.1	106	2.7	2.5
44	1.803	0.43	0.2	142	4.7	3.3
55	2.247	1.00	0.4	175	2.6	1.5
66	2.713	0.38	1.4	208	16.7	8.0

The averaged entrance lengths and fully developed centreline velocities calculated for the eight Re cases are given in Table 4.3. In this table, the ratio of

standard deviation to average result is listed as a percentage. With the exception of the lowest Reynolds number case, $Re = 1$, the variation of the fully developed centreline velocity is $\leq 1.5\%$, which is about the same as the bias limit calculated for the flow rate of 1.4% in Section 3.4.3. At $Re = 1$, the standard deviation is about 10% of the mean, which reflects the variability found during experimentation for this slower speed. The variation of the measured entrance length is small, approximately 5% for most cases with $Re = 66$ having the highest standard deviation, 8% of the mean length. For this case the measured entrance length is long and occured at about the limit of the measured plane. Sometimes the length would fall outside the measurement plane, depending on exactly where the entrance region was placed within the field of view of the camera. It is suggested for this reason that the higher variability of the entrance length for $Re = 66$ occured.

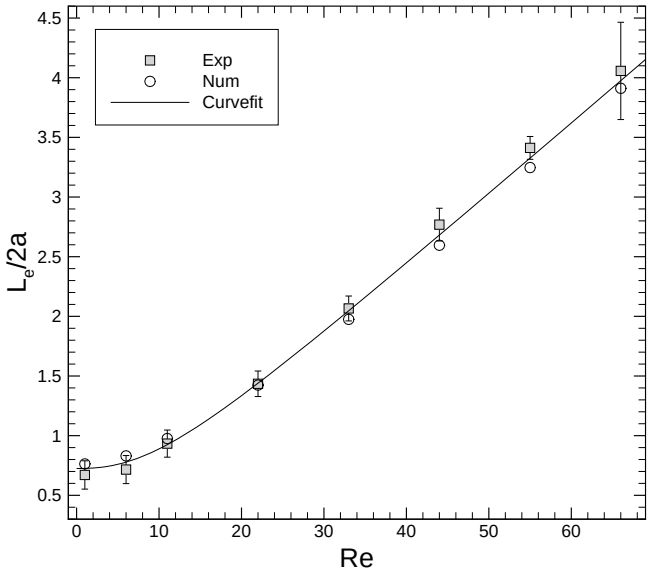

Figure 4.13: Variation of non-dimensional entrance length with Reynolds Number. Solid line is the curve, Equation 4.3 fitted to both numerical and experimental data sets.

The experimentally determined entrance lengths, normalised by the channel width, $2a$, have been plotted against the numerical results determined by inspection in Figure 4.13. Table 4.4 contains corresponding values used in this plot. In Figure 4.13, the entrance length follow a non-linear trend with Reynolds num-

Table 4.4: Non-dimensional entrance length $L_e/2a$.

Re	$L_e/2a$	
	Exp	Num
1	0.67	0.76
5	0.72	0.83
11	0.93	0.98
22	1.43	1.42
33	2.07	1.97
44	2.77	2.60
55	3.41	3.25
66	4.06	3.91

ber as expected for these low Reynolds numbers (Atkinson *et al.* (1969)). The entrance length varied from a constant value, $L_e/2a = 0.7$ as $Re \to 0$, to a near linear trend with Reynolds number at higher Re. The entrance length is not a perfectly linear relation with Reynolds number in the range studied here, which is consistent with other works on steady flow, where $Re > 200$ has been required for linearity (Vrentas *et al.* (1966)).

Overall the agreement between experimental and numerical entrance lengths is reasonably good. At lower Reynolds numbers, $Re \leq 11$ the experimental entrance lengths lie below the numerical result, as would be expected by the curve fit procedure used, which systematically under predicted the entrance length at low Re. At higher Reynolds numbers, the results are slightly larger than the numerical result, and all points lie within 6%. Alongside the results in Figure 4.13, a curve has been fitted to both the experimental and numerical data, of the form

$$L_e/2a = [(C_4)^{C_5} + (C_6 Re)^{C_5}]^{1/C_5} \tag{4.2}$$

where C_4, C_5, C_6 are constants to be determined for specific geometries. Durst *et al.* (2005) used this form to accurately represent numerically calculated entrance lengths over a large range of Reynolds numbers. This equation gives much greater flexibility than the more frequently used form proposed by Chen (1973) and has the right asymptotic behaviour. Here C_4 can be thought of as the creep-

ing flow limit, and C_5 as the high Reynolds number asymptote, C^+. Equation 4.2 fitted to the experimental and numerical results gave the constants as

$$L_e/2a = [(0.725)^{2.4} + (0.060Re)^{2.4}]^{1/2.4} \tag{4.3}$$

and all experimental and numerical points are captured within 8% of this correlation and for $Re \geq 22$ are within 4%.

4.4.2 Experimental Results and Existing Correlations

The experimental result can also be compared with a number of existing correlations. For a planar entry Lee *et al.* (2008) examined flow into two rectangular channels, which had similar aspect ratios of 2.75 but one channel had its longer side in common with the plenum and the other had its shorter side (which was discussed in Section 2.2.4). Lee *et al.* (2008) proposed a correlation for both conditions, of the form suggested by Chen (1973),

$$L_e/D_h = \frac{1.09}{1 + 0.019Re} + 0.026Re \tag{4.4}$$

for the channel with the longer side in common, and

$$L_e/D_h = \frac{0.46}{1 + 0.011Re} + 0.013Re \tag{4.5}$$

for the channel with the shorter side in common.

During the course of this research, Ahmad & Hassan (2010) published an entrance length correlation for square cross-section channels, based on their own experimental work on microchannels flows. The given correlation was

$$L_e/D_h = \frac{0.63}{1 + 0.035Re} + 0.0742Re \tag{4.6}$$

and is of the same form as the two equations above, given by Lee *et al.* (2008). A comparison of the current experimental results and those predicted by Equations 4.4, 4.5, 4.6 is provided in Figure 4.14.

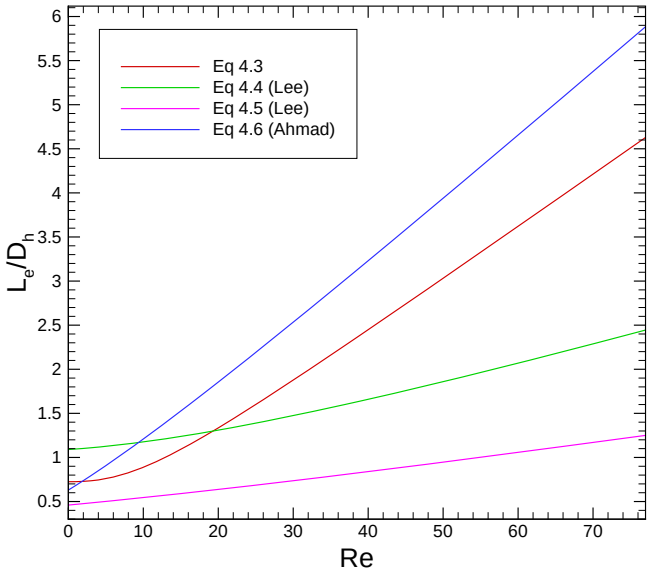

Figure 4.14: Comparison of correlation obtained in this thesis (Equation 4.3) and existing in literature correlations.

For $Re > 20$, the current results for a near square geometry have shorter development lengths than the two results for an aspect ratio 2.75, using the correlations proposed byLee *et al.* (2008). This would be expected as channels with a more slender the cross-sections generally have a faster rate of development. For $Re << 20$, the correlation for the channel with its shorter length in common with the plenum predicts a longer entrance length than the proposed by the other correlations. The reason for this difference it not known, and may be due to the high uncertainties which occurred for all authors at low Re.

The correlation given by Ahmad & Hassan (2010) predicts larger values of $L_e/2a$, about $20 - 30\%$ larger than the correlation based on the experimental results of this work. The decrease in entrance length in the current results could by expected due to the effects of the planar entry, which were not present in the experiments of Ahmad & Hassan (2010). The other reason for the discrepancy, which is thought to be minor, is the slight variation of the cross-sectional geometry from that of perfect square. It should also be pointed out that Equation 4.6, fit the experimental data of Ahmad & Hassan (2010) to within 15%.

The discussion given in this section suggests the results of the current study

are comparable to those results already in the literature. The current results extend both the work of Lee *et al.* (2008), Ahmad & Hassan (2010) to include steady flow into a square cross-section channel for a planar entry condition with some of the most accurate experimental results to date. The comparison of the current results with those of Ahmad & Hassan (2010) for flow in a square channel suggest that the planar entry reduced the entrance length by up to 30%, which is similar to the findings of Lee *et al.* (2008) for a planar entrance, in which reductions of $20 - 80\%$ were found.

Chapter 5

Oscillatory Flow in the Entrance Region

In this chapter the experimental results for oscillatory (zero mean flow) and pulsatile flow (steady component superimposed on an oscillatory component) in the entrance region of the channel are presented. First the features of purely oscillatory flow conditions are described for three Stokes numbers, $\alpha = 1.10, 1.90, 2.45$. Next, the results for pulsatile flow are presented, for $\alpha = 2.45$ and four oscillatory to steady amplitude ratios, A, of 3.70, 1.85, 1.25, 0.93. Finally, a summary is given of the entry flow results for both oscillatory and pulsatile flow conditions.

5.1 Oscillatory Flow (Zero Mean Flow)

In order to generate a purely oscillatory flow, the rotor valve located above the filling port was closed and a sinusoidal voltage was applied to the piezoelectric disc. The closed rotor valve prevented compliance effects of the tubing system upstream of the microfluidic device from effecting the flow within the chip. The applied sinusoidal voltage was converted into a mechanical deflection of the silicon diaphragm by the piezoelectric disc. This motion was transferred to the fluid within the chamber, and carried by the fluid through the microfluidic device. The desired flow within the channel has the form

$$\bar{u} = \bar{u}_{os} sin(\theta) \tag{5.1}$$

where $\bar{u}$ is the cross-sectional average velocity, and θ is the phase angle of the average flow equal to ωt, where ω is the angular frequency of oscillation. The time-averaged velocity over the entire oscillation cycle is equal to zero, so that the representative velocity can be taken as the amplitude of the average flow, $\bar{u}_{os}$. With this velocity scale, the Reynolds number can then be defined

$$Re_{os} = \frac{\bar{u}_{os} 2a}{\nu} \tag{5.2}$$

where a is the channel half width and ν is the kinematic viscosity of the fluid. The other non-dimensional parameter that characterises oscillatory duct flow is the Stokes number

$$\alpha = a\sqrt{\frac{\omega}{\nu}}, \tag{5.3}$$

which is often viewed as a measure of the ratio of unsteady to viscous forces. At a distance far from the either end of a channel, laminar flow under oscillatory conditions becomes fully developed, and its velocity distribution becomes invariant in the streamwise direction for the entire oscillation cycle. In this region, the velocity distributions are a function of the Stokes number, α, only. For oscillatory flows, Drake (1965) was the first to solve the equations of motion for channels with rectangular cross-sections. In order to characterise the flow generated by the actuation of the diaphragm and to establish the accuracy of the microPIV measurements under these flow conditions, the PIV results are first compared in the fully developed region to the analytical solution of Drake (1965) for oscillatory flow in a square channel.

5.1.1 Fully Developed Flow

Three frequencies were studied, $f = 300, 900$ and $1500Hz$ giving to Stokes numbers of 1.10, 1.90 and 2.45 respectively. Measurements equally spaced at 15^o intervals from zero to 180^o, were made in each half cycle of oscillation that had a net flow from the chamber into the channel. This portion of the cycle will be referred to as 'ingestion' and the other half of the cycle as 'expulsion'. The timing of the measurement acquisition was based upon the centreline velocity cycle (described in detail in Section 3.3) but the results are presented in terms of aver-

age flow properties, $\bar{u}_{os}$ and θ. Measured velocity profiles for the three different Stokes number have been presented in Figures 5.1-5.3, acquired in the midplane of the channel. The experimental values were extracted at the furthest distance in the streamwise direction captured in the field of view, $\approx 200\mu m$ from the inlet, which corresponds to approximately four channel widths, or $8a$. The symbols are the experimentally measured velocity, and the solid lines are the analytical solution of Drake (1965).

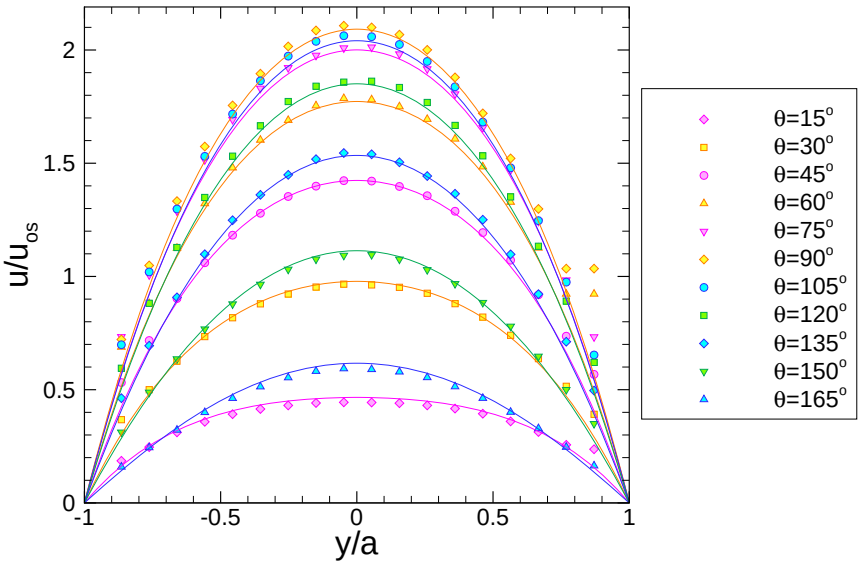

Figure 5.1: Velocity profiles against phase angle θ, for $\alpha = 1.10$. Symbols are the experimental result. Solid lines are the analytical solution of Drake (1965).

For the lowest Stokes number, $\alpha = 1.10$, the comparison can be seen in Figure 5.1. Throughout the oscillation cycle the profiles remain very close to the steady state profile, as expected for low α, and the flow can be said to be quasi-steady. Good agreement between the experimental results and analytical solution has clearly been demonstrated. The velocity profiles for this case however do not appear to be symmetric in time about the peak centreline velocity as expected. This was due to a slight error that was made in the timing calculations prior to measurements being made. The good agreement between the experimental result and analytical solution at all phases, however indicates that the calculated average velocity amplitude, $\bar{u}_{os}$ and phase angle θ used to scale the experimental

results were accurate. Therefore the only bearing the miscalculation has on the actual results presented, is that the phase angle that has the maximum centreline velocity was not captured but missed by 2^o, which is only of minor consequence and thus this experimental case was not redone.

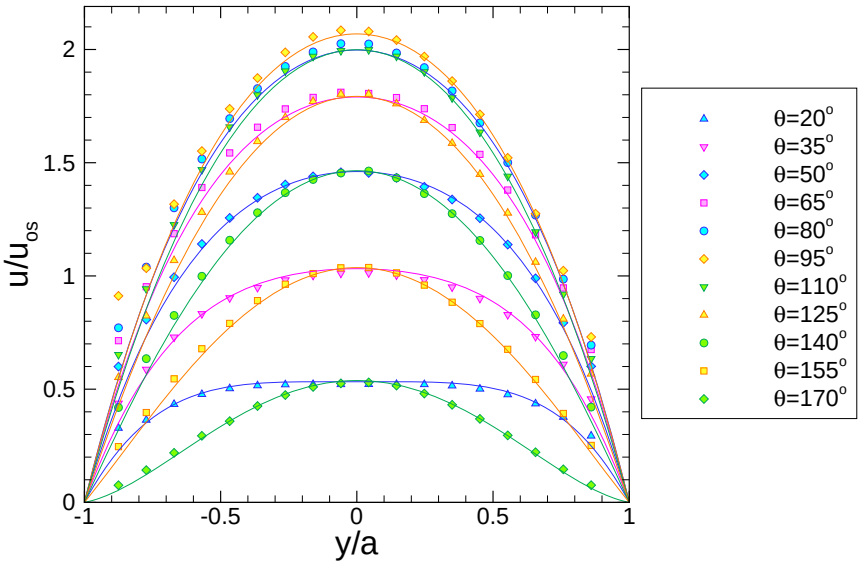

Figure 5.2: Velocity profiles against phase angle θ, for $\alpha = 1.90$. Symbols are the experimental result. Solid lines are the analytical solution of Drake (1965).

For $\alpha = 1.90$, shown in Figure 5.2, the timing scheme was successfully implemented and phases are symmetric about the peak centreline velocity. This can be recognised in the figure, as for each centreline velocity other than the peak, the centreline velocity is captured by two phases either side of the peak. As with $\alpha = 1.10$ good agreement can be see between the experimental profiles and analytical solution at all phases. The increase in Stokes number has caused the velocity profiles to deviate from the steady flow shape and due to the inertia of the fluid the velocity on the centreline lags the main flow. From the analytical solution, for $\alpha = 1.90$ the centreline velocity lags the average flow by 5.4^o. This effect causes the maximum velocity to occur away from the midplane in the early part of the cycle and only the locations where the maximum velocity occurred in the midplane were measured. Therefore, as shown in Figure 5.2 the first profile was measured at $\theta = 20^o$. The velocity distribution at this phase can been seen

to have a broad flat region in the centre of the channel, which the flow retains in the early part of the cycle, $\theta = 0^o - 50^o$. As the flow approached its peak, $\theta = 90^o$, the profiles at $\theta = 65^o - 125^o$ can be seen to be very similar to the steady flow distribution. Later, for $\theta = 140^o - 170^o$, the velocity distributions takes on a much narrower shape and are very different to the accelerating phases.

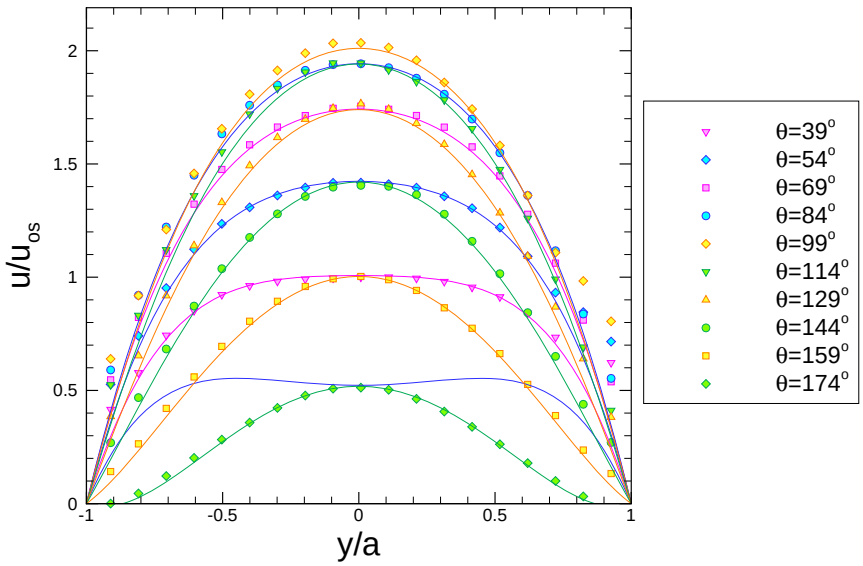

Figure 5.3: Velocity profiles against phase angle θ, for $\alpha = 2.45$. Symbols are the experimental result. Solid lines are the analytical solution of Drake (1965).

The velocity profiles for highest Stokes number $\alpha = 2.45$ have been presented in Figure 5.3. The desired timing scheme has successfully been implemented, and phases are symmetric about the centreline velocities. The first experimental phase was measured at $\theta = 39^o$, as earlier phases have maximum velocities that did not occur on the centreline. This can be seen by the analytical solution plotted for $\theta = 24^o$, the line with no nearby symbols, which has a dip in the centre. The features discussed in the profiles for $\alpha = 1.90$, are more prominent for $\alpha = 2.45$ in Figure 5.3. The profiles early, $\theta = 39^o - 54^o$ are very broad in shape and later, $144^o - 174^o$ narrow. In fact, at $\theta = 174^o$, the profile passes through $u/\bar{u}_{os} = 0$ before the wall and flow reversal has just begun to occur.

Overall very good agreement has been achieved for all three Stokes numbers and at all phases. The flow was also examined across the remaining half of

the cycle, $\theta = 180^o - 360^o$, and a similar level of agreement was achieved. As the flow in the fully developed region is symmetric in time over a half cycle, 'ingestion' is the same as 'expulsion' but with a change of direction, and therefore these phases have not been presented. The results presented in Figures 5.1-5.3, demonstrate that the flow is indeed oscillatory and that the flow reaches a fully developed state within the channel. Furthermore, the timing and accuracy of the PIV measurements have both been confirmed for oscillatory conditions. With this established, the results for the entrance region flow can now be presented. First the flow in chamber is presented, which is much more complex than for the steady flow results presented in Section 4.2. Following this, the developing velocity distribution within the channel is explored.

5.1.2 Flow fields in the Chamber

When the diaphragm oscillates with a simple harmonic motion the flow field in the chamber near the entrance to the channel also oscillates; with the flow changing from being directed towards the channel to the fluid moving away from the chamber. As the flow changes between these two states of ingestion and expulsion, intricate flow structures emerge, grow, propagate and eventually dissipate. The rich fields that can exist for oscillatory flow outside of a channel were also reported in the numerical study of Jaworski *et al.* (2009). For all oscillatory cases studied the flow in the chamber followed the same basic pattern, and only a single illustrative case will be presented.

Instantaneous streamlines of the chamber flow field captured on the midplane have been plotted in Figure 5.4 at various phase angles for $\alpha = 1.90$ and $Re \approx 30$. Starting with the flow at $\theta = 215^o$, shortly after the fluid begins to flow into the chamber, as shown in Figure 5.4(a), the flow field fans out smoothly from the channel into the chamber. As the average velocity out of the channel increases, flow separation occurs on the surface of the two chamber walls outside of the channel. As may be seen in Figure 5.4(b), at $\theta = 335^o$ two vortices are formed, one on either side of the channel, with a jet of fluid in between at $\theta = 335^o$. The flow pattern here is reminiscent of the flow fields that are generated by another oscillatory device, the synthetic jet (Smith & Glezer (1998) and Glezer & Amitay (2002)).

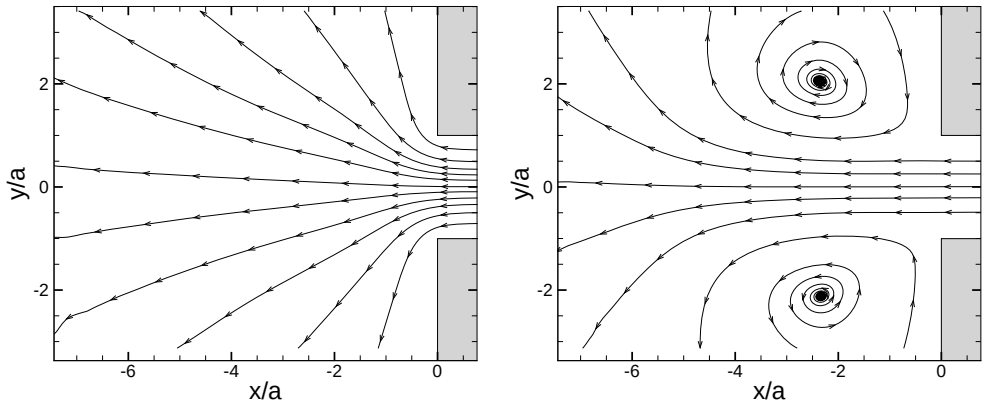

(a) $\theta = 215^o$ (b) $\theta = 335^o$

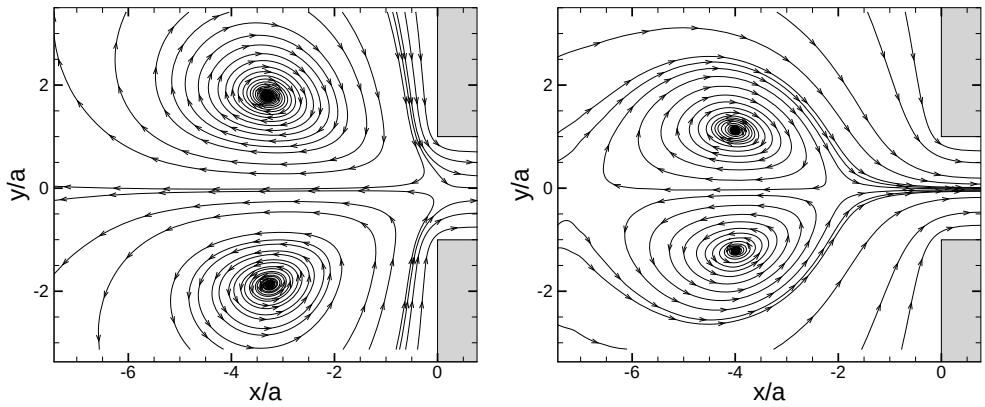

(c) $\theta = 5^o$ (d) $\theta = 35^o$

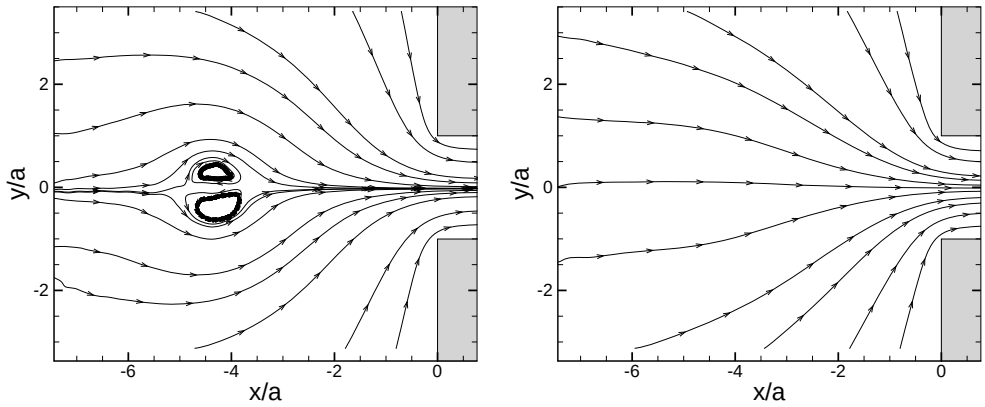

(e) $\theta = 50^o$ (f) $\theta = 80^o$

Figure 5.4: Streamlines of the flow in the chamber at various phase angle θ for $\alpha = 1.90$.

A short time later at $\theta = 5^o$, the direction of flow has changed and as may be seen in Figure 5.4(c) the fluid now leaves the chamber to flow back into the channel. In the intervening period the vortices in Figure 5.4(b) continue to rotate in the same direction, have grown and have moved further from the channel entry, but not moved much in the direction perpendicular to the flow. However, in order to enter the channel, the fluid now has to flow around the vortices.

Surprisingly, as is seen in Figure 5.4(d), continue to move away from the channel despite the fact that the fluid is flowing into the channel. Later, due to viscous action the strength of the vortices diminishes so that they

shrink and exist as island surrounded by the main flow as shown in Figure 5.4(d) at $\theta = 50^o$. Within this island, the velocity magnitudes are small and highly varying in direction. Because of this the PIV measurements shown in this figure were unable to resolve the fine details of the flow within this region. Finally, as may be seen in Figure 5.4(f), the main flow has completely engulfed the island and its presence can no longer be detected. The formation of a sustained jet over the entire oscillation cycle, therefore did not occur. The flow then proceeds smoothly into the channel in much the same way as for steady flow and remains in this way until the flow direction is reversed and the cycle depicted in Figure 5.4 is repeated.

5.1.3 Developing Flow Fields in the Channel

Flow development from the flow fields in the chamber, presented in the previous section, to the fully developed profiles presented in 5.1.1 can be analysed much like steady flows but on a phase by phase basis. The developing velocity profiles can be seen in Figure 5.5 for the highest Stokes number, $\alpha = 2.45$, at three different phase angles, which represented the more extreme shapes seen in the velocity profiles in the fully developed region (in Section 5.1.1). The fully developed profiles do not depend on the Reynolds number, but the flow in the developing region is expected to be. The results presented here are for $Re_{os} = 30$.

The development of flow for $\alpha = 2.45$ at $\theta = 39^o$, which was the phase angle with the broadest profile measured, and can be seen in Figure 5.5(a). The profile enters at $x/a = 0$ with a profile highly similar to its fully developed shape. Subsequently, the distance required for the flow to reach a fully developed state

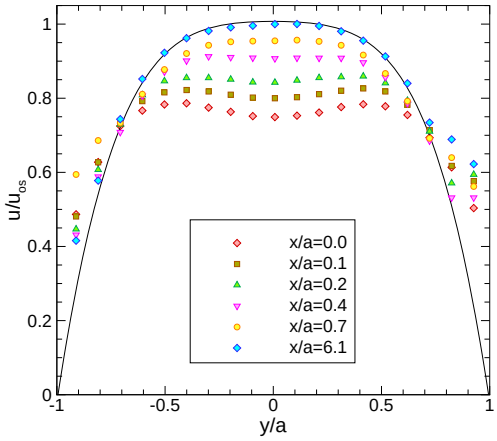

(a) $\theta = 39^o$

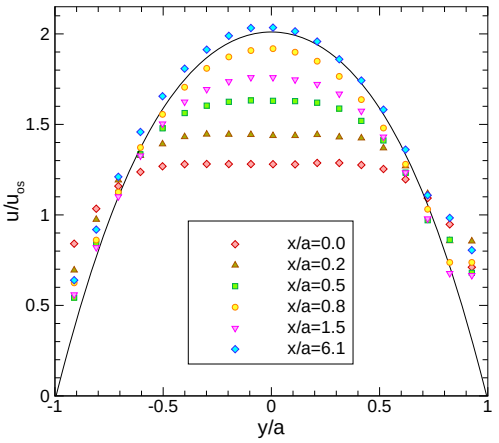

(b) $\theta = 99^o$

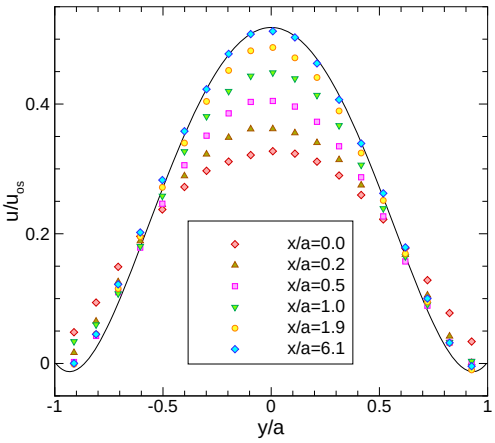

(c) $\theta = 174^o$

Figure 5.5: Developing velocity profiles at three phase angles for $\alpha = 2.45$. Profiles at various streamwise locations and $z/a = 0$. Symbols experimental values. Solid lines are the analytical solution of Drake (1965).

was particularly short for this phase angle. Interesting the PIV measurements show two off centre maxima in the profiles at $x/a = 0$ through to $x/a = 0.4$, with a slight inflection occurring in the centre. Closer to the wall, the fully developed profile shown by the analytical solution has very steep velocity gradients, which again was not able to be resolved by the current PIV setup.

In Figure 5.5(b), the developing flow at $\theta = 99^o$ can be seen. It was the phase angle where the maximum centreline velocity occurred within the oscillation cycle. At this phase the velocity distribution is very similar to the steady flow profile

and the flow also appears to develop similarly to the steady case. At the inlet, $x/a = 0$, the velocity profile has a flat distribution across the centre region, which slowly becomes rounder for the profiles further downstream. Eventually the flow reaches a fully developed distribution, over a distance substantially larger than for $\theta = 39^o$.

The final phase shown, $\theta = 174^o$ in Figure 5.5(c), was for a highly narrow velocity distribution and where flow reversal had just stated to occur near the wall. The average velocity in this case is much lower than at $\theta = 99^o$, only about 11% of it, yet the flow took a much longer distance to approach the fully developed profile. After this phase angle, 174^o there is a change in direction of the flow and over $\theta = 180^o - 360^o$ there is a net flow out of the channel and into the chamber. This portion of the oscillation cycle, 'expulsion', was also examined and the flow at these phase angles remained very close to the fully developed profiles throughout the entire entrance region.

During ingestion, $0^o < \theta < 180^o$, for same Stokes number, $\alpha = 2.45$, the development of the centreline velocity at various different phase angles can be seen in Figure 5.6. At each phase angle, θ, the centreline velocity for each case was extracted and processed in an identical manner to the steady flow cases presented in Section 4.3, using the curvefit, Equation 4.3. In Figure 5.6 the symbols are the experimental results, and the solid lines are the curvefit, which can be seen to fit the data well at all phases. The velocities have been normalised by the amplitude of the fully developed centreline velocity so that all values are ≤ 1.

In Figure 5.6, for phase angles either side of maximum centreline velocity which share the same centreline velocity, for example, $\theta = 39^o$ and $\theta = 159^o$, the flow can be seen to develop over quite a different length. As seen in the developing profiles in Figure 5.5, during the accelerating stages of the cycle, $0^o < \theta < 90^o$, the flow develops much quicker than during the decceleration phases, $90^o < \theta < 180^o$. This indicates that it is not just the magnitude of the centreline velocity which determines the entrance length of the flow.

The curves fitted to the velocity along the centreline shown in Figure 5.6, were used to determine the fully developed centreline velocity and the entrance length for each phase angle, θ. As discussed in the literature survey in Section 2.3.3, in oscillatory flows the development process is a function of the Reynolds number

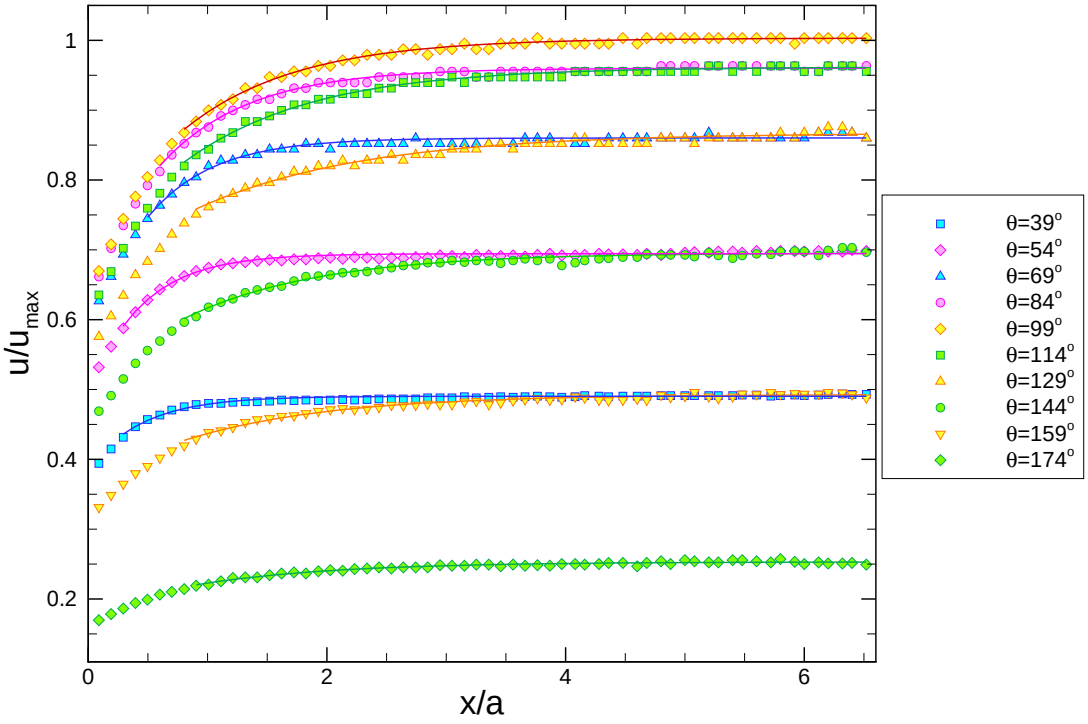

Figure 5.6: Developing centreline velocity at different phase angles, θ. $\alpha = 2.45$ and $Re_{os} = 30$. Symbols are experimental values. Solid lines are the curvefit.

and the Stokes number. The developing velocity fields presented in this section were for $Re = 30$, and $\alpha = 2.45$, and highlighted the effects seen in at all flow conditions in this study. For varying Reynolds and Stokes numbers, the entrance length has been examined, and is presented in the following two sections.

5.1.4 Entrance Lengths for Varying Stokes Number

For three Stokes numbers, $\alpha = 1.0, 1.90, 2.45$, the variation of entrance length with phase angle, θ, is examined. The results given in this section are averaged results, from five sets of measurements, as was done with the steady flow measurement. The flow was studied at nominally the same Reynolds number for the three α studied in this section of $Re \approx 30$.

For the lowest Stokes number, $\alpha = 1.10$, the measured entrance lengths (symbols) are shown in Figure 5.7 against phase angle, θ. The Reynolds number based

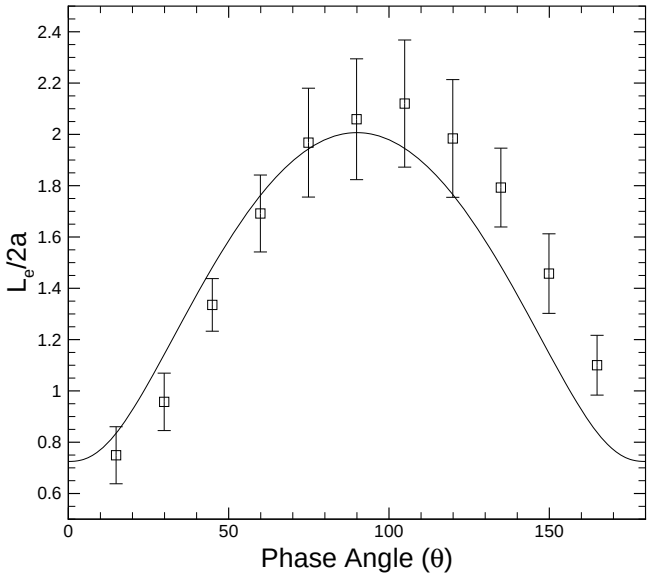

Figure 5.7: Non-dimensional entrance length against phase angle, θ, for $\alpha = 1.10$ and $Re_{os} = 32$. Symbols are the experimental result. Solid line corresponds to Equation 4.3.

on the amplitude of the cross-sectional average velocity, $\bar{u}_{os}$, was determined to be $Re_{os} = 32$, using the method outlined in Section 3.3.2, based on the centreline velocities and the analytical solution. The solid line corresponds to the entrance length correlation, Equation 4.3, derived from the experimental results under steady flow conditions in Chapter 4. In this correlation, the non-dimensional entrance length, $L_e/2a$ has been determined using a Reynolds number calculated from the instantaneous cross-sectional average velocity, $\bar{u}$, described by $\bar{u}_{os}sin(\theta)$.

In Figure 5.7 it can be seen that the experimental entrance lengths lie close to the prediction of the steady flow correlation, and therefore can be said to vary in an approximately quasi-steady manner across the oscillation cycle. For low Stokes numbers, $\alpha \leq 1$, the variation of velocity profiles in the fully developed region is quasi-steady (see the velocity profiles for $\alpha = 1.1$ presented earlier in Figure 5.1), which has lead other workers to suggest that the entrance length for these conditions would also be quasi-steady (Kassianides & Gerrard (1975)). The results shown in Figure 5.7, for $\alpha = 1.1$, provide some experimental support for this assertion.

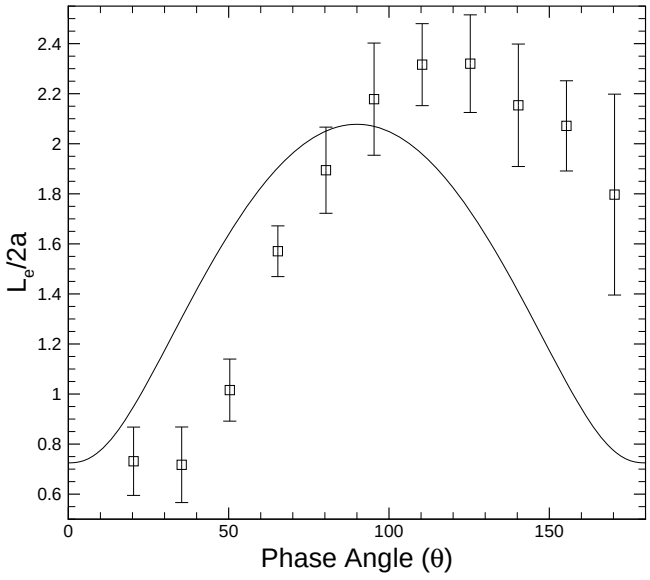

Figure 5.8: Non-dimensional entrance length against phase angle, θ, for $\alpha = 1.90$ and $Re_{os} = 33$.Symbols are the experimental result. Solid line corresponds to Equation 4.3.

For larger Stokes numbers, the fully developed velocity profiles deviated from the steady distribution, (see Figures 5.2 and 5.3 for $\alpha = 1.90$ and $\alpha = 2.45$). At $\alpha = 1.90$, the entrance length deviates from a quasi-steady relation with phase angle, as shown in Figure 5.2, and takes on an S-shaped distribution. Early in the cycle, $\theta < 50^o$, the flow develops quickly and is approximately equal to the lower limit, $L_e/2a = 0.72$, given by the steady flow correlation. For $0^o < \theta < 90^o$, the entrance lengths are shorter than the predicted values of the steady flow correlation and around the peak values of $\bar{u}$, the experimental results lie within experimental error of the correlation. After peak flow, at $\theta \approx 120^o$, the maximum entrance length occurs. This maximum entrance length is approximately 12% greater than maximum predicted by the steady flow correlation. As the flow decelerates further, $130 < \theta < 180$, the entrance length decreases with phase angle, but takes a longer distance to develop than the given by the steady flow solution.

The entrance lengths for the highest Stokes number studied, $\alpha = 2.45$, given in Figure 5.3, show a variation with phase angle, θ, completely different from

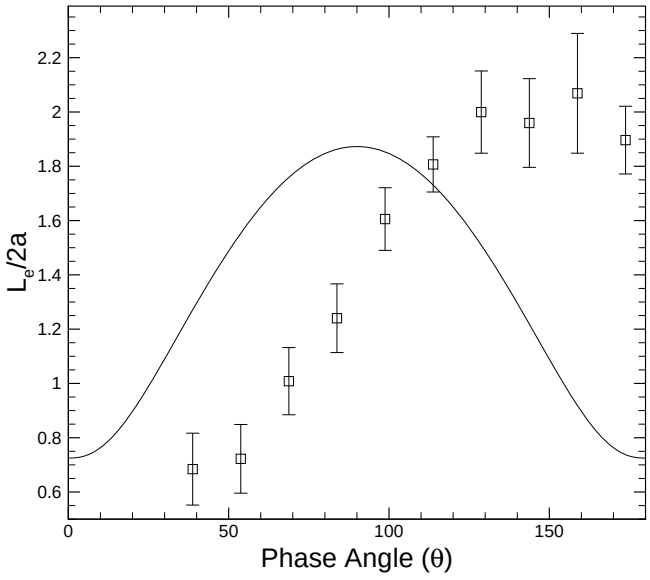

Figure 5.9: Non-dimensional entrance length against phase angle, θ, for $\alpha = 2.45$ and $Re_{os} = 30$. Symbols are the experimental result. Solid line corresponds to Equation 4.3.

the quasi-steady curve. The distribution with phase angle now becomes more like a Z-shape, which begins at approximately the lower limit, $L_e/2a = 0.72$, for $\theta < 50^o$. The entrance length increases with phase angle and reaches the maximum entrance length at $\theta \approx 120^o$, and then oscillates about this value for the remainder of the half cycle. The variation of the data after $\theta = 120^o$ is within experimental error meaning its value is essentially constant at the end of the cycle. This maximum value is slightly greater than the maximum predicted by the steady flow correlation, approximately 10% longer. A similar distribution to that shown in Figure 5.9 was found in the numerical results of Raju *et al.* (2005) for flow between parallel plates. This can be seen in a replot of the results of Raju *et al.* (2005) given earlier, in Figure 2.9(a), for a Stokes number of 2.5.

In Figure 5.10 a comparison is made between the entrance lengths of the three Stokes numbers. The Reynolds number for each of the three cases was not the same, and to help facilitate a comparison, the entrance length has been divided by Re. This allows the effects of the Stokes number to more clearly be distinguished. For $\alpha \leq 2.45$, the Stokes number has a large effect on the variation on entrance

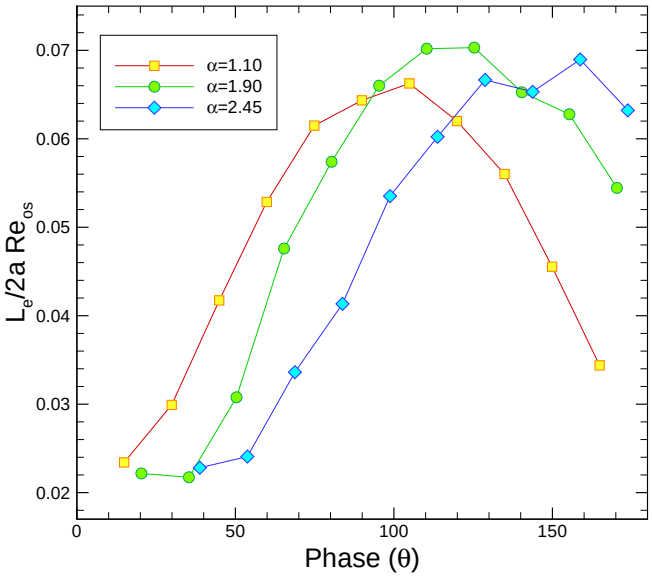

Figure 5.10: Entrance length non-dimensionalised by Re_{os} against phase angle, θ, for $\alpha = 1.10, 1.90, 2.45$.

length with phase angle, θ. For increasing α the maximum entrance length occurs later in the cycle, an effect which has been reported in the numerical studies of pulsatile flow (Krijger *et al.* (1991) and He & Ku (1994)). The maximum entrance length however, appears to be approximately the same for all cases, with a slightly higher value for $\alpha = 1.90$. In Figures 5.7-5.9, the maximum value of L_e at each Stokes number was very close to the maximum predicted by the steady flow correlation. A more close examination of the maximum entrance length is given in Section 5.1.6.

The cases presented in this section were for a single Reynolds number, $Re_{os} \approx 30$, which allow the effects of the variation of Stokes number to be investigated. For steady flow, the relationship between entrance length and Reynolds number is non-linear at low Re. No entrance length data exists for oscillatory flows at low Re in the literature, numerical or experimental, and the effect is now explored.

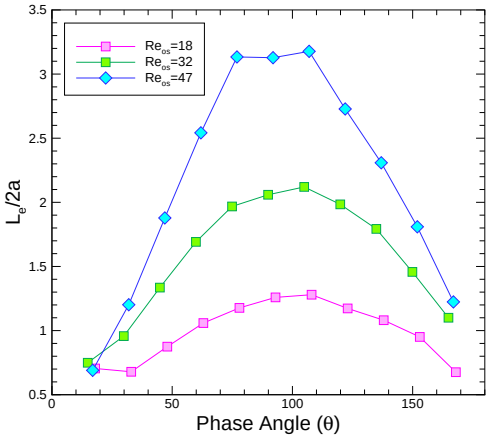

(a) $\alpha = 1.10$

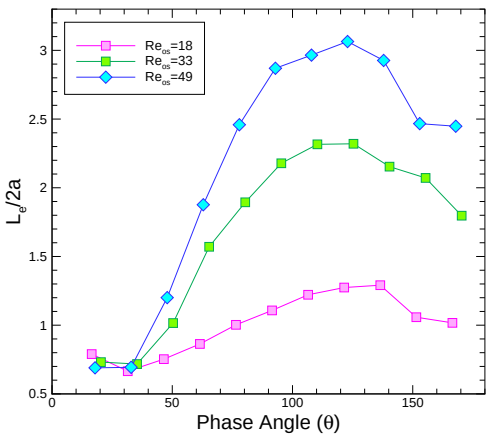

(b) $\alpha = 1.90$

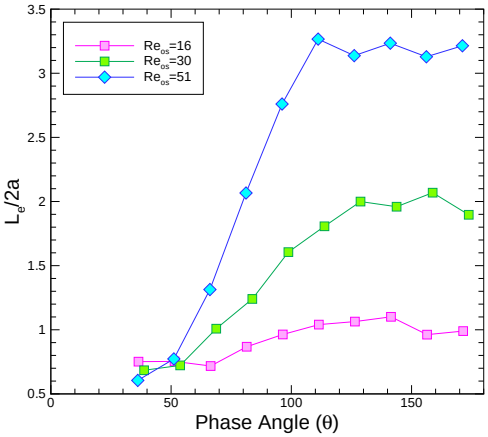

(c) $\alpha = 2.45$

Figure 5.11: Entrance length against phase angle, θ, for varying Reynolds number.

5.1.5 Entrance Lengths for Varying Reynolds number

For each of the three Stokes number examined, $\alpha = 1.0, 1.90, 2.45$ two addition Reynolds numbers cases was performed, one at a higher Reynolds number and one at lower Reynolds number. The upper bound was set to approximately match the maximum steady flow Reynolds number, which is where the entrance length became approximately equal to the length of the measurement field of view. This upper limit also closely coincides with the shortest possible interframing time of the camera. At lower Re, the entrance lengths do not vary significantly about the lower limit of $L_e/2a$ of approximately 0.7, making it hard to discern possible

trends for further reductions in Re. Therefore the range of results presented here represents the full range of Re possible with the current experimental setup.

The results for the new Reynolds numbers, plotted with the original results can be seen in Figure 5.11. The new results are from a single experimental run, unlike the moderate Reynolds number cases of the previous section, which were the average of 5 experimental runs. In each of the three figures presented, the curves follow the same basic trends described in the previous section. For a fixed Stokes number, the entrance length, L_e can be seen to increase with the Reynolds number, Re. Excluding the initial portion of the cycle, $0^o < \theta < 60^o$, the relationship appears to scale approximately linearly for the range of Re examined. This finding is similar to the pulsating studies cited earlier, such as Krijger *et al.* (1991) and the oscillatory results of Raju *et al.* (2005), who both examined higher Reynolds numbers, $Re > 75$, and found the relationship to be linear. To examine the scaling of entrance length scales can be described by steady flow, the maximum entrance length can be compared to the steady flow correlation.

5.1.6 Maximum Entrance Length

For all the cases presented in the previous section, a maximum value of the entrance length was extracted and can be seen in Figure 5.12. In all cases the maximum entrance length occurred after peak flow, and fell within the phase angle range, $105 < \theta < 160$. The experimental results have been plotted against the steady flow correlation using a Reynolds number based on amplitude $\bar{u_{os}}$, which is the solid line in the figure.

All of the nine experimental cases performed lie very close to the steady flow correlation. For $Re_{os} > 20$, the entrance lengths lie above the steady flow correlation. The experimental results for the steady flow cases also lied above the correlation for higher Reynolds numbers, $Re \geq 33$. Overall the steady correlation predicts the maximum entrance length within 12%. Therefore, for the range of Stokes numbers studied here, $\alpha < 2.45$, it can be concluded that the maximum entrance length for oscillatory flow, with a time mean velocity equal to zero, is well predicted by the steady flow correlation when the average velocity amplitude $\bar{u_{os}}$ is used in the Reynolds number.

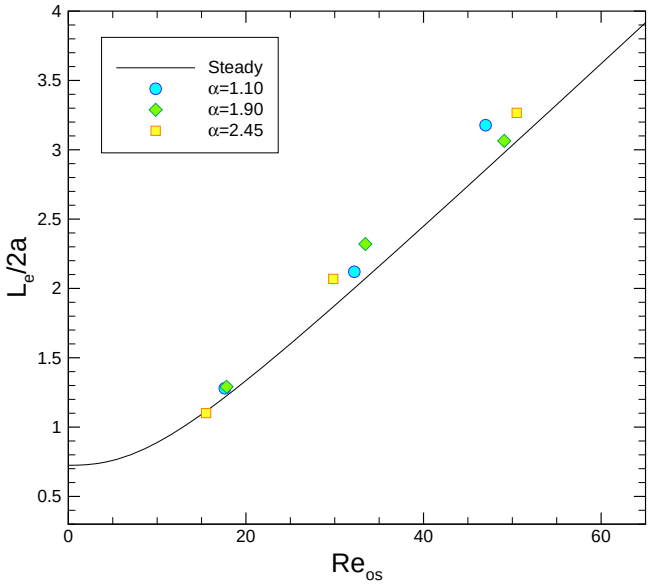

Figure 5.12: Maximum L_e against Re_{os}. Symbols are experimental values. Solid line corresponds to the steady flow correlation, Equation 4.3.

5.2 Pulsatile Flow

Pulsatile flow was composed of steady flow supplied by the syringe, and an oscillatory component generated by the motion of the diaphragm. The rotor valve located above the filling port is kept open and the entire flow system (depicted in Section 3.1.5) can affect the flow inside the entrance region. The desired form of flow from these two components in the channel is described by

$$\bar{u} = \bar{u}_s(1 + Asin(\theta)) \tag{5.4}$$

where again $\bar{u}$ is the cross-sectional average velocity, $\bar{u}_s$ is the steady component of the flow, A is the ratio of the amplitude of oscillatory to steady flow, $\bar{u}_s/\bar{u}_{os}$ and θ is the phase angle of the oscillating component of the average flow. The time averaged velocity over the entire oscillation cycle is equal to the steady component $\bar{u}_s$, and the peak flow is represented by

$$\bar{u}_{puls} = \bar{u}_s + \bar{u}_{os}, \tag{5.5}$$

equal to the sum of the steady and oscillatory components. If this is taken as representative velocity scale the Reynolds number can then be defined

$$Re_{puls} = \frac{\bar{u}_{puls} 2a}{\nu} \tag{5.6}$$

and is the Reynolds number at peak flow. Similarly the analytical solution for fully developed pulsatile flow of the form of Equation 5.4 is the summation of the steady and oscillatory fully developed analytical solutions. For example, the superposition of the steady flow solution of White (1991) and the oscillatory solution of Drake (1965) for a square channel. In order to characterise the flow generated by combination of steady and the oscillatory flow, and evaluate any possible compliance effects from the upstream tubing line, the velocity fields are first compared in the fully developed region to the analytical result.

5.2.1 Fully Developed Flow

The largest frequency, $f = 1500Hz$ or Stokes number, $\alpha = 2.45$, where the flow deviated the most from the steady flow profiles was used to examine the effects of including a steady component. The oscillatory component, $\bar{u}_{os}$ was fixed to give $Re_{os} \approx 30$, approximately the same magnitude of the oscillating component as for the purely oscillatory case with $\alpha = 2.45$ previously examined. The steady flow component, $\bar{u}_s$, which could be controlled much more accurately was increased to give different values of the oscillatory to steady flow ratio, A. Unlike purely oscillatory flow, the flow does not exhibit symmetry in half cycles, and therefore measurements were made over the entire oscillation cycle, in equal increments of 15^o. Measured velocity profiles for four different values of $A = 3.70, 1.85, 1.25, 0.93$, the ratio of steady to oscillatory components, have been presented in Figures 5.13-5.16, acquired in the midplane of the channel.

As a large number of phase angles were measured across the oscillation cycle the profiles have been split into two sub-figures. For example, for in Figure 5.13 the smallest steady component relative to the oscillatory component, $A = 3.70$, the profiles have been presented in Figure 5.13(a) for phase angles $\theta = 294^o - 99^o$, where the flow progresses from the phase angle just after peak expulsion to peak ingestion. In Figure 5.13(b) are the phase angles $\theta = 114^o - 279^o$, where the flow changes from the phase angle just after peak ingestion to peak

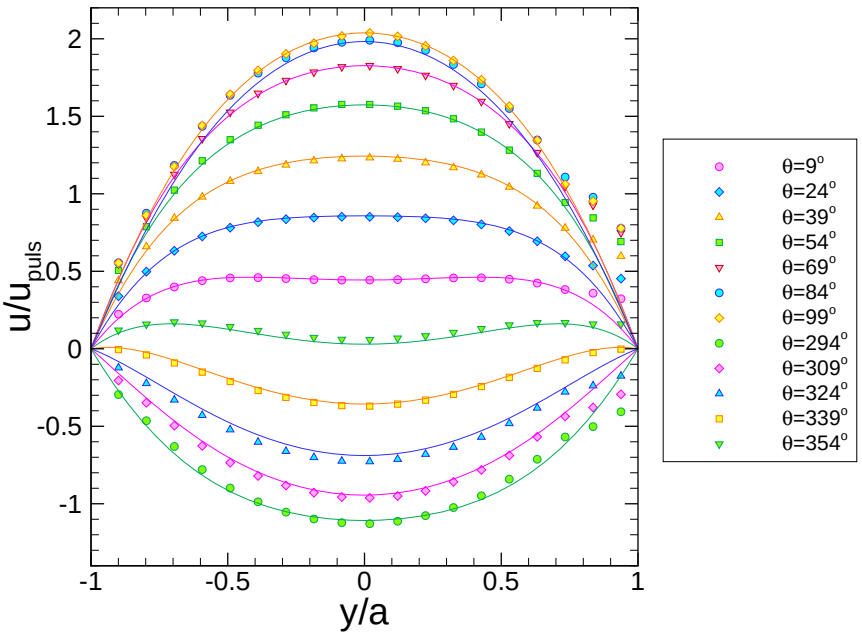

(a) $\theta = 294^o - 99^o$

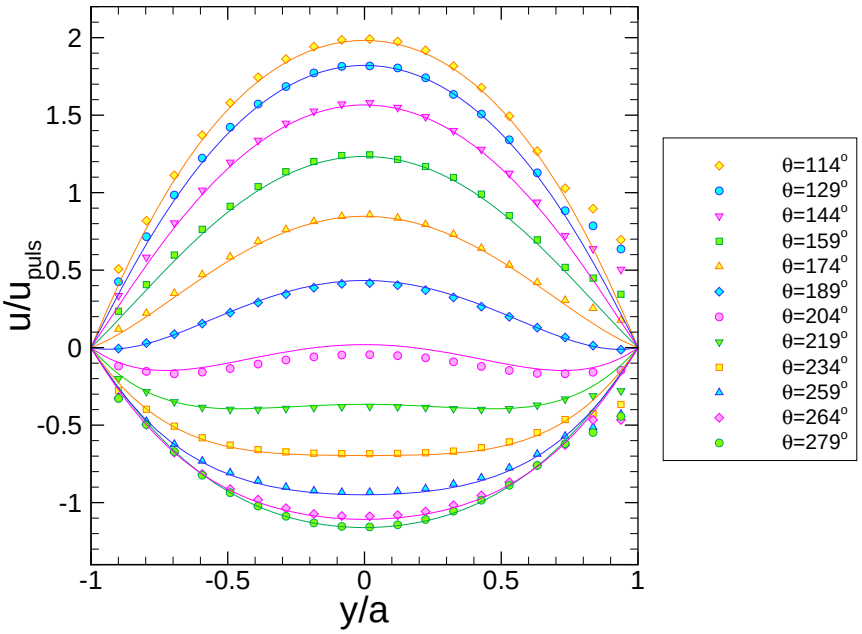

(b) $\theta = 114^o - 279^o$

Figure 5.13: Fully developed velocity profiles against phase angle θ, for $\alpha = 2.45$ and $A = 3.70$. Symbols are the experimental result. Solid lines are the analytical solution of Drake (1965) and White (1991).

expulsion. The experimental values were extracted at the furthest distance in the streamwise direction captured in the field of view, $\approx 200\mu m$ from the inlet, which corresponds to approximately four channel widths, or $8a$. The symbols are the experimentally measured velocity, and the solid lines are the combined analytical solution of Drake (1965) and White (1991). The velocity has been normalised by the amplitude of the cross-sectional average flow, $\bar{u}_{puls} = \bar{u}_s + \bar{u}_{os}$. In Figure 5.13, the steady component of the flow, $\bar{u}_s$, is small, and only has a weak affect on the flow and the profiles during ingestion, $\theta \approx 0^o - 180^o$, are similar to those presented for purely oscillatory flow at $\alpha = 2.45$ in Figure 5.3.

Increasing the steady component relative to the oscillatory, increasing A, the fraction of the cycle where the average flow is reversed is reduced. This can be seen in Figure 5.14, for $A = 1.85$, where only at 8 of the 24 phases angles is the average flow in the direction from the channel back into the chamber. The amplitude of the flow in the reversed direction is also reduced, and in Figure 5.14, the centreline velocity is approximately 60% of $\bar{u}_{puls}$ in the negative direction but in the positive direction remains about 200% of $\bar{u}_{puls}$. The phase lag of the flow in the central region of the channel can still be seen at a number of phases in the oscillation cycle for $A = 1.85$.

In Figure 5.15, the fully developed velocity profiles for $A = 1.25$ can be seen. The steady and oscillatory components are almost equal in magnitude and the phase lag of the central region can barely be distinguished. The flow is now almost exclusively in the positive direction, from the chamber into the channel.

For a largest relative steady component, $A = 0.93$, the profiles have been presented in Figure 5.16. The steady component of the flow is marginally greater than the oscillatory, and there is no reversal of the flow direction. The velocity profiles in Figure 5.16(a) and Figure 5.16(b) show less variation in magnitude and distribution between phase angles. The profiles now resemble the almost parabolic fully developed steady distribution, much more so than for higher values of A.

Overall, in Figures 5.13-5.16, good agreement between the experimental results and analytical solution has been demonstrated. The resultant flow in the channel formed from the combination of steady flow from the syringe pump, and oscillatory motion of the diaphragm has been shown to be of the desired pulsatile form. For low relative steady flow components the velocity profiles were very similar to the purely oscillatory case with $\alpha = 2.45$, and become closer to the

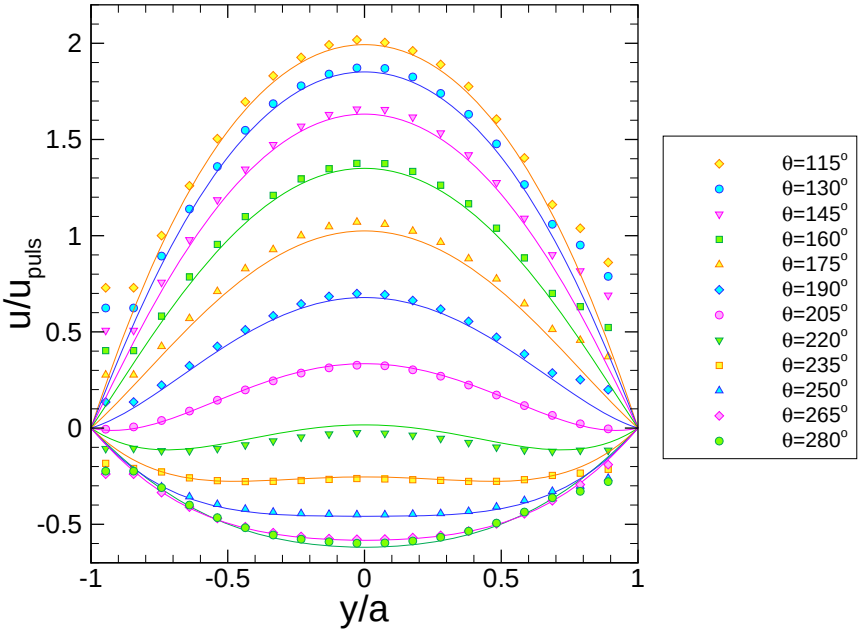

(a) $\theta = 295^o - 100^o$

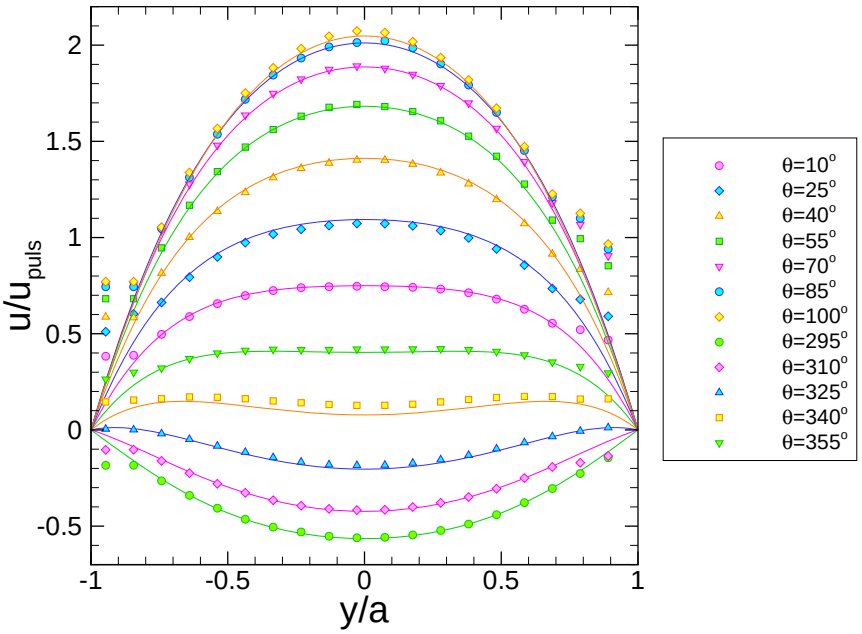

(b) $\theta = 115^o - 280^o$

Figure 5.14: Fully developed velocity profiles against phase angle θ, for $\alpha = 2.45$ and $A = 1.85$. Symbols are the experimental result. Solid lines are the analytical solution of Drake (1965) and White (1991).

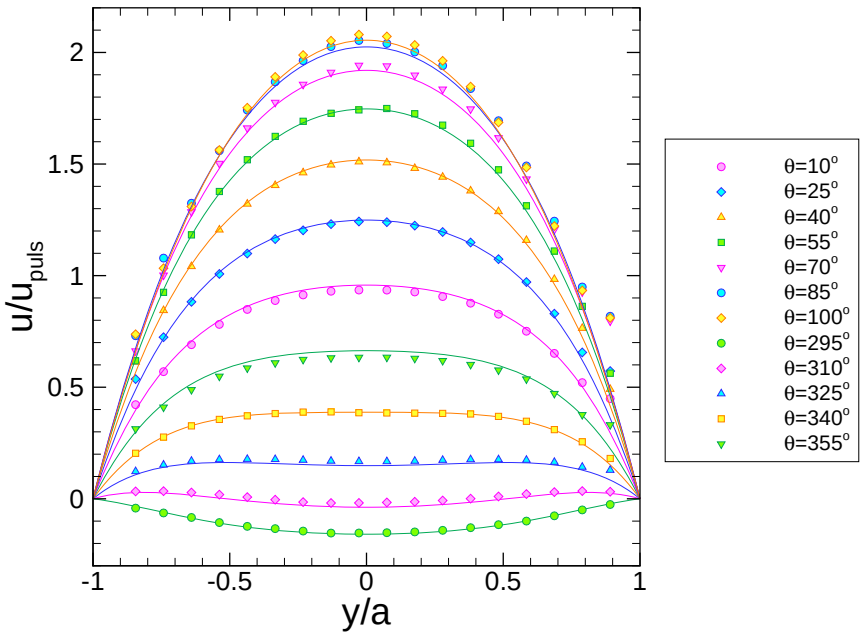

(a) $\theta = 295^o - 100^o$

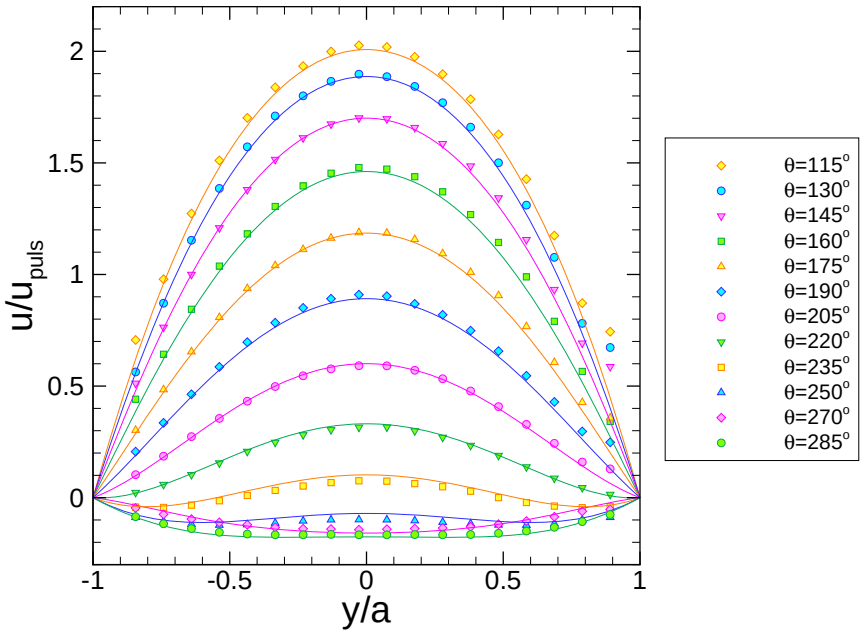

(b) $\theta = 115^o - 280^o$

Figure 5.15: Fully developed velocity profiles against phase angle θ, for $\alpha = 2.45$ and $A = 1.25$. Symbols are the experimental result. Solid lines are the analytical solution of Drake (1965) and White (1991).

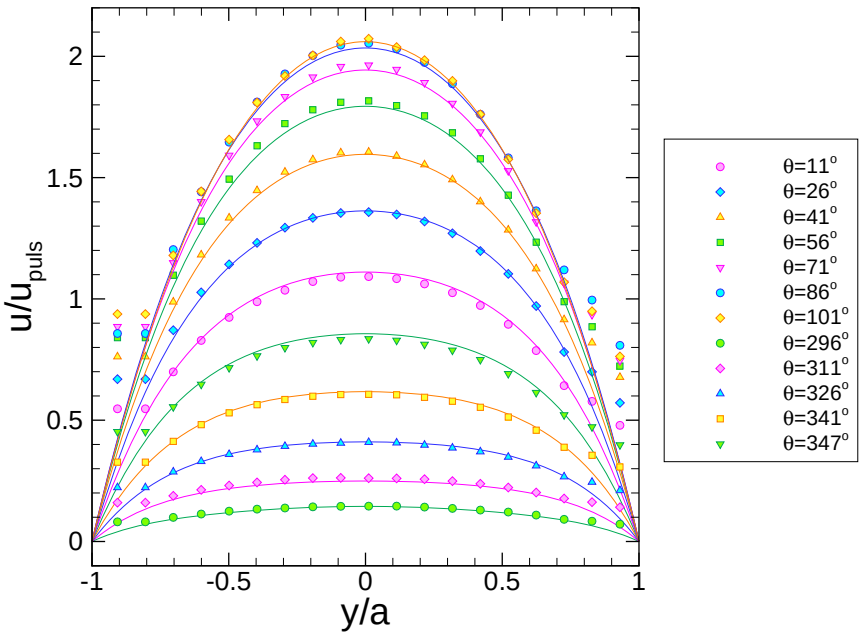

(a) $\theta = 296^o - 101^o$

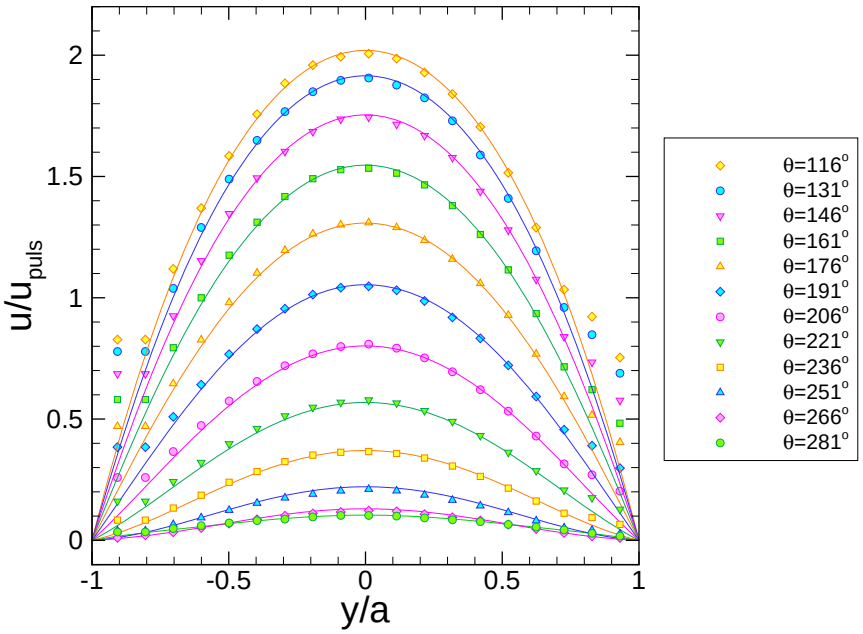

(b) $\theta = 116^o - 281^o$

Figure 5.16: Fully developed velocity profiles against phase angle θ, for $\alpha = 2.45$ and $A = 0.93$. Symbols are the experimental result. Solid lines are the analytical solution of Drake (1965) and White (1991).

fully developed steady flow profile with a decrease in A. The developing profiles have been presented for steady flow in Section 4.2.1, and for the extreme profiles found in the oscillatory case, $\alpha = 2.45$, in Section 5.1.3. The velocity profiles shown in the pulsatile flow cases, Figures 5.13-5.16, showed no features significantly different from those already presented, and this was also the case in the developing region. Therefore the discussion will continue straight onto the measured entrance lengths for each case of oscillatory to steady flow ratio, A.

5.2.2 Entrance Lengths for Varying Steady Flow

The variation of entrance length across the oscillation cycle has been calculated for each case of A examined and can be seen in Figures 5.17 - 5.20. As with the purely oscillatory flow, only those phase angle were the maximum velocity occurred on the centreline, and was in the positive direction, that is, from the chamber into the channel, were the entrance length measured. In each of the Figures 5.17 - 5.20, the experimental results are the symbols, the solid line is the steady flow correlation, Equation 4.3, where Re is the instantaneous Reynolds number based on $\bar{u}$, and the dashed line is the same correlation but based on Re_s, the steady flow component.

In Figure 5.17 flow with the smallest steady component, $A = 3.70$, the entrance length varies with phase angle much like the purely oscillatory case with the same Stokes number, which was described as Z-shaped (shown in Figure 5.9). The entrance length at $\theta < 50^o$ is approximately equal to the steady flow correlation based on the mean Reynolds number. For phase angles $50^o < \theta < 140^o$ the entrance length increases substantially with phase angle, and reaches a maximum at $\theta = 144^o$. From this phase angle there is a reduction in the entrance length, which is different to the purely oscillatory case, which remained an approximately constant length over the later phases angles, $130^o < \theta < 180^o$.

The range of phase angles which were measured increased with increasing A, as the maximum velocity occurs on the centreline was an increasing amount of the oscillation cycle. In Figure 5.18, for $A = 1.85$ the range of measured phase angles has been extended to $-15^o < \theta < 195^o$. Interestingly, in Figure 5.18 for phase angles, $\theta < 50^o$, the entrance length is well below the mean value shown by the dashed line, but for these phase angles the average flow is greater than

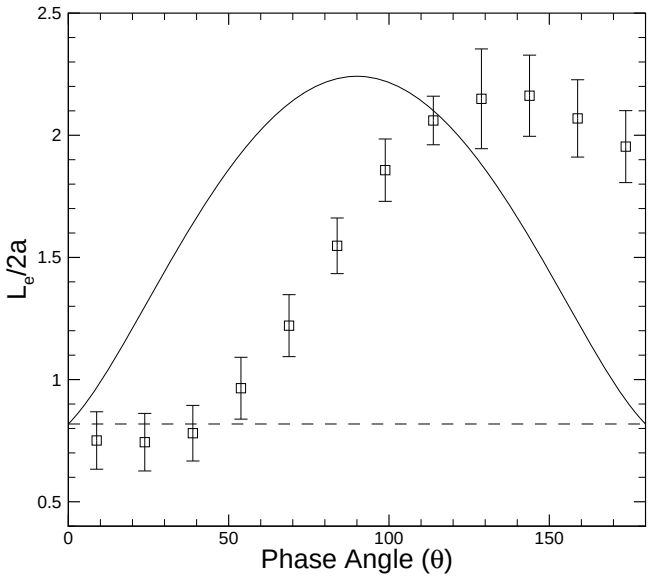

Figure 5.17: Non-dimensional entrance length against phase angle, θ, for $A = 3.70$, $\alpha = 2.45$ and $Re_{puls} = 36$. Symbols are the experimental result. Solid line is Equation 4.3. Dashed line corresponds to Equation 4.3 for the steady flow component.

the steady component. In other words, the entrance length has been reduced by the presence of additional flow, which in this case broadens the shape of the instantaneous developing and fully developed velocity distributions. The entrance length increases of the range of phase angles, $50^o < \theta < 130^o$, and the maximum measured entrance length occurred at $\theta = 129^o$, which is 15^o earlier in the cycle than for $A = 3.70$ which had a smaller steady component.

For a further increase in the steady component, $A = 1.25$, as shown in Figure 5.19, the variation of entrance length with phase angle takes on a much more sinusoidal shape. The reduction of entrance length for early phase angles, $\theta < 50^o$, is very similar to $A = 1.85$ shown in Figure 5.18, and the maximum measured entrance length again occurs at $\theta = 129^o$. After this phase angle, the entrance length is decreased but interestingly for phase angles, $\theta > 180^o$ where the average flow is less than the time mean, the entrance length is still greater than that predicted by the steady flow correlation. That is, the reduction of the instantaneous average flow, $\bar{u}$, by the presence of the oscillating component, increased the

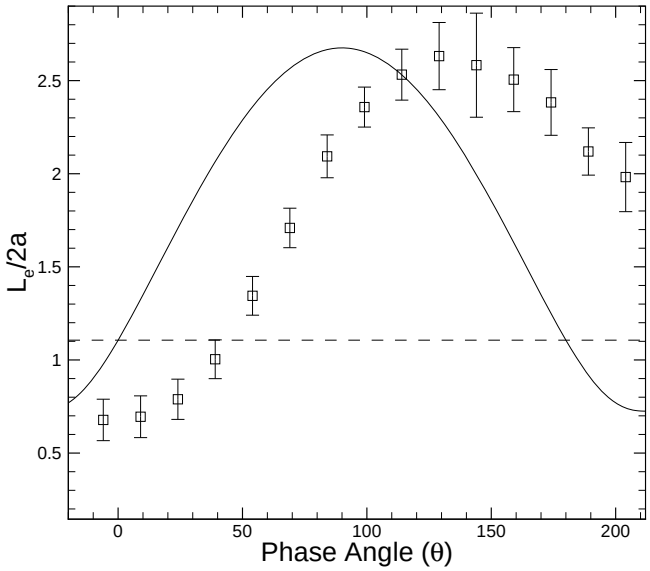

Figure 5.18: Non-dimensional entrance length against phase angle, θ, for $A = 1.85$, $\alpha = 2.45$ and $Re_{puls} = 44$.Symbols are the experimental result. Dashed line corresponds to Equation 4.3. Dashed line is Equation 4.3 for the steady flow component.

entrance length of the flow.

Figure 5.20 shows the variation of entrance length for the largest steady component, $A = 0.93$, and it varies much like the previous case of $A = 1.25$, but now the entire oscillation cycle has been measured. The entrance length appears to oscillate about the mean entrance length, the dashed line in Figure 5.19, much like earlier pulsatile studies (Atabek & Chang (1961),Krijger *et al.* (1991) and He & Ku (1994)). In these studies the entrance length was described as having a delay relative to the average flow, and in Figure 5.20 this delay can be seen by comparing the measured result to the prediction of the entrance length correlation based on the instantaneous average flow. The measured maximum entrance length occurred at $\theta = 131^o$, a delay of 41^o from peak flow, $\theta = 90^o$.

Finally, a direct comparison of the effects of an increasing steady component are shown in Figure 5.21, in which the variation of entrance length with phase angle, θ, has been plotted for each value of A studied (including the purely oscillatory case, $A = \infty$, which is shown as $A = -$. For these measurements,

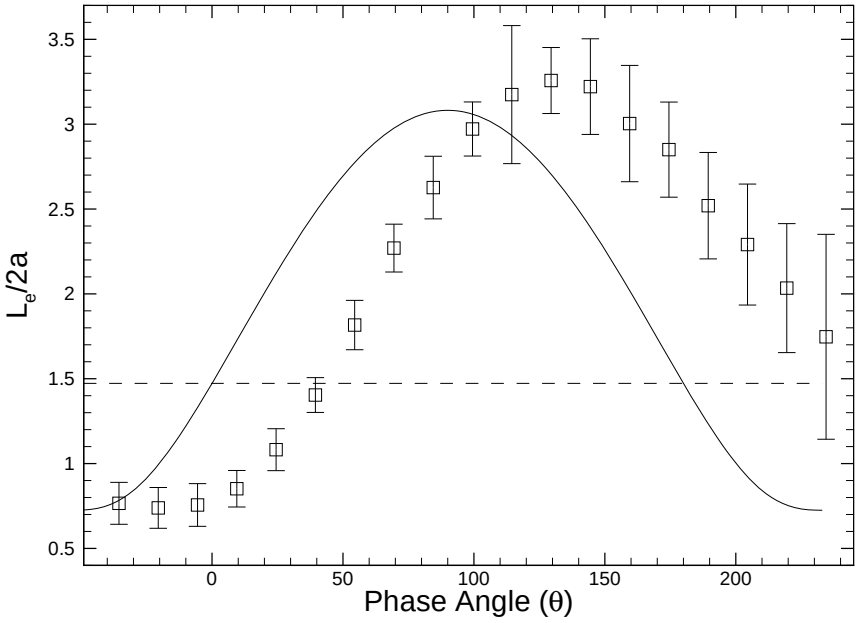

Figure 5.19: Non-dimensional entrance length against phase angle, θ, for $A = 1.25$, $\alpha = 2.45$ and $Re_{puls} = 51$.Symbols are the experimental result. Dashed line corresponds to 4.3. Dashed line is Equation 4.3 for the steady flow component.

the oscillatory component, $\bar{u}_{os}$ was fixed to give $Re_{os} \approx 30$, and the steady flow component, $\bar{u}_s$ increased to give different values of of the relative components, A. The presence of a steady flow component increased the phase angles where the entrance length of the flow could be considered and as can be seen in Figure 5.21 caused a shift of the distributions to earlier in the cycle and closer to the phase angle of the peak average flow, $\theta = 90^o$. The steady component also increased the overall entrance lengths in an approximately linear manner, which can be examined through a comparison of the maximum entrance lengths.

5.2.3 Maximum Entrance Length

The maximum entrance length from the purely oscillatory flow cases presented earlier in Section 5.1.6, was well predicted by the steady flow correlation when the Reynolds was based on the peak average velocity. The maximum entrance lengths for the four values of the ratio, A, examined can be seen in Figure 5.22

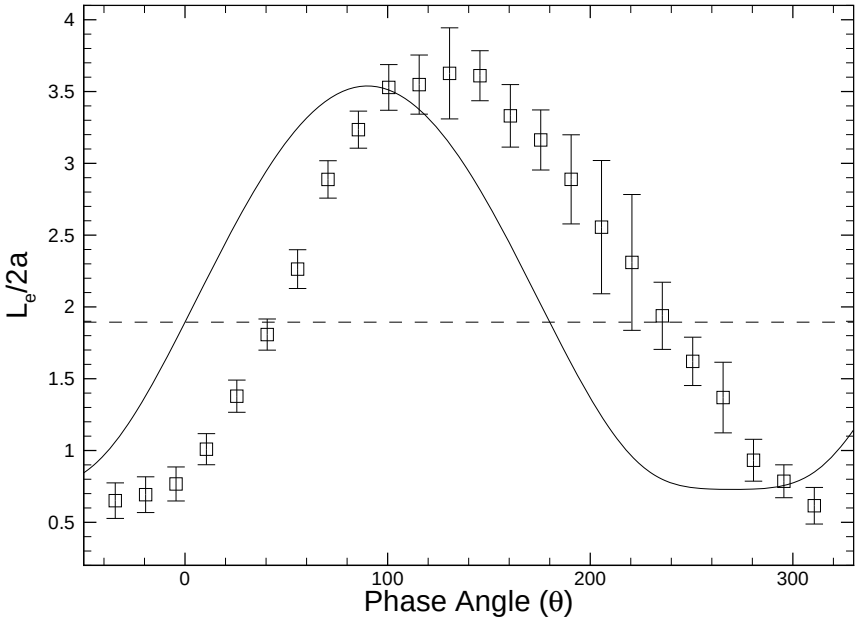

Figure 5.20: Non-dimensional entrance length against phase angle, θ, for $A = 0.93$, $\alpha = 2.45$ and $Re_{puls} = 58$.Symbols are the experimental result. Dashed line corresponds to 4.3. Dashed line is Equation 4.3 for the steady flow component.

alongside the purely oscillatory results. The peak average velocity in this case is $\bar{u}_{puls}$, the addition of both the steady and oscillatory components, and the steady flow correlation, which is the solid line in the figure, has been calculated using Re_{puls}.

In Figure 5.22, the experimental results for the pulsatile flow cases lie close to predicted values from the steady flow correlation based on Re_{puls}. In general the pulsatile results are in slightly better agreement with the steady flow correlation than are the purely oscillatory cases but all values are within 12% of the predictions of the steady flow correlation. It can be concluded that for the oscillatory flows studied with $\alpha \leq 2.45$, the maximum entrance length of the flow can accurately be described by the steady flow correlation using a Reynolds number based on the amplitude of the average flow.

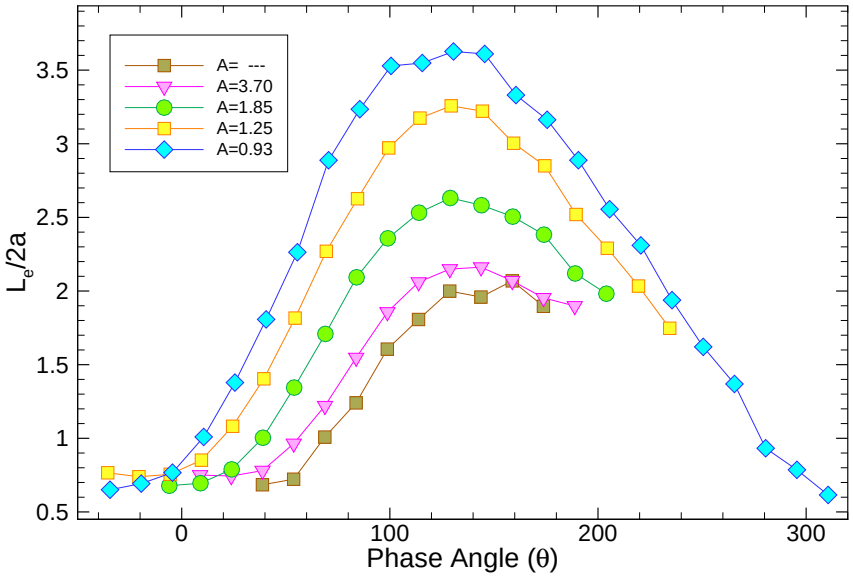

Figure 5.21: Non-dimensional entrance length against phase angle, θ, for varying A, $\alpha = 2.45$.

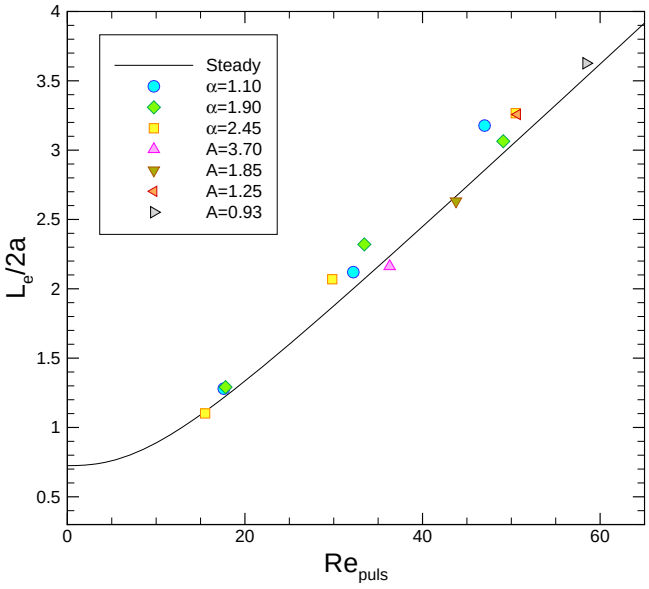

Figure 5.22: Maximum L_e for all oscillatory flow cases against Re_{puls}. Symbols are experimental values. Solid line corresponds to the steady flow correlation, Equation 4.3.

Chapter 6

Conclusions

An experimental study of developing flows in a square microchannel has been performed for steady, oscillatory and pulsatile flow conditions. This study was motivated by the practical importance of the entrance region to microscale flows and the absence of research focused on the conditions most prevalent in microfluidic devices.

A microfluidic device was designed and fabricated from traditional micromachining techniques and an interface system built to connect the microfluidic device to the macro world. The resulting geometry of the microfluidic device were accurately characterised by destructive measurements post experiment using the best possible measuring techniques. In order to produce high quality experimental data, repeat measurements were performed and the results compared with many available sources, such as analytical and numerical solutions and existing correlations to establish their accuracy. The experimental results obtained represent the first systematic experimental study into oscillatory entrance flow from which a number of significant findings were uncovered.

6.1 Key Findings

Topographic measurements of the etched silicon surface of the microfluidic device revealed curvature effects around the walls of the device. For the entrance region of the channel, this caused the depth of the lower surface to vary, which prevented the flow from developing within the first half width into the channel. This is an

important feature that may be present in many devices that have used similar fabrication processes.

The approximately planar entry was studied for steady flow in the channel at low Reynolds numbers in the range, $Re \leq 66$. For $Re = 1$ the velocity distribution entered the channel highly developed with a centreline velocity 87% of its fully developed value. Interestingly at $Re = 66$, small velocity overshoots were found in the developing experimental velocity profiles, which is at a lower Reynolds number than that for which it occurs in circular cross-sections or parallel plate configurations.

Calculation of the entrance length under these conditions was shown to be incredibly difficult. A numerical solution was used to demonstrate the accuracy of the experimental measurements and the method used to determine the entrance length. The numerical results showed the inherent difficultly with determining the entrance length from a curve fitted to the velocity measurements. Despite the fact that the curve fit the data extremely well it resulted in a significant underestimation of the entrance length. A variation to the curve fit procedure was applied, which produced satisfactory results using both numerical and experimental data. The calculated entrance lengths compared well with existing correlations and suggested that the approximately planar entry reduced the entrance lengths by 20-30%. A correlation was proposed for steady flow under these conditions. This correlation would be useful for many microdevices fabricated using similar techniques to the devices used in this study.

For the first time the variation of entrance length with phase angle across the oscillatory cycle was measured experimentally for both purely oscillatory and pulsatile flow. For purely oscillatory flow, at all Stokes numbers studied, $\alpha \leq 2.45$, a large variation of the entrance length occurred across the half of the oscillation cycle for which there was a net flow into the channel. For the lowest Stokes number, $\alpha = 1.10$, the entrance length varied in an approximately quasi-steady manner with a small delay relative to the average flow. For larger Stokes numbers, the entrance length varied between approximately the same maximum and minimum lengths, with an S-shaped distribution across the cycle.

Pulsatile flow was examined for large values of the average oscillatory to steady flow components, $A > 1$, which previously have not been experimentally studied. For $\alpha = 2.45$, the variation of entrance length across the cycle changed from an

S-shaped distribution for purely oscillating flow to a more sinusoidal shape for increasing values of A. The location of the maximum entrance length within the cycle was also found to shift to later phase angles for increasing values of A. For the smallest relative oscillatory component, $A = 0.93$, the variation of entrance length was shown to oscillate about the steady flow.

The maximum entrance length for all cases was found to be well approximated by the steady flow entrance length correlation when the Reynolds number was based on the amplitude of the cross-sectional average flow. This result extends and experimentally confirms the numerical findings of He & Ku (1994), who suggested this result for pulsatile flows. The current results, along with those citied in literature suggest that for time dependent flows it is the amplitude of the flow that determines the entrance length and that a maximum entrance length can be calculated directly from correlations based on the much simpler case of steady flow. This result is a significant finding and will be greatly beneficial to an increasingly large number of applications which employ time varying flows.

The experimental data generated by the current study, along with the thorough uncertainty analysis were performed to the highest standards suggested in the literature. The experimental results compared exceedingly well with the corresponding numerical study and to existing results in the literature. Therefore the results and findings of the current study serve as a benchmark for future experimental studies and as a source of validation for various numerical models, for which high quality experimental data is often scarce.

6.2 Recommendations for Future Work

This dissertation has examined developing flow in a square microchannel at low Reynolds number and low Stokes numbers. The oscillatory and pulsatile cases examined in this work were for those which the entrance region was suggested to be as large as it is in study flow. Future works could extend the range of Stokes numbers in order to determine the reduction of entrance length, which has been found in numerical results for oscillatory flows (Raju *et al.* (2005)), and for pulsatile flows (Krijger *et al.* (1991), He & Ku (1994)). This task would be best suited to flow in a circular channel, where the variation of the location where

the maximum velocity occurs, can be captured by a single measurement plane that passes through the centreline.

One of the most promising applications for microdevices is in heat transfer augmentation. The design and optimisation of potential devices would greatly benefit from knowledge of the thermal entrance length in microchannel flows. Investigation of the thermal entrance length for both steady and pulsatile flow conditions either numerically or experimentally would also be a worthy avenue of future study.

Measurements of the flow fields in the chamber under oscillatory flow conditions revealed the formation of highly complex flow patterns, reminiscent of those found in synthetic jet devices. For the range of experimental parameters studied, a jet was formed that travelled away from the channel inlet but could not be sustained over the entire oscillation cycle. The large viscous forces, generated by the close proximity of the upper and lower surfaces of the chamber, caused the propagation of the jet to slow and eventually dissipate. Study of the formation of a sustained jet under these conditions, would be an interesting topic of further research as synthetic jets have been proposed for a number of microscale applications, yet currently for these devices there exists little experimental work at this scale in the literature.

Appendix A

Details of the numerical model

A.1 CFD Model details

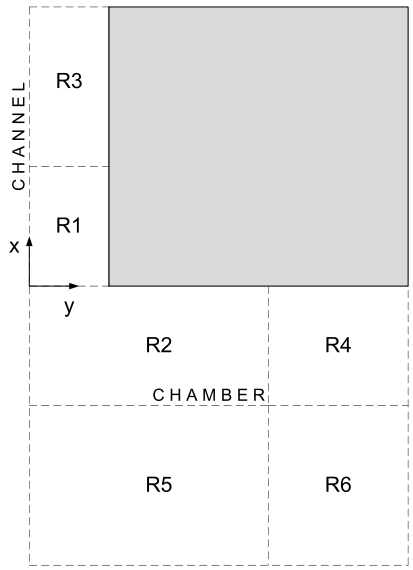

Figure A.1: Schematic diagram of the numerical domain.

In Figure A.1 the lower surface has been divided into regions, R1 and R3 inside the channel and regions R2, R4, R5, R6 inside the chamber. In the channel the

lower surfaces varies in depth in region R1 but in region R3 the lower surface remains invariant in the x-direction. The division between R3 and R1 occurs at $x/a = 4$, where the optical profiler measurements found essentially no variation in depth or shape. In the chamber, the low surface varies in depth throughout region R2 and in all directions. Region R4 is invariant in the y-direction, with the division between R2 and R4 at $y/a = 3$. Region R5 is invariant in the x-direction, with the division between R2 and R5 at $x/a = 2$. Region R6 is a constant depth throughout.

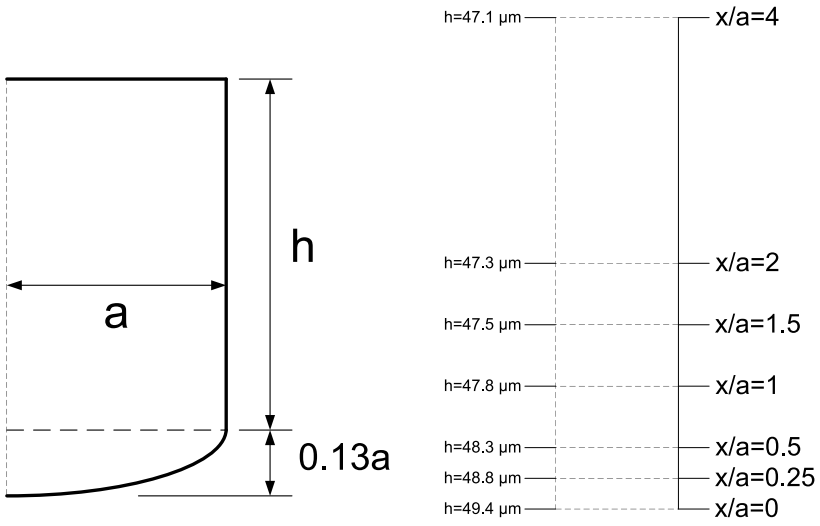

(a) Channel cross-section (b) Region R1

Figure A.2: Geometry of the channel in the numerical model.

The cross-section in region R1 was modelled as a rectangle and quarter ellipse connected together, as can be seen in Figure A.2(a). Throughout the region R1, the dimensions of the ellipse component of the cross-section remained the same but the length of the vertical sides of the rectangle, h, was varied in order to achieve the correct depth of the centreline as shown earlier in Figure 3.9. The quarter ellipse was found to be a good approximation of the lower surface in region R1, in the measurements made by the optical profiler. Seven different lengths, h, at seven locations along the x-axis shown in Figure A.2(b), were imported into the model. A surface was fitted through the seven quarter ellipse curves located at those seven depths using splines.

(a) Region R2

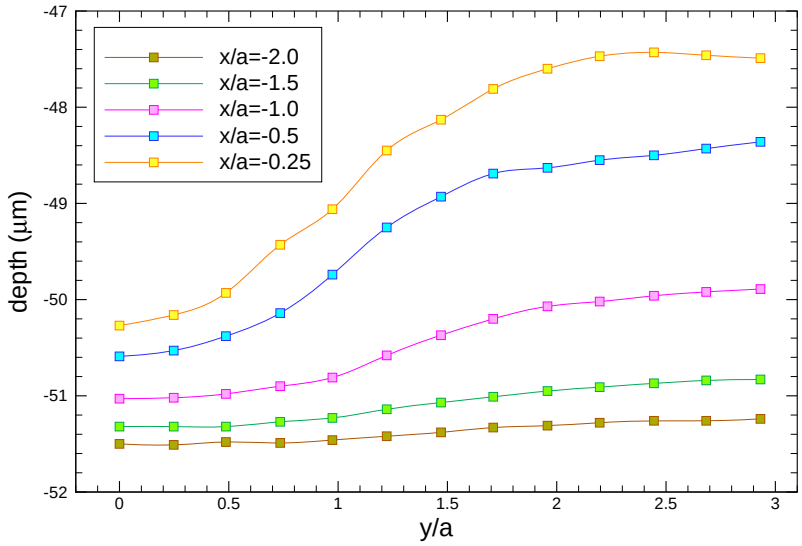

(b) Profile measurements

Figure A.3: Geometry of the chamber in the numerical model.

In region R2, as shown in Figure A.3, the lower surface was far enough away from the walls that the measurements made from the optical profiles could be used in a more direct way. At the locations shown in Figure A.3(a) lines consisting of 13 equal spaced points were extracted from the profile measurements, shown in Figure A.3(b). These lines were imported into the model, and a surface was fitted through the seven lines using splines.

References

Abarbanel, S., Bennett, S., Brandt, A. & Gillis, J. (1970). Velocity profiles of flow at low reynolds numbers. *Journal of Applied Mechanics*, **37**, 2. 16

Abgrall, P. & Gue, A. (2007). Lab-on-chip technologies: making a microfluidic network and coupling it into a complete microsystema review. *Journal of Micromechanics and Microengineering*, **17**, R15. 11, 12

Adrian, R. (2005). Twenty years of particle image velocimetry. *Experiments in Fluids*, **39**, 159–169. 68

Ahmad, T. & Hassan, I. (2010). Experimental analysis of microchannel entrance length characteristics using microparticle image velocimetry. *Journal of Fluids Engineering*, **132**, 041102. xiii, 5, 27, 28, 107, 108, 109

Anna, S., Bontoux, N. & Stone, H. (2003). Formation of dispersions using flow focusing in microchannels. *Applied Physics Letters*, **82**, 364. 8

Atabek, H. (1962). Development of flow in the inlet length of a circular tube starting from rest. *Zeitschrift für Angewandte Mathematik und Physik (ZAMP)*, **13**, 417–430. 34, 35

Atabek, H. & Chang, C. (1961). Oscillatory flow near the entry of a circular tube. *Zeitschrift für Angewandte Mathematik und Physik (ZAMP)*, **12**, 185–201. xiv, 34, 35, 41, 43, 136

Atabek, H., Chang, C. & Fingerson, L. (1964). Measurement of laminar oscillatory flow in the inlet length of a circular tube. *Physics in Medicine and Biology*, **9**, 219. 43

Atkinson, B., Kemblowski, Z. & Smith, J. (1967). Measurements of velocity profile in developing liquid flows. *AIChE Journal*, **13**, 17–20. 16

Atkinson, B., Brocklebank, M., Card, C. & Smith, J. (1969). Low Reynolds number developing flows. *AIChE Journal*, **15**, 548–553. xiii, 2, 17, 18, 19, 21, 23, 106

Bayraktar, T. & Pidugu, S. (2006). Characterization of liquid flows in microfluidic systems. *International Journal of Heat and Mass Transfer*, **49**, 815–824. 5

Beavers, G., Sparrow, E. & Magnuson, R. (1970). Experiments on hydrodynamically developing flow in rectangular ducts of arbitrary aspect ratio. *International Journal of Heat and Mass Transfer*, **13**, 689–701. 19

Beebe, D., Mensing, G. & Walker, G. (2002). Physics and applications of microfluidics in biology. *Annual Review of Biomedical Engineering*, **4**, 261–286. 3

Berman, N. & Santos, V. (1969). Laminar velocity profiles in developing flows using a laser doppler technique. *AIChE Journal*, **15**, 323–327. 16, 19, 21

Bhagat, A., Jothimuthu, P., Pais, A. & Papautsky, I. (2007). Re-usable quick-release interconnect for characterization of microfluidic systems. *Journal of Micromechanics and Microengineering*, **17**, 42. 13, 14

Bodoia, J. & Osterle, J. (1961). Finite difference analysis of plane poiseuille and couette flow developments. *Applied Scientific Research*, **10**, 265–276. 16

Boger, D. (1982). Circular entry flows of inelastic and viscoelastic fluids. *Advances in Transport Processes*, **2**, 43–104. 1, 2, 22, 23, 44

Boger, D. (1987). Viscoelastic flows through contractions. *Annual Review of Fluid Mechanics*, **19**, 157–182. 3

Boillot, A. & Prasad, A. (1996). Optimization procedure for pulse separation in cross-correlation PIV. *Experiments in Fluids*, **21**, 87–93. 65, 79

Bottausci, F., Mezić, I., Meinhart, C. & Cardonne, C. (2004). Mixing in the shear superposition micromixer: three-dimensional analysis. *Philosophical Transactions of the Royal Society of London. Series A: Mathematical, Physical and Engineering Sciences*, **362**, 1001. 4

Bourdon, C., Olsen, M. & Gorby, A. (2004). Power-filter technique for modifying depth of correlation in microPIV experiments. *Experiments in Fluids*, **37**, 263–271. 67

Brandt, A. & Gillis, J. (1966). Magnetohydrodynamic flow in the inlet region of a straight channel. *Physics of Fluids*, **9**, 690. 16

Brocklebank, M. & Smith, J. (1968). Laminar velocity profile development in straight pipes of circular cross section. *Rheologica Acta*, **7**, 286–289. 19, 21

Burke, J. & Berman, N. (1969). Entrance flow development in circular tubes at small axial distances. paper 69-wa/fe-13. ASME. 24

Cao, B., Sun, J., Chen, M. & Guo, Z. (2009). Molecular momentum transport at fluid-solid interfaces in mems/nems: a review. *International Journal of Molecular Sciences*, **10**, 4638–4706. 9

Caro, C., Pedley, T., Schroter, R. & Seed, W. (1978). *The mechanics of the circulation*, vol. 527. Oxford University Press New York. 36, 37, 38

Celata, G., Lorenzini, M., Morini, G. & Zummo, G. (2009). Friction factor in micropipe gas flow under laminar, transition and turbulent flow regime. *International Journal of heat and fluid flow*, **30**, 814–822. 11

Chan, W., Lee, S. & Liu, C. (2002). Effects of frequency and amplitude of oscillation on low reynolds number pulsating flow in a circular pipe. *Engineering Computations*, **19**, 119–132. 42

Chang, C. & Atabek, H. (1961). The inlet length for oscillatory flow and its effects on the determination of the rate of flow in arteries. *Physics in Medicine and Biology*, **6**, 303. 29

Chen, R. (1973). Flow in the entrance region at low Reynolds numbers. *Journal of Fluids Engineering*, **95**, 153. 18, 38, 106, 107

Cheng, J. & Giordano, N. (2002). Fluid flow through nanometer-scale channels. *Physical Review E*, **65**, 031206. 8

Cho, H. & Hyun, J. (1990). Numerical solutions of pulsating flow and heat transfer characteristics in a pipe. *International Journal of Heat and Fluid Flow*, **11**, 321–330. 42, 43

Christiansen, E., Kelsey, S. & Carter, T. (1972). Laminar tube flow through an abrupt contraction. *AIChE Journal*, **18**, 372–380. 21, 22, 23, 24, 96

Coleman, H. & Steele, W. (1999). *Experimentation and uncertainty analysis for engineers*. Wiley-Interscience. 76, 78, 104

Costaschuk, D., Elsnab, J., Petersen, S., Klewicki, J. & Ameel, T. (2007). Axial static pressure measurements of water flow in a rectangular microchannel. *Experiments in Fluids*, **43**, 907–916. 27

Denison, E., Stevenson, W. & Fox, R. (1971). Pulsating laminar flow measurements with a directionally sensitive laser velocimeter. *AIChE Journal*, **17**, 781–787. 43

Dombrowski, N., Foumeny, E., Ookawara, S. & Riza, A. (1993). The influence of reynolds number on the entry length and pressure drop for laminar pipe flow. *The Canadian Journal of Chemical Engineering*, **71**, 472–476. 18

Drake, D. (1965). On the flow in a channel due to a periodic pressure gradient. *The Quarterly Journal of Mechanics and Applied Mathematics*, **18**, 1. xvi, xvii, 33, 73, 111, 112, 113, 114, 118, 128, 129, 130, 131, 132, 133

Durst, F. & Loy, T. (1985). Investigations of laminar flow in a pipe with sudden contraction of cross sectional area. *Computers & fluids*, **13**, 15–36. 22, 24, 88

Durst, F., Ray, S., Ünsal, B. & Bayoumi, O. (2005). The development lengths of laminar pipe and channel flows. *Journal of Fluids Engineering*, **127**, 1154. 18, 106

Effenhauser, C., Paulus, A., Manz, A. & Widmer, H. (1994). High-speed separation of antisense oligonucleotides on a micromachined capillary electrophoresis device. *Analytical Chemistry*, **66**, 2949–2953. 8

Fan, C. & Chao, B. (1965). Unsteady, laminar, incompressible flow through rectangular ducts. *Zeitschrift für Angewandte Mathematik und Physik (ZAMP)*, **16**, 351–360. 33

Fan, L. & Hwang, C. (1966). Bibliography of hydrodynamic entrance region flow. *Kansas State University Bulletin*, **50**. 15

Fargie, D. & Martin, B. (1971). Developing laminar flow in a pipe of circular cross-section. *Proceedings of the Royal Society of London. A. Mathematical and Physical Sciences*, **321**, 461. 15

Florio, P., Mueller, W. & of Mechanical Engineers, A.S. (1968). Development of a periodic flow in a rigid tube. vol. 90, 395–399, ASME J. Basic Eng. 42, 43

Fox, R., McDonald, A. & Pritchard, P. (1985). *Introduction to fluid mechanics*, vol. 7. John Wiley & Sons New York. 9

Fredrickson, C. & Fan, Z. (2004). Macro-to-micro interfaces for microfluidic devices. *Lab Chip*, **4**, 526–533. 13, 14

Friedmann, M., Gillis, J. & Liron, N. (1968). Laminar flow in a pipe at low and moderate Reynolds numbers. *Applied Scientific Research*, **19**, 426–438. xiii, 16, 17, 18, 21, 23

Fung, Y. (1997). *Biomechanics: circulation*. Springer Verlag. 31, 36

Gad-el Hak, M. (1999). The fluid mechanics of microdevices-the freeman scholar lecture. *Trans ASME J Fluids Eng*, **121**, 5–33. 9

Gamrat, G., Favre-Marinet, M., Le Person, S., Baviere, R. & Ayela, F. (2008). An experimental study and modelling of roughness effects on laminar flow in microchannels. *Journal of Fluid Mechanics*, **594**, 399–424. 11

Gerrard, J. & Hughes, M. (1971). The flow due to an oscillating piston in a cylindrical tube: a comparison between experiment and a simple entrance flow theory. *Journal of Fluid Mechanics*, **50**, 97–106. 35, 36, 37, 38, 40, 44

Glasgow, I. & Aubry, N. (2003). Enhancement of microfluidic mixing using time pulsing. *Lab Chip*, **3**, 114–120. 4

Glezer, A. & Amitay, M. (2002). Synthetic jets. *Annual Review of Fluid Mechanics*, **34**, 503–529. 115

Goldstein, R. & Kreid, D. (1967). Measurement of laminar flow development in a square duct using a laser-doppler flowmeter. *Journal of Applied Mechanics*, **34**, 813. 19

Hale, J., McDonald, D. & Womersley, J. (1955). Velocity profiles of oscillating arterial flow, with some calculations of viscous drag and the reynolds number. *The Journal of Physiology*, **128**, 629. 33

Han, L. (1960). Hydrodynamic entrance lengths for incompressible laminar flow in rectangular ducts. *J. Appl. Mech*, **27**, 403–409. 3, 19

Hao, P., He, F. & Zhu, K. (2005). Flow characteristics in a trapezoidal silicon microchannel. *Journal of Micromechanics and Microengineering*, **15**, 1362. 29

Haubert, K., Drier, T. & Beebe, D. (2006). PDMS bonding by means of a portable, low-cost corona system. *Lab on a Chip*, **6**, 1548–1549. 12

Hawken, D., Townsend, P. & Webster, M. (1991). Numerical simulation of viscous flows in channels with a step. *Computers & Fluids*, **20**, 59–75. 24

He, X. & Ku, D. (1994). Unsteady entrance flow development in a straight tube. *Journal of Biomechanical Engineering*, **116**, 355. 35, 42, 43, 44, 124, 136, 142

Hessel, V., Lowe, H. & Schonfeld, F. (2005). Micromixers–a review on passive and active mixing principles. *Chemical Engineering Science*, **60**, 2479–2501. 3

Ho, C. & Tai, Y. (1998). Micro-electro-mechanical-systems (mems) and fluid flows. *Annual Review of Fluid Mechanics*, **30**, 579–612. 8

Hornbeck, R. (1964). Laminar flow in the entrance region of a pipe. *Applied Scientific Research*, **13**, 224–232. 16

Hsieh, S., Lin, C., Huang, C. & Tsai, H. (2004). Liquid flow in a micro-channel. *Journal of Micromechanics and Microengineering*, **14**, 436. 27

Hunt, R. (1990). The numerical solution of the laminar flow in a constricted channel at moderately high reynolds number using newton iteration. *International Journal for Numerical Methods in Fluids*, **11**, 247–259. 24

Iguchi, M., Park, G., Akao, F. & Yamamoto, F. (1992). A study on velocity profiles of developing laminar oscillatory flows in a square duct. *JSME International Journal*, **35**, 158–164. 37

Iverson, B. & Garimella, S. (2008). Recent advances in microscale pumping technologies: a review and evaluation. *Microfluidics and Nanofluidics*, **5**, 145–174. 4

Jaworski, A., Mao, X., Mao, X. & Yu, Z. (2009). Entrance effects in the channels of the parallel plate stack in oscillatory flow conditions. *Experimental Thermal and Fluid Science*, **33**, 495–502. 35, 40, 115

Judy, J., Maynes, D. & Webb, B. (2002). Characterization of frictional pressure drop for liquid flows through microchannels. *International Journal of Heat and Mass Transfer*, **45**, 3477–3489. 11

Kandlikar, S. (2006). *Heat transfer and fluid flow in minichannels and microchannels*. Elsevier Science. xix, 8

Kassianides, E. & Gerrard, J. (1975). The calculation of entrance length in physiological flow. *Medical and Biological Engineering and Computing*, **13**, 558–560. 36, 121

Keane, R. & Adrian, R. (1992). Theory of cross-correlation analysis of PIV images. *Applied Scientific Research*, **49**, 191–215. 65

Kerswell, R. (2005). Recent progress in understanding the transition to turbulence in a pipe. *Nonlinearity*, **18**, R17. 10

Kim-e, M., Brown, R. & Armstrong, R. (1983). The roles of inertia and shear-thinning in flow of an inelastic liquid through an axisymmetric sudden contraction. *Journal of Non-Newtonian Fluid Mechanics*, **13**, 341–363. 22, 23, 96

Krijger, J., Hillen, B. & Hoogstraten, H. (1991). Pulsating entry-flow in a plane channel. *Zeitschrift für Angewandte Mathematik und Physik (ZAMP)*, **42**, 139–153. 35, 41, 42, 124, 126, 136, 142

Ku, D. (1997). Blood flow in arteries. *Annual Review of Fluid Mechanics*, **29**, 399–434. 29

Langhaar, H. (1942). Steady flow in the transition length of a straight tube. *Journal of Applied Mechanics*, **9**, 55–58. 16

Laser, D. & Santiago, J. (2004). A review of micropumps. *Journal of Micromechanics and Microengineering*, **14**, R35. 4

Lauga, E. & Stone, H. (2003). Effective slip in pressure-driven stokes flow. *Journal of Fluid Mechanics*, **489**, 55–77. 9

Lee, S. & Kim, G. (2003). Analysis of flow resistance inside microchannels with different inlet configurations using micro-piv system. 823–830. 26

Lee, S., Wereley, S., Gui, L., Qu, W. & Mudawar, I. (2002). Microchannel flow measurement using micro particle image velocimetry. *ASME Fluids Engineering Division*, **258**, 493–500. 25

Lee, S., Jang, J. & Wereley, S. (2008). Effects of planar inlet plenums on the hydrodynamically developing flows in rectangular microchannels of complementary aspect ratios. *Microfluidics and Nanofluidics*, **5**, 1–12. xiii, 5, 13, 25, 26, 44, 72, 93, 98, 100, 107, 108, 109

Lew, H. & Fung, Y. (1969). On the low-reynolds-number entry flow into a circular cylindrical tube. *Journal of Biomechanics*, **2**, 105–119. 16

Li, H. & Olsen, M. (2006). Micropiv measurements of turbulent flow in square microchannels with hydraulic diameters from 200 [mu] m to 640 [mu] m. *International journal of heat and fluid flow*, **27**, 123–134. 11

Li, Z. (2003). Experimental study on flow characteristics of liquid in circular microtubes. *Microscale Thermophysical Engineering*, **7**, 253–265. 11

Lindken, R., Rossi, M., Grosse, S. & Westerweel, J. (2009). Micro-Particle Image Velocimetry (μPIV): Recent developments, applications, and guidelines. *Lab on a Chip*, **9**, 2551–2567. 62, 63, 79

Madou, M. (2002). *Fundamentals of microfabrication: the science of miniaturization*. CRC. 12

Massey, B. & Ward-Smith, J. (1998). *Mechanics of fluids*, vol. 1. Taylor & Francis. 9

Meinhart, C. & Zhang, H. (2000). The flow structure inside a microfabricated inkjet printhead. *Journal of Microelectromechanical Systems*, **9**, 67–75. 63

Meinhart, C., Wereley, S. & Santiago, J. (1999). PIV measurements of a microchannel flow. *Experiments in Fluids*, **27**, 414–419. 59

Meinhart, C., Wereley, S. & Santiago, J. (2000). A PIV algorithm for estimating time-averaged velocity fields. *Trans ASME J. Fluids Eng*, **122**, 285–289. 61, 68

Michaelides, E. (1997). Reviewthe transient equation of motion for particles, bubbles, and droplets. *Journal of Fluids Engineering*, **119**, 233. 64

Moffat, R. (1988). Describing the uncertainties in experimental results. *Experimental Thermal and Fluid Science*, **1**, 3–17. 76

Mohiuddin Mala, G. & Li, D. (1999). Flow characteristics of water in microtubes. *International Journal of Heat and Fluid Flow*, **20**, 142–148. 10

Morihara, H. & Ta-Shun Cheng, R. (1973). Numerical solution of the viscous flow in the entrance region of parallel plates. *Journal of Computational Physics*, **11**, 550–572. 15, 16, 18, 23

Morini, G. (2004). Laminar-to-turbulent flow transition in microchannels. *Microscale Thermophysical Engineering*, **8**, 15–30. 11

Morini, G. (2005). Viscous heating in liquid flows in micro-channels. *International Journal of Heat and Mass Transfer*, **48**, 3637–3647. 11

Morris, C. & Forster, F. (2000). Optimization of a circular piezoelectric bimorph for a micropump driver. *Journal of Micromechanics and Microengineering*, **10**, 459–465. 47

Morris, C. & Forster, F. (2003). Low-order modeling of resonance for fixed-valve micropumps based on first principles. *Microelectromechanical Systems, Journal of*, **12**, 325–334. 71

Muchnik, G., Solomonov, S. & Gordon, A. (1973). Hydrodynamic development of a laminar velocity field in rectangular channels. *Journal of Engineering Physics and Thermophysics*, **25**, 1268–1271. 19

Natrajan, V. & Christensen, K. (2007). Microscopic particle image velocimetry measurements of transition to turbulence in microscale capillaries. *Experiments in fluids*, **43**, 1–16. 11

Nguyen, C., Fouras, A. & Carberry, J. (2010). Improvement of measurement accuracy in micro PIV by image overlapping. *Experiments in Fluids*, 1–12. 67

Nguyen, N. & Wereley, S. (2002). *Fundamentals and applications of microfluidics*. Artech House Publishers. 9, 12

Niklaus, F., Stemme, G., Lu, J. & Gutmann, R. (2006). Adhesive wafer bonding. *Journal of Applied Physics*, **99**, 031101. 12

Nilsson, A., Petersson, F., Jönsson, H. & Laurell, T. (2004). Acoustic control of suspended particles in micro fluidic chips. *Lab on a Chip*, **4**, 131–135. 4

Nittis, V., Fortt, R., Legge, C. & Mello, A. (2001). A high-pressure interconnect for chemical microsystem applications. *Lab on a Chip*, **1**, 148–152. 13, 14

Oak, J., Pence, D. & Liburdy, J. (2004). Flow development of co-flowing streams in rectangular micro-channels. *Microscale Thermophysical Engineering*, **8**, 111–128. 29

Olsen, M. & Adrian, R. (2000). Out-of-focus effects on particle image visibility and correlation in microscopic particle image velocimetry. *Experiments in Fluids*, **29**, 166–174. 61, 62

Patankar, S. (1980). *Numerical heat transfer and fluid flow*. Hemisphere Pub. 81

Peng, X. & Peterson, G. (1996). Forced convection heat transfer of single-phase binary mixtures through microchannels. *Experimental Thermal and fluid science*, **12**, 98–104. 5, 10

Peng, X., Peterson, G. & Wang, B. (1994). Frictional flow characteristics of water flowing through rectangular microchannels. *Experimental Heat Transfer*, **7**, 249–264. 10

Pfenninger, W. (1961). Boundary layer suction experiments with laminar flow at high reynolds numbers in the inlet length of a tube by various suction methods. *Boundary layer and flow control Lachman GV*, 961–980. 16

Poelma, C., Vennemann, P., Lindken, R. & Westerweel, J. (2008). In vivo blood flow and wall shear stress measurements in the vitelline network. *Experiments in Fluids*, **45**, 703–713. 66

Prasad, A., Adrian, R., Landreth, C. & Offutt, P. (1992). Effect of resolution on the speed and accuracy of particle image velocimetry interrogation. *Experiments in Fluids*, **13**, 105–116. 79

Qu, W., Mala, G. & Li, D. (2000). Pressure-driven water flows in trapezoidal silicon microchannels. *Int. J. Heat Mass Transfer*, **43**, 353–364. 10

Raffel, M., Willert, C. & Kompenhans, J. (1998). *Particle image velocimetry*. Springer Heidelberg. 60, 62

Raju, R., Mittal, R., Gallas, Q. & Cattafesta, L. (2005). Scaling of vorticity flux and entrance length effects in zero-net mass-flux devices. *AIAA paper*, **4751**, 2005. xiii, 35, 37, 38, 39, 123, 126, 142

Richardson, E. (1927). The amplitude of sound waves in resonators. *Proceedings of the Physical Society*, **40**, 206. 33

Rossi, M., Cierpka, C., Segura, R. & Kähler, C. (2010). On the effect of particle image intensity and image preprocessing on depth of correlation in micro-PIV. In *15th International symposium on applications of laser techniques to fluid mechanics, Lisbon, Portugal*, 05–08. 67, 72

Rouse, H. & Ince, S. (1963). *History of hydraulics*. Dover Publications. 8

Sadri, R. (2002). Accurate Evaluation of the loss coefficient and the entrance length of the inlet region of a channel. *Journal of Fluids Engineering*, **124**, 685. 21, 24

Santiago, J., Wereley, S., Meinhart, C., Beebe, D. & Adrian, R. (1998). A particle image velocimetry system for microfluidics. *Experiments in Fluids*, **25**, 316–319. 59, 64

Schlichting, H. & Gersten, K. (2000). *Boundary-layer theory*. Springer Verlag. 1, 16, 30, 33

Schmidt, F. & Zeldin, B. (1971). Laminar heat transfer in the entrance region of ducts. *Applied Scientific Research*, **23**, 73–94. 15

Schmidt, M. (1998). Wafer-to-wafer bonding for microstructure formation. *Proceedings of the IEEE*, **86**, 1575–1585. 12

Sexl, T. (1930). Über den von EG Richardson entdeckten Annulareffekt . *Zeitschrift für Physik A Hadrons and Nuclei*, **61**, 349–362. 31

Shah, R. & London, A. (1978). *Laminar flow forced convection in ducts: a source book for compact heat exchanger analytical data*. Academic press New York, NY. 2, 10, 15, 16, 18, 87

Sharp, K. & Adrian, R. (2004). Transition from laminar to turbulent flow in liquid filled microtubes. *Experiments in Fluids*, **36**, 741–747. 11

Sheen, H., Hsu, C., Wu, T., Chang, C., Chu, H., Yang, C. & Lei, U. (2008). Unsteady flow behaviors in an obstacle-type valveless micropump by micro-PIV. *Microfluidics and Nanofluidics*, **4**, 331–342. 47

Shimura, K., Koyama, Y., Sato, K. & Kitamori, T. (2007). On-chip connector valve for immunoaffinity chromatography in a microfluidic chip. *Journal of Separation Science*, **30**, 1477–1481. xiv, 14, 56, 57

Smith, B. & Glezer, A. (1998). The formation and evolution of synthetic jets. *Physics of fluids*, **10**, 2281. 115

Sparrow, E. & Anderson, C. (1977). Effect of upstream flow processes on hydrodynamic development in a duct. *Journal of Fluids Engineering*, **99**, 556. 19, 21, 24, 88, 93

Sparrow, E., Lin, S. & Lundgren, T. (1964). Flow development in the hydrodynamic entrance region of tubes and ducts. *Physics of Fluids*, **7**, 338. 2

Sparrow, E., Hixon, C. & Shavit, G. (1966). Experiments on laminar flow development in rectangular ducts. vol. 89. 19

Squires, T. & Quake, S. (2005). Microfluidics: Fluid physics at the nanoliter scale. *Reviews of Modern Physics*, **77**, 977. 3

Steinke, M. & Kandlikar, S. (2006). Single-phase liquid friction factors in microchannels. *International Journal of Thermal Sciences*, **45**, 1073–1083. 5, 11, 43

Stone, H., Stroock, A. & Ajdari, A. (2004). Engineering flows in small devices. *Annu. Rev. Fluid Mech.*, **36**, 381–411. 4, 10, 13, 71

Tachibana, M., Kawabata, N. & Genno, H. (1986). Steady laminar flow of power-law fluids in the inlet region of rectangular ducts. *Journal of Rheology*, **30**, 517. 19

Thompson, B., Maynes, D. & Webb, B. (2005). Characterization of the hydrodynamically developing flow in a microtube using mtv. *Journal of Fluids Engineering*, **127**, 1003. 27

Tietjens, O., Prandtl, L. & Den Hartog, J. (1934). *Applied hydro-and aeromechanics*. McGraw-Hill Book Company, inc. 1, 10, 15

Tikekar, M., Singh, S. & Agrawal, A. (2010). Measurement and modeling of pulsatile flow in microchannel. *Microfluidics and Nanofluidics*, 1–16. 4

Timchenko, V., Reizes, J. & Leonardi, E. (2007). An evaluation of synthetic jets for heat transfer enhancement in air cooled micro-channels. *International Journal of Numerical Methods for Heat & Fluid Flow*, **17**, 263–283. 4

Uchida, S. (1956). The pulsating viscous flow superposed on the steady laminar motion of incompressible fluid in a circular pipe. *Zeitschrift für Angewandte Mathematik und Physik (ZAMP)*, **7**, 403–422. 31

Vrentas, J. & Duda, J. (1973). Flow of a newtonian fluid through a sudden contraction. *Applied Scientific Research*, **28**, 241–260. 22, 24, 88

Vrentas, J., Duda, J. & Bargeron, K. (1966). Effect of axial diffusion of vorticity on flow development in circular conduits: Part i. numerical solutions. *AIChE Journal*, **12**, 837–844. xiii, 20, 21, 22, 88, 93, 106

Wagner, M. (1975). Developing flow in circular conduits: transition from plug flow to tube flow. *Journal of Fluid Mechanics*, **72**, 257–268. 1, 2, 15

Wang, Y. & Longwell, P. (1964). Laminar flow in the inlet section of parallel plates. *AIChE Journal*, **10**, 323–329. 20, 21, 23, 88

Wereley, S. & Meinhart, C. (2010). Recent Advances in Micro-Particle Image Velocimetry. *Annual Review of Fluid Mechanics*, **42**, 557–576. 60

Westerweel, J. (1994). Efficient detection of spurious vectors in particle image velocimetry data. *Experiments in Fluids*, **16**, 236–247. 68

Westerweel, J. (1997). Fundamentals of digital particle image velocimetry. *Measurement Science and Technology*, **8**, 1379–1392. 59

Westerweel, J. (2000). Theoretical analysis of the measurement precision in particle image velocimetry. *Experiments in Fluids*, **29**, 3–12. 62, 79

Westerweel, J. (2008). On velocity gradients in PIV interrogation. *Experiments in Fluids*, **44**, 831–842. 65

White, F. (1991). *Viscous fluid flow*. McGraw-Hill New York. xv, xvii, 10, 31, 81, 87, 128, 129, 130, 131, 132, 133

White, F. (1999). *Fluid mechanics*. McGraw-Hill, New York. 2, 10

Whitesides, G. (2006). The origins and the future of microfluidics. *Nature*, **442**, 368–373. 3, 12

Wiginton, C. & Dalton, C. (1970). Incompressible laminar flow in the entrance region of a rectangular duct. *Journal of Applied Mechanics*, **37**, 854. 19

Womersley, J. (1955). Method for the calculation of velocity, rate of flow and viscous drag in arteries when the pressure gradient is known. *The Journal of Physiology*, **127**, 553. 31

Wu, P. & Little, W. (1984). Measurement of the heat transfer characteristics of gas flow in fine channel heat exchangers used for microminiature refrigerators. *Cryogenics*, **24**, 415–420. 10

Yamanaka, G., Kikura, H., Takeda, Y. & Aritomi, M. (2002). Flow measurement on an oscillating pipe flow near the entrance using the UVP method. *Experiments in Fluids*, **32**, 212–220. 35, 40

Yang, J., Bhattacharyya, A., Masliyah, J. & Kwok, D. (2003). Oscillating laminar electrokinetic flow in infinitely extended rectangular microchannels. *Journal of Colloid and Interface Science*, **261**, 21–31. 33

Yang, Z. & Maeda, R. (2002). A world-to-chip socket for microfluidic prototype development. *Electrophoresis*, **23**, 3474–3478. 13, 14